

**CHARACTERIZATION, STRUCTURAL ANALYSIS, AND IDENTIFICATION
OF INHIBITORS OF THE ATG8 AND THE ATG8-ATG3 INTERACTION IN
THE MALARIA PARASITE, *PLASMODIUM***

By
Adelaide Ulricke P. Hain

A dissertation submitted to Johns Hopkins University in conformity with the
requirements for the degree of Doctor of Philosophy

Baltimore, Maryland
January 2014

© 2014 Adelaide Hain
All Rights Reserved

Abstract

Autophagy is a catabolic process that normally utilizes the lysosome. With central roles in survival during stress and protein and organelle turnover, the far-reaching implications of this system in disease are being increasingly understood. Studying autophagy is complicated by its role in cell survival and programmed cell death and the involvement of the canonical marker of autophagy, Atg8/LC3, in numerous non-autophagic roles.

The malaria parasite, *Plasmodium*, has conserved certain aspects of the autophagic machinery but for what purpose has long remained a mystery. Major advances have recently been gained and suggest a role for Atg8 in apicoplast maintenance, degradation of heme inside the food vacuole, and possibly trafficking of proteins or organelles outside the parasite membrane.

Malaria kills nearly a million people each year, mostly children, representing a global public health problem. With ninety percent of these deaths in Africa, malaria also represents a major obstacle to the stability and economic prosperity of the nation. The essentiality of plasmodial Atg8, and its emerging role at the essential apicoplast organelle implicate Atg8 as a good drug target for antimalarial drug design. Atg8 is an ubiquitin-like protein, requiring an E1-activating and E2-conjugating enzyme for lipidation to membranes, required for its function. An important question is how the conjugation systems differ between *Plasmodium* and humans and how these differences can be exploited to design specific novel antimalarial drugs. We provide structural information

on the *P. falciparum* Atg8-Atg3 interaction, identify small molecule inhibitors against the interaction, and use these inhibitors to probe novel functions of Atg8 in *Plasmodium*.

Advisor:

Dr. Jürgen Bosch

Thesis Readers:

Dr. Michael J. Matunis

Dr. Isabelle Coppens

Dr. Sandra Gabelli

Alternate Readers:

Dr. Scott Bailey

Dr. Michael Trush

Acknowledgements

Science does not occur in isolation. With decreasing resources and increasing pressure to publish, it is necessary to collaborate in order to investigate a biological question with depth. The work presented in this dissertation would not be possible without the advice, reagents, equipment, and time of countless individuals. For reagents, supplies, and guidance, I would like to thank the following labs at Johns Hopkins University: Drs Sean Prigge, Krista Matthews, Michael Matunis, Scott Bailey, David Sullivan, David Graham and David Colquhoun, Caren Freel-Meyers, Arne Schön, Ernesto Freire, and Jelena Levitskaya. I would additionally like to thank Brian Learn for management and maintenance of equipment in the protein analysis room.

The following labs at other institutions have been invaluable: Drs Paul Roepe (Georgetown University), Joseph Smith and Marion Avril (Seattle Biomed), and Anthony Sinai (University of Kentucky). I would like to acknowledge the Johns Hopkins Malaria Research Institute for a predoctoral fellowship and its members for stimulating discussion the past five years, as well as the Hopkins Ubiquitin club for helping me hone my presentation skills.

I would like to thank members of my thesis advisory and final defense committee for thoughtful discussion and advice: Drs Michael Matunis, Isabelle Coppens, Sandra Gabelli, Scott Bailey, and Michael Trush.

I cannot thank my thesis advisor Dr. Jürgen Bosch enough for his guidance, mentorship, and patience throughout the years. He was a constant source of optimism and was always willing to discuss ideas or demonstrate a technique. He taught me the

importance of looking at a problem from different angles, and of not letting a technique define one's research, but to enhance it. Current and past lab members have made the past five years immeasurably easier and more enjoyable. Finally and not lastly, I thank my family, friends, and husband for their support.

Table of Contents

Abstract.....	ii
Acknowledgement.....	iv
Table of contents.....	vi
List of Tables.....	viii
List of Figures.....	ix
List of Abbreviations.....	xii
Chapter 1: Overview of autophagy pathways in <i>Plasmodium</i>	1
1. Why Malaria?	2
2. The <i>Plasmodium</i> Parasite.....	3
3. Introduction to Autophagy	4
4. Bioinformatics Search for Autophagy Proteins in <i>Plasmodium</i>	7
5. Recent Advances in the study of Atg8 in <i>Plasmodium</i>	9
6. Thesis Rationale.....	19
7. Methods & Materials	20
Chapter 2: Structural and biochemical studies of the PfAtg8-PfAtg3 interaction.....	25
1. Abstract.....	26
2. Introduction.....	27
3. Results.....	29
4. Discussion.....	35
5. Methods & Materials	37

Chapter 3: Identification of inhibitors against the plasmodial Atg8-Atg3 interaction.....	58
1. Abstract.....	59
2. Introduction.....	60
3. Results.....	65
4. Discussion.....	76
5. Methods & Materials.....	80
Chapter 4: Preliminary studies of the function of Atg8 in <i>Plasmodium</i>	104
1. Abstract.....	105
2. Introduction.....	106
3. Results.....	108
4. Discussion.....	113
5. Methods & Materials.....	120
Chapter 5: Final Conclusions and Closing Remarks	134
1. Finals Conclusions.....	135
2. Model for PfAtg8 Function.....	136
3. Remaining Questions	137
Appendix.....	141
References.....	156
Curriculum Vitae	173

List of Tables

Chapter 2

Table 2.1	X-ray diffraction and refinement statistics.....	44
-----------	--	----

Chapter 3

Table 3.1	Virtual library screening compounds.....	90
-----------	--	----

Table 3.2	MMV PTA comounds and derivatives.....	91
-----------	---------------------------------------	----

Chapter 4

Table 4.1	Candidate PfAtg8-interacting proteins from mass spectrometry-based interactome study.....	124
-----------	---	-----

Table 4.2	Putative AIMs in candidate PfAtg8 interacting proteins.....	126
-----------	---	-----

Appendix

Table A.1	Identity and additional information of Atg plasmodial homologues.....	142
-----------	---	-----

Table A.2	List of primers used in cloning and site-directed mutagenesis studies...	144
-----------	--	-----

Table A.3	List of constructs created for dissertation work.....	145
-----------	---	-----

Table A.4	Non-candidates from mass spectrometry-based PfAtg8 interactome study.....	147
-----------	---	-----

List of Figures

Chapter 1

Figure 1.1	The <i>Plasmodium</i> life cycle.....	21
Figure 1.2	Overview of autophagy, Atg8 conjugation.....	22
Figure 1.3	Conservation of autophagy proteins in <i>Plasmodium</i> genome.....	23
Figure 1.4	Expression data for autophagy protein homologues in <i>Plasmodium</i>	24

Chapter 2

Figure 2.1	Thermal stability of PfAtg8 Cysteine mutant.....	45
Figure 2.2	Protein interaction studies of recombinant PfAtg8 and PfAtg3.....	46
Figure 2.3	Comparison of PfAtg8 CM and WT affinity to PfAtg3.....	47
Figure 2.4	Identification of a putative AIM in PfAtg3.....	48
Figure 2.5	Identification of a PfAtg3 peptide that binds PfAtg8.....	49
Figure 2.6	The crystallographic structure of PfAtg8 ^{CM} -PfAtg3 ¹⁰³⁻¹¹⁰	50
Figure 2.7	Identification of an Apicomplexan-specific loop in PfAtg8.....	51
Figure 2.8	Analysis of the cargo receptor site of PfAtg8.....	52
Figure 2.9	Identification of Atg3-interacting residues in PfAtg8.....	53
Figure 2.10	Electrostatic surface potential of Atg8 homologues.....	54
Figure 2.11	Human LC3 does not bind PfAtg3.....	55
Figure 2.12	Multiple sequence alignment of Atg3 homologues.....	56
Figure 2.13	Conservation of PfAtg8 surface residues.....	57

Chapter 3

Figure 3.1	Identification of molecular fragments against the PfAtg8-PfAtg3 interaction.....	92
Figure 3.2	Primary screen of hydroxybenzene oxime library.....	93
Figure 3.3	Virtual library screen to identify A-loop pocket binders.....	94
Figure 3.4	Dose-dependent inhibition by VLS compound, C25.....	95
Figure 3.5	Identification of a common scaffold that inhibits Atg8-Atg3 from the MMV malaria box.....	96
Figure 3.6	<i>In vitro</i> and <i>silico</i> studies on PfAtg8-PTA compound binding.....	97
Figure 3.7	Synthesis of a PTA derivative with a functional handle.....	98
Figure 3.8	Inhibition of <i>P. falciparum</i> blood stages.....	99
Figure 3.9	Effect of PAH9 and C25 treatment on viability of HC-04 cells <i>in vitro</i>	100
Figure 3.10	Effect of PAH9 and C25 treatment on the development of <i>P. falciparum</i> 3D7 GFP parasite in HC-04 cells <i>in vitro</i>	101
Figure 3.11	PAH9 and C25 increase endogenous <i>P. falciparum</i> Atg8 protein levels.....	103

Chapter 4

Figure 4.1	PfAtg8 interacts with endogenous PfAtg3 in the blood stage.....	127
Figure 4.2	Sub-cellular location of PfAtg8-interacting candidate proteins.....	128
Figure 4.3	Biological function of PfAtg8-interacting candidate proteins.....	129

Figure 4.4	PfAtg8 co-localizes with apicoplast protein, ACP in blood stages.....	130
Figure 4.5	PfAtg8 co-localizes with exported virulence factor PfEMP1 in blood stages.....	131
Figure 4.6	Partial co-localization of PfAtg8 with maurer's cleft protein, SBP-1 within blood stage parasites.....	132
Figure 4.7	PfAtg8-PfAtg3 inhibitors decrease PfEMP1 staining on RBC surface...	133
Chapter 5		
Figure 5.1	Model for PfAtg8 function in the erythrocyte stage.....	140
Appendix		
Figure A.1	Overview of drug design approach.....	148
Figure A.2	Binding of fragment 410 to the MBP-PfAtg3 CM3 chip	149
Figure A.3	Deconvolution of 2,3-dihydroxybenzaldehyde hit from first pass screen	150
Figure A.4	Alignment of <i>P. yoelii</i> and <i>P. falciparum</i> Atg8.....	151
Figure A.5	¹ H- ¹⁵ N HSQC 2D spectrum of ¹⁵ N-His ₆ -PfAtg8 ^{CM}	152
Figure A.6	PfAtg8 co-localization under <i>in vitro</i> high parasitemia conditions	153
Figure A.7	PfAtg8 localization under PAH9 drug treatment.....	154
Figure A.8	Sequence alignment of various PfEMP1 ATS domains.....	155

List of Abbreviations

3-MA	3-methyladenine
ACP	Acyl-carrier protein
AIM	Atg8 interacting motif
Atg	Autophagy gene
ATS	Acidic intracellular segment
BSA	Bovine serum albumin
CSA	Chondroitin sulfate A
CM	Cysteine mutant
CQ	Chloroquine
Cvt	Cytoplasm-to-vacuole targeting
EM	Electron microscopy
FBDD	Fragment-based drug design
FCC	Fragment cocktail crystallography
FV	Food vacuole
His ₆	Hexahistidine
IFA	Immunofluorescence assay
IPTG	Isopropyl-b-D-thiogalactopyranoside
iRBC	Infected red blood cell
ITC	Isothermal titration calorimetry
KO	Knockout
LIR	LC3-interacting region

MBP	Maltose binding protein
MC	Maurer's cleft
ns	Not significant
PAGE	Polyacrylamide gel electrophoresis
PAS	Pre-autophagosomal structure
PBS	Phosphate buffered saline
PE	Phosphatidylethanolamine
Pf	<i>Plasmodium falciparum</i>
PfEMP1	<i>Plasmodium falciparum</i> exported membrane protein 1
PI3K	Phosphatidyl-Inositol 3-phosphate Kinase
PS	phosphatidylserine
PV	Parasitophorous vacuole
RBC	Red blood cell
SAR	Structure activity relationships
SBDD	Structure-based drug design
SDS	Sodium dodecyl sulfate
SPR	Surface plasmon resonance
SUMO	Small Ubiquitin-like modifier
TM	transmembrane domain
Ub	Ubiquitin
VLS	Virtual library screening
WT	Wild type
WU-BLAST	Washington University – Basic Alignment Search Tool

Chapter 1

Overview of autophagy pathways in *Plasmodium*

Sections previously published as:

Hain *et al.* Autophagy in *Plasmodium*, a multifunctional pathway?

Comp & Struct Biotech J. 2013

Vol 8, Issue 11, <http://dx.doi.org/10.5936/csbj.201308002>

Why Malaria?

There are many public health problems facing the world: cancer, AIDS, neurodegenerative disease, and increasingly diabetes. In contrast, malaria is a disease most Americans likely only become aware of when preparing to travel abroad. So why should one care about a disease that already has existing treatments and whose impact is constrained to the developing world?

One could counter with the global impact of the disease; half the world's population is at risk of malaria and in 2010 there were 219 million clinical cases and 660,000 deaths from malaria (1). Because of the confounding nature of the disease and the lack of access to health care in many regions, especially in Africa, the number of cases is most likely underestimated. What is lost in the numbers is the human face; 86% of victims are under 5 years of age (1). Pregnant women are especially susceptible to malaria, which accounts for 8-14% of low weight births in malaria-endemic regions, a poor indicator for the future health of that child (2). Additionally, the economic toll of the disease is astounding. Poverty is a positive indicator for malaria prevalence and mortality; countries with lower gross national incomes have higher malaria mortality rates and within countries, children from poorer families are more likely to die from the disease (3). Malaria prevents children from attending school and adults from working continuing the cycle of malaria and poverty.

Artemisinin combination therapy is the first-line defense for *P. falciparum*-causing malaria in most countries. As was the case for previous antimalarials, such as chloroquine, resistance is emerging against artemisinin and has been detected in 4

countries in Southeast Asia (1). We are in a never-ending arms race with the malaria parasite and it is pivotal to have new and effective therapies ready when resistance inevitably spreads to other parts of the world. Finally, many antimalarials have severe side effects including insomnia, intense itchiness, psychosis, sunburn, and blindness (4-8). Treatment for the hypnozoite-causing species, *P. vivax*, requires Primaquine, which causes hemolysis in patients with glucose-6-phosphate dehydrogenase deficiency (9).

There is great hope, along with great skepticism, for a malaria vaccine. The most furthest candidate, RTS,S, is in Phase 3 clinical trials (10). This vaccine targets *P. falciparum*, leaving large swaths of the world unprotected, where *P. vivax* is the predominant malaria-causing species. Additionally the vaccine offers partial protection that is far from optimal. Although promising vaccine targets are in the pipeline (11), there is a need for development of new antimalarial drugs for the foreseeable future.

The *Plasmodium* Parasite

The *Plasmodium* parasite is a unicellular eukaryote that has evolved distinctive biological mechanisms to invade and replicate within different cell types in both the mosquito vector and mammalian host as part of its life cycle (Figure 1.1). During a mosquito blood meal, elongated sporozoites are injected into the host and invade liver cells. Here, the parasite undergoes major morphological changes, transforming from an elongated structure into a round trophozoite (12, 13). Rhoptries and dense granules, as well as other organelles believed to be unnecessary after initial host invasion, are degraded shortly after parasite metamorphosis within the liver (13). The parasite uses a

form of asexual replication, schizogony, to produce hundreds to thousands of teardrop-shaped merozoites. Extensive remodeling of the host cell creates a merozoite, which contains the merozoites that are released into the bloodstream to continue the next stage of infection, the symptomatic erythrocytic stage (14, 15).

Merozoites invade the red blood cells (RBC) and develop into the ring stage form. This continues to the active feeding, or trophozoite stage before undergoing schizogony to produce more merozoites for sequential rounds of invasion and replication. During the trophic stage, hemoglobin is taken up from the host RBC cytoplasm and transported to the food vacuole (FV), a lysosome-like compartment where it is degraded to provide amino acids for parasite growth. Some merozoites are shunted from this cycle to produce gametocytes, which are subsequently taken up by a mosquito during a blood meal, continuing the *Plasmodium* life cycle.

All members of the phylum Apicomplexa, with the exception of *Cryptosporidium*, contain apicoplasts, plastid organelles analogous to chloroplasts in plants, acquired through endosymbiosis. The organelle is essential to *Plasmodium* survival in both asexual stages and is the site for synthesis of iron-sulfur clusters, isoprenoids, and fatty acids (16). It contains four membranes, requiring unique transport processes for trafficking proteins to the apicoplast lumen.

Introduction to Autophagy

Classically, autophagy has been defined as a eukaryotic system for degradation of cellular material inside the lysosome. The best-studied form, macroautophagy,

encapsulates the cytoplasmic material inside a double-membrane vesicle, the autophagosome that fuses with the lysosome (Figure 1.2A). Once considered a nonselective bulk process, autophagy is now appreciated as a way to quickly respond to shifting cellular conditions and to selectively degrade damaged organelles, proteins, nucleic acids, and pathogens

The first mention of plasmodial autophagy in the literature was in the 1970s by D.C. Warhurst and colleagues. They conducted extensive studies showing increased pigment clumping in “autophagic vacuoles (AV)” following chloroquine (CQ) treatment in blood stage parasites (17, 18). In the 2000s, drug treatment was again reported to induce autophagic vacuoles and an autophagic cell death (19, 20). However, leading researchers in autophagy have warned against the visualization of autophagosomes through electron microscopy as the sole evidence for an autophagic process (21, 22). The difficulty in culturing certain stages of the parasite, genetically manipulating the organism to make conditional knockouts, and to clone and express genes recombinantly all have contributed to a void of knowledge in this area. The last year witnessed an expanse in papers exploring autophagic pathways in the *Plasmodium* parasite.

Overview of autophagy

Although over 30 AuTophagy (Atg) proteins have been identified in yeast, not all are essential to macroautophagy. Autophagy induction in yeast (and mammals) begins with the Atg1 (ULK1 in mammals) protein kinase complex, which is inhibited by the target of rapamycin, TORC1 (mTOR in mammals) complex under homeostasis. Nutrient deprivation or rapamycin treatment alleviates the negative regulation on the Atg1

complex (23). Atg1 and Atg13 form a complex with Atg31/Atg17/Atg29/Atg11 in yeast, analogous to the ULK1/Atg13/FIP200/Atg101 complex in mammals, at the pre-autophagosomal structure (PAS) (24, 25). Atg17 has been implicated as the most upstream scaffold for protein recruitment to the PAS (26). Phosphorylation of substrates by Atg1 activates the Phosphatidyl-Inositol 3-phosphate Kinase (PI3K) class III complex, composed of Vps34, Atg14, Vps15/p150, and Atg6 (Beclin1 in mammals) which converts phosphatidylinositol (PI) into phosphatidylinositol triphosphate (PI(3)P) at the site of the PAS (27). This creates a binding site for Atg18 (WIPIs in mammals) and Atg2 at the isolation membrane, also requiring association with the transmembrane protein Atg9 (28).

Elongation of the membrane and closure of the autophagosome requires the ubiquitin (Ub)-like protein, Atg8 (LC3 in mammals), which is covalently attached via its C-terminal glycine to phosphatidylethanolamine (PE) in the phagophore membrane (29). Atg8 utilizes a similar conjugation pathway as Ub for lipidation, diagrammed in Figure 1.2B. In most species, Atg8 is proteolytically activated by Atg4, then transferred to an E1-activating enzyme, Atg7, before transfer to its E2-conjugating enzyme, Atg3 for lipidation (30, 31). Another autophagy Ubl protein, Atg12, is covalently attached to Atg5, requiring Atg7 as well, and its own E2, Atg10 (32). The Atg12-Atg5 conjugate forms a complex with Atg16 to drastically increase conjugation of Atg8 through rearrangement of Atg3's catalytic site (33, 34). The autophagosome seals and fuses with endocytic compartments and the lysosome where the material is broken down and recycled back to the cytoplasm.

Bioinformatics Search for Autophagy Proteins in *Plasmodium*

To obtain an overview of the system, we performed bioinformatics analysis to identify putative orthologues of autophagy proteins in *Plasmodium falciparum*. While such lists have been published, our analysis focused on the minimal machinery needed for macroautophagy in yeast (35-39). The coordination of events in macroautophagy is diagrammed in Figure 1.3, with putative homologues identified in *Plasmodium* colored in black and less reliable identifications in gray. Although several hits were identified for the nutrient sensor TOR, these hits have clearer homology to Phosphatidyl-Inositol 4-Kinases. Of the proteins involved in autophagy induction, Atg1 and its mammalian binding partners, FIP200 and Atg101 appear to have orthologues in *Plasmodium*, while Atg13 appears absent. The C-terminal Atg13-binding domain is also missing from PfAtg1. It contains several potential Atg8-interacting motifs, which mediate Atg1 binding to Atg8 in an Atg13-independent manner in yeast and humans (40). PfPI3K exists in *P. falciparum* and is one of the better-characterized proteins. Vps15 and Atg14, members of the PI3K complex were identified. While Atg6 was not identified using our methods, it has recently been reported by Cervantes et al (41).

Atg9 is an essential transmembrane protein for autophagy thought to supply Golgi-derived membranes to the PAS during initiation (42, 43). None of the significant BLAST hits for Atg9 are predicted to contain any of its six transmembrane domains. Atg18 likely has a homologue in *Plasmodium* and contains the FRRG motif necessary for binding to PI(3)P and Atg18-Atg2 recruitment to the PAS as well as WD40 repeats for beta propeller formation. Atg18 is thought to aid recruitment of Atg8 to the PAS and

protect it from premature Atg4 cleavage (44). A putative homologue for Atg18's binding partner, Atg2, was also identified but is annotated as a putative rhopty protein.

Atg8, Atg7, and Atg3 orthologues are present (Figure 1.2C). Atg8 contains a C-terminal glycine in *Plasmodium* (45). Similar Atg8 homologs have been identified in plants and other protists including *Toxoplasma* (46, 47). Therefore, the putative Atg4 orthologue is likely important for recycling improperly conjugated Atg8 (48). Putative homologues for the Ubl, Atg12 and its target, Atg5, were identified. However, the C-terminal glycine of PfAtg12 and its E2 enzyme needed for covalent attachment are absent. It is unclear if Atg16, which forms a 350 kDa complex with Atg12-Atg5 is present. It is essential *in vivo* but not *in vitro* for Atg8 lipidation (33, 49).

Fusion of both autophagosomes and endosomes with the lysosome requires Rab7 and various SNAREs (50, 51). Apicomplexans contain a basic set of Rabs, including Rab7 (52). Putative homologues for essential SNAREs including Vti1b and VAMP8 also exist in *Plasmodium*. The lipase for breaking down the autophagosome membrane, Atg15 (53) was absent in our search but is reported by another group (41). The vacuolar proteinase Prb1 (53, 54) was also not found, however the parasite contains numerous proteases in the food vacuole for degrading hemoglobin. The lysosomal amino acid efflux pump Atg22 is present (55). More information, including the PlasmoDB code of hits and e-values are presented in the appendix (Table A.1).

Expression data for autophagy genes

PlasmoDB houses RNA-Seq data during the blood stage for each gene (56). Additionally, several widespread mass spectrometry studies have provided data on

protein expression in the liver and blood stages (57-62). There is also specific transcript, immunoblotting and/or immunofluorescence data for a small subset of autophagy genes (38, 39, 63-65). Evidence for expression from these various sources is compiled in Figure 1.4 and supports an important role for autophagy proteins during the late blood stage, where both hemoglobin digestion and apicoplast growth is maximal. Less data is available for non-blood stages. Atg8, Atg3, and Atg7 are transcribed during all life cycles of *P. berghei* (64).

Recent Advances in the Study of Atg8 in *Plasmodium*

Localization of the autophagy marker, Atg8 in Plasmodium

Atg8/LC3 is the classical marker for autophagy as it is covalently attached to the pre-autophagosome (PAS) membrane at an early stage and stays conjugated to the autophagosome during fusion with the lysosome. In yeast and mammals, Atg8/LC3 has a diffuse cytoplasmic distribution under nutrient rich conditions but forms punctate upon autophagy induction (30). The lipidated fraction of Atg8 can also be visualized as a faster migrating band with high percentage or urea-containing gels in SDS-PAGE (31).

Several groups have examined the localization of Atg8 in different *Plasmodium* species and stages. Under normal conditions, *P. berghei* liver and *P. falciparum* blood stage Atg8 are in punctae that are nearby and partially colocalize with the apicoplast markers, such as acyl-carrier protein (ACP) (38, 39, 64, 66). Localization to other organelles, such as mitochondria, rhoptries, micronemes, and dense granules was negative in the schizont, while transgenic Atg8 lacking the C-terminal glycine for

lipidation showed diffuse localization, validating the results of these studies (38). In hepatocytes, PbAtg8 localization along the apicoplast was observed 14 hours post-invasion and increased with organelle size throughout the liver stage (64).

Roepe and Sinai also observe punctate PfAtg8 in blood stage trophozoites, but co-localization with ACP, or other organelle markers, was not assessed (67). Interestingly, when cells were transferred to media lacking amino acids and glucose for 6 hours, PfAtg8 redistributes to a wider punctate staining that seems to be inside the host red blood cell cytoplasm. Similar re-localization was seen in treatment with high levels of CQ (67). Langsley and colleagues also starved blood stage parasites in media lacking amino acids. At 4 hours, they observed localization of PfAtg8 to double-membrane structures also containing PfRab7, required for autophagosome-lysosome fusion in other species, that were near or inside the food vacuole, visualized with electron micrographs (66). This has thus far, provided the strongest evidence for autophagic process where the food vacuole is the final digestive compartment in a *Plasmodium*.

Less attention has been paid to the mosquito stages, however PfAtg8 shows elongated tubular localization in mosquito midgut oocytes and sporozoites from the mosquito salivary glands. This staining is reminiscent of apicoplast morphology under normal cell conditions (64).

Atg8 is essential for Plasmodium

Knockout of Atg8 is lethal in the mouse malaria model, *P. yoelli* (68). In the highly related Apicomplexa, *Toxoplasma*, the E2 conjugating enzyme for Atg8, TgAtg3, is also indispensable (47). It was recently shown that attenuation of PfAtg7, the E2

enzyme necessary for Atg8 lipidation, led to a severe growth defect of *P. falciparum* blood stages (65). Consistent with this, a fraction of *Plasmodium* Atg8 is lipidated in blood stages and is necessary for localization to the apicoplast (38, 66, 69).

Potential Functions for Atg8 in Plasmodium

Atg8's essentiality in *Plasmodium* is intriguing, as Atg8 knockouts are viable in yeast under homeostatic conditions (29), which suggests an alternative or additional vital function(s) in the parasite. Proposed roles include vesicular trafficking, growth and maintenance of the apicoplast, and programmed cell death.

Hemoglobin degradation and autophagy

In early to mid-trophozoite stages, host cytoplasm is endocytosed, delivering hemoglobin to the food vacuole, for subsequent generation of amino acids. It has long been reported that CQ treatment led to production of vesicles inside the *Plasmodium* parasite (18, 19), which were assumed to be autophagic vesicles. Chloroquine (CQ) is a lysosomotropic agent that prevents autophagosome-lysosome fusion (70, 71). In other studied Eukarya, CQ causes an accumulation of Atg8 lipidated to autophagosomes in starvation and non-starvation conditions (70). A longstanding antimalarial, CQ accumulates in the food vacuole and prevents hemozoin dimerization and hemoglobin digestion (72), starving the parasite of amino acids.

Varying responses are observed in *Plasmodium* upon CQ treatment and this appears to be due in part to the concentration that is used and the duration of treatment. In CQ-sensitive strains, such as 3D7, ten to 100 nM is cytostatic whereas micromolar amounts are cytotoxic (73). Extended incubation (12 hours) with 120 nM CQ leads to a

build-up of hemoglobin-containing vesicles, (74) likely by preventing fusion of these vesicles with the food vacuole, preventing hemoglobin digestion and starving the parasite of amino acids. Sinai and Roepe report drastic re-localization of PfAtg8 from the parasite to the RBC host cytoplasm with either prolonged starvation or high cytotoxic concentrations of CQ (67). The authors hypothesize that PfAtg8 may be involved in vesicular trafficking of hemoglobin or other nutrients under starvation conditions.

In contrast, Kitamura *et al.* do not see a change in PfAtg8 localization or protein levels in response to 300 nM CQ treatment. However these concentrations are cytostatic, and may not be sufficient to induce a lysosomotropic effect; 100 μ M is typically used in mammalian cell lines to block autophagy (73). Additionally the treatment period was shorter than in other studies.

Recently, immuno-EM and IFA studies show re-localization of PfAtg8 to Rab7-containing vesicles near and inside the food vacuole when parasites are deprived of amino acids for 4 hours, providing the strongest evidence for an autophagic process (66). While these authors never saw PfAtg8 in the host cytoplasm, Cervantes *et al.* report some Atg8 staining in the RBC even under normal conditions (41).

Vps34, also known as class III PI3K, is a lipid kinase at the ER that produces PI(3)P on the outer leaflet, important for recruitment of proteins to the phagophore and proper curvature of the autophagosome (26, 75). PfVps34 purified from parasite lysate has kinase activity that can be inhibited by the well-characterized class III PI3K complex inhibitor, wortmannin. Endogenous PfVps34 localizes to the food vacuole and vesicular structures near the host plasma membrane in the blood stage (63). Strikingly, the PI3K inhibitor, wortmannin (10 μ M, 5 hour treatment), caused accumulation of hemoglobin-

containing endocytic vesicles within the parasite and subsequently less in the FV, indicating a defect in digestion concomitant with decreased parasite growth. They suggest the class III PI3K complex is important for hemoglobin endocytosis and trafficking to the FV in *Plasmodium* (63). While the effect of wortmannin on *Plasmodium* Atg8 was examined under normal conditions, it was not tested under starvation conditions to see if treatment prevented PfAtg8 localization to vesicles and the FV. However another PI3K inhibitor, 3-MA, inhibited re-localization of PfAtg8 to the host cytoplasm upon starvation or CQ treatment, implicating involvement of Atg8 in trafficking of these hemoglobin-containing vesicles (69).

The malaria parasite does not obtain isoleucine from hemoglobin and is dependent on the host for this amino acid. *Plasmodium* can survive up to 72 hours without exogenous isoleucine, suggesting a survival mechanism is present. Since food vacuole proteases are essential to survival, an autophagic mechanism was suggested (76).

While two independent studies concluded that *P. berghei* Atg8 could not complement an Atg8 knockout in yeast, a recent study showed *P. falciparum* Atg8 to be a functional homologue for ScAtg8 (38, 64, 66). This discrepancy between the species is unexpected as *P. berghei* and *P. falciparum* Atg8 are 88% identical to each other and 40% identical to yeast Atg8. Transgenic PfAtg8 was not lipidated in mammalian cells, indicating PfAtg8 cannot complement the human homologue and PfAtg3 could not interact with human LC3 (45, 64).

Vesicular Trafficking

Protein Secretion: The *Plasmodium* parasite initiates extensive remodeling of the host cell upon infection by exporting hundreds of its own proteins into the host cell.

Plasmodium is encapsulated by a parasitophorous vacuole (PV) within host cells. Proteins targeted for export to the host cytosol or plasma membrane must be trafficked out of the parasite plasma membrane and the PV, necessitating novel pathways for protein secretion. How this is done is still under extensive study, but one possibility is unconventional protein secretion, termed exophagy (77).

A recent review suggests that vesicles originating at the ER via the formation of PI(3)P are destined for export to the host cytoplasm (78). PfPI3K partially co-localizes with exported membrane protein 1 (PfEMP1), a virulence factor in *P. falciparum* that is exported to the erythrocyte surface (63). One of the more characterized routes of protein export beyond the PV utilizes a PEXEL motif for recognition. Recently, PI(3)P was shown to bind the PEXEL motif at PI(3)P-enriched regions in the ER (79). PfAtg8 localization in the RBC cytoplasm is reported, but only under starvation conditions (67) and co-localization with PfEMP1 or the Maurer's cleft (MC), an intermediate compartment for protein export in the RBC cytoplasm, was not examined.

Protein trafficking to the food vacuole: PI(3)P, is enriched at both the apicoplast and the food vacuole and one of the few PI(3)P-binding proteins identified in *Plasmodium*, FCP protein, is trafficked to the FV using an unknown mechanism, which some suggest may be similar to the autophagic cytoplasm-to-vacuole targeting pathway in yeast (80). Support is garnered by the presence of Atg8 vesicles in and near the food vacuole (66).

Organelle expulsion: The malaria parasite undergoes major morphological changes in the early liver stage, converting from a motile, slender sporozoite into a round trophozoite. During this transformation, organelles used for liver cell invasion, including

the inner membrane complex, rhoptries, and micronemes, are expelled from the parasites (12). Treatment of *Plasmodium* sporozoites with 3-methyladenine (3-MA), which targets Vps34, needed for PI(3)P production and phagophore formation, delays conversion into trophozoites (81). Electron micrographs of liver stage parasites revealed double-membraned structures morphologically similar to autophagosomes containing micronemes leading to the hypothesis that exophagy of organelles could be important for differentiation in the liver stage in the absence of an extensive intracellular degradative system (36).

Programmed cell death

Programmed cell death (PCD) is increasingly being examined in protozoans as a way to modulate host-pathogen responses and limit parasite load (82). Autophagy is a recognized mechanism of cell death in other eukarya where the balance between pro-survival and pro-death is tightly regulated (83). Autophagic cell death has previously been reported for the protozoan parasites *Toxoplasma* and trypanosomes and less conclusively in *Leishmania*, but there is controversy as to the legitimacy of a regulated rather than incidental mechanism of cell death in protozoa (84-88).

Treatment of *P. falciparum* erythrocytes with chloroquine (180 nM), SNAP, a nitric oxide donor, and staurosporine, an apoptosis inducing agent, led to cell death that was described as autophagic-like because of distinct vacuolarization of the parasite cytoplasm and presence of double-membrane structures, whereas the nuclear morphology remained in tact and other apoptotic markers were absent (19). The morphology of this cell death is similar to that observed in retinal pigment epithelial cells upon treatment

with much higher concentrations (120 μ M) of CQ and is thought to be the mechanism for retinotoxicity associated with CQ. In this case, they also did not see hallmarks of apoptosis but did see increased lipidation of LC3 to autophagic vacuoles and a block in degradation of the autophagy-specific substrate, p62 (89). Autophagic vacuoles were also observed in *P. berghei* blood stage parasites dying after treatment with dihydroartemisinin (20). In this study, the authors concluded, “Since the food vacuole membranes were affected, the nutrition of parasites was blocked and the autophagic vacuoles formed quickly as a result of amino-acid hunger of parasites.” However distribution of Atg8 was not investigated.

After invasion of hepatocytes, a significant fraction of *P. berghei* parasites die through an autophagic mechanism (38). This was observed in cell culture and in mice, indicating it is a physiological mechanism. The process is restricted to the later stages of development. Eickel et al. described double membrane structures that appeared similar to those reported by Meis and Verhave in 1985, then portrayed as “membranous whorls” (13). Yet, fluorescence microscopy revealed that PbAtg8 never localized to these vesicular structures and remained associated with the apicoplast, determined by colocalization with ACP, and its organellar fragments throughout the cell death event (38). Treatment with rapamycin (500 nM), which potently induces autophagy in yeast through inhibition of TOR, decreased parasite size and changed apicoplast morphology, but did not affect PbAtg8 localization. However, there is no known TOR orthologue in *Plasmodium*, and the observed effect on parasite growth could be mediated through off-target effects or effects on host autophagy (90). The authors speculate that autophagy occurs in the parasite but is independent of Atg8. Although Atg8 is the canonical

autophagic marker, there are reports of macroautophagy that is independent of LC3 conjugation (91). This alternative pathway requires ULK1, Rab9, and Beclin 1; of which there may be orthologues in *Plasmodium* (41).

Apicoplast maintenance

The apicoplast is vital to survival in both mammalian stages. A gradual increase in apicoplast size begins in the trophozoite stage. Dramatic elongation and branching of the organelle occurs in the late trophozoite/early schizont stage. Division of the apicoplast occurs late in the schizont and ultimately results in each merozoite containing one apicoplast (92). If the autophagic machinery delivers lipids or proteins to the growing apicoplast membrane, the expression of its component proteins is necessary by the trophozoite stage. As shown in Figure 2, this appears to be the case.

Pf/PbAtg8 localizes to the apicoplast in liver and blood stages under normal conditions. Electron micrographs and biochemical data indicate that Atg8 is conjugated to the outermost membrane of the apicoplast (39). *Plasmodium* treated with chloramphenicol leads to loss of the apicoplast, which is normally lethal, but supplementation with isopentenylpyrophosphate (IPP) allows the parasite to survive during the RBC stage (93). Tomlins et al. observed PfAtg8 localization under these conditions. Strikingly, PfAtg8 was located at vesicular structures that also contained the apicoplast-targeted protein LipDH1, suggesting a role in trafficking (66).

Treatment of parasites with the Vps34 inhibitor, wortmannin (10 μ M), did not change the localization of PfAtg8 at the apicoplast in the blood or liver stage suggesting Atg8 localization to the apicoplast is constitutive and not induced by the class III PI3K

complex (39, 66). However PfVps34 is also located at the apicoplast and its product, PI(3)P, is enriched at the apicoplast and nearby single-membrane vesicles, in addition to the food vacuole (94). PI(3)P production is maximal in later blood stages and Tawk et al. suggest that PI(3)P vesicles transport lipids or proteins to the apicoplast, as is the case in *T. gondii* (95). In agreement with this vital role, PI3K is essential in *P. berghei* (94). As of now, there are no studies describing co-localization between PI3K and Atg8.

Interestingly, although PbAtg8 localized to the apicoplast in the liver stage, its E1 activating and E2 conjugating enzyme, Atg7 and Atg3, were located at the mitochondria, leading the authors to question whether they interact with PbAtg8 (38). However, localization was only described at 52 h.p.i., at which point PbAtg8 is already lipidated to the outer membrane of the apicoplast (64). It is difficult to imagine how Atg8 is lipidated without an activating and conjugating enzyme, other than the possibility that an E1 and E2 enzyme function has divergently evolved. Further localization studies in other stages and time points, as well as knockout of Atg3 and Atg7 would address these questions.

Thesis Rationale

Teasing apart how autophagy can promote cell survival and cell death has been a central question for all eukaryotes and is especially important in cancer research. Autophagy may well be the mechanism by which the malaria parasite dies with CQ and

artemisinin treatment, necessitating a better understanding of PCD pathways in *Plasmodium* as well.

It appears that Atg8, due to its unique ability to be covalently attached to membranes and to bind diverse proteins through adaptors has been conserved throughout Eukarya, even when other autophagy proteins are not. The list of non-autophagic functions for Atg8 homologues continues to grow and includes functions independent of membrane conjugation (96, 97). Since *P. yoelli* Atg8 knockouts are nonviable and conditional knockouts are difficult in *Plasmodium*, a selective inhibitor preventing lipidation of Atg8 would be an invaluable tool that could also serve as a potential antimalarial therapeutic. Plasmodial Atg8's essentiality and our recently elucidated crystal structure, presented in Chapter 2, make PfAtg8 a prime target for structure-based drug design (45). Our efforts to this end are presented in Chapter 3. Finally, we present intriguing data on the function of Atg8 in *Plasmodium* in Chapter 4.

Methods & Materials

Bioinformatics search: The genome sequence of *P. falciparum* was published in 2002 and is stored along with various data associated with each gene in the *Plasmodium* Genome database (PlasmoDB) (98, 99). The amino acid coding sequence of *Saccharomyces cerevisiae* and *Homo sapien* ATG genes were queried for putative homologues using the WU-BLAST program within PlasmoDB. Hits were identified based on the Expect (e)-value of the BLAST search, as well as annotation in PlasmoDB, any functional knowledge, conservation among all the plasmodial species sequenced, and the length of the hit in comparison to the query. Of note, the most likely homologue did not necessarily have the highest e-value in the initial PlasmoDB BLAST search. Additionally the species used as the query had a major impact on the returned BLAST hits. Often the same hit was identified with both the human and yeast homologue query but sometimes a strong hit was only identified with one species. In a few cases other species were used as a query (Table A.2). An inverse BLAST was performed with the potential hits using NCBI Position-Specific Iterated (PSI) BLAST against the *S. cerevisiae* or *H. sapiens* non-redundant protein sequence database, and if that failed, with the Domain Enhanced Lookup Time Accelerated (DELTA) BLAST. Hits were additionally screened in Pfam to see if they contained the domains or motifs important to that homologue's function, such as coiled-coil domains and lipid binding motifs. For transmembrane proteins, the TMHMM server 2.0 (<http://www.cbs.dtu.dk/services/TMHMM/>) was used to compare predicted membrane topology.

Figures

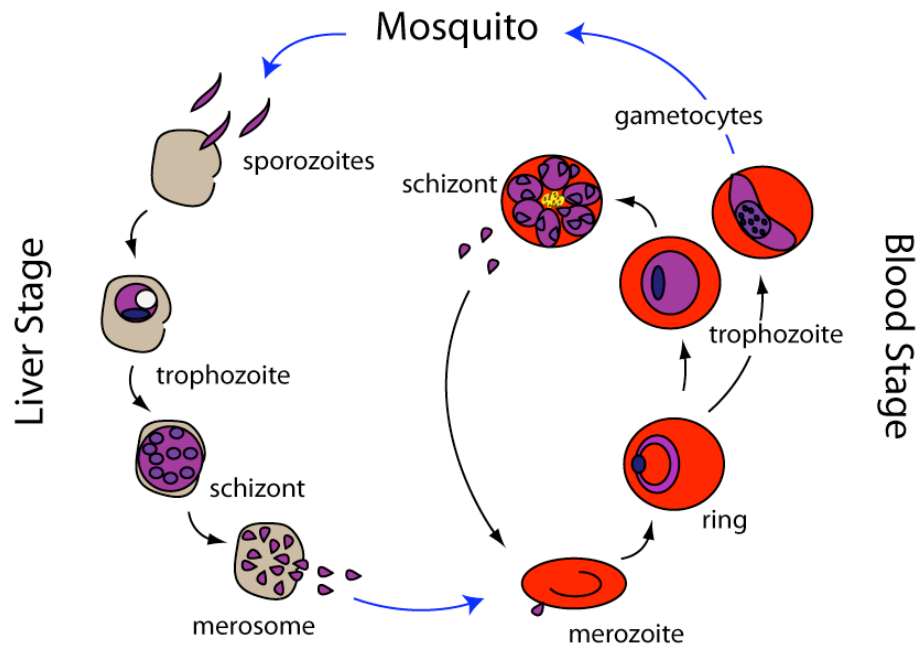


Figure 1.1. *Plasmodium* mammalian life cycle. Blue arrows indicate transition to a new cell type or host.

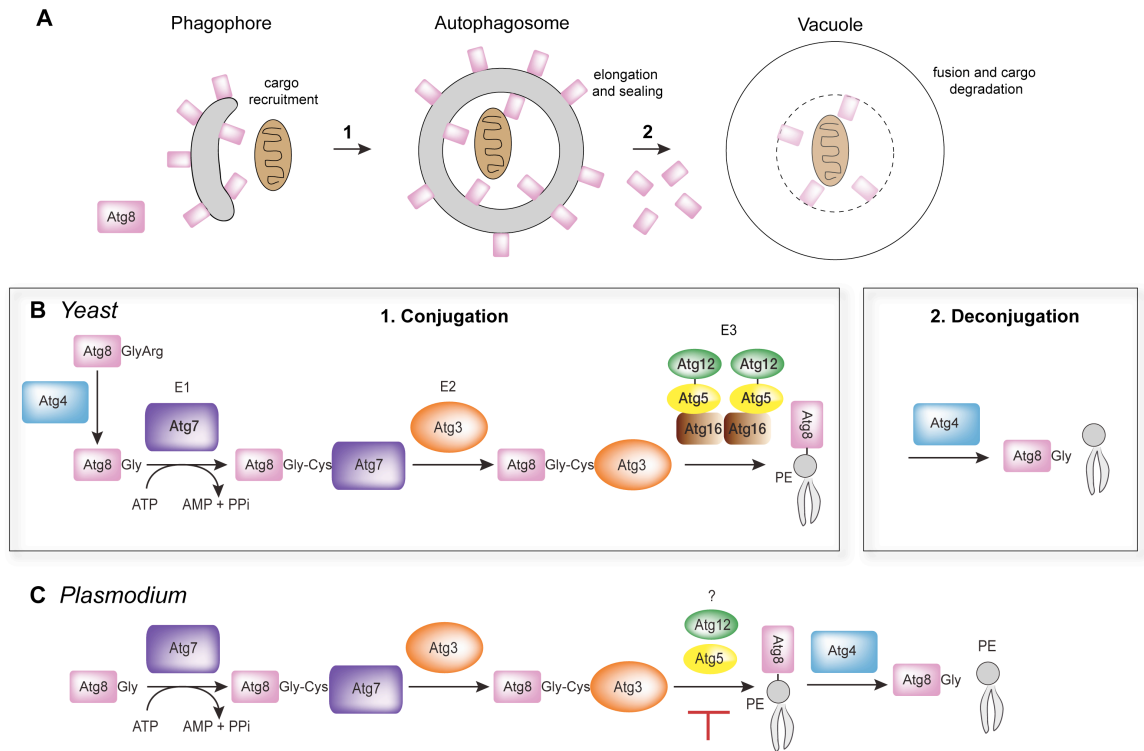


Figure 1.2. Atg8 conjugation pathway. **A.** Overview of macroautophagy and localization of Atg8 to growing autophagosome. **B.** Yeast Atg8 conjugation pathway. 1. Atg8 is attached to phosphatidylethanolamine in the phagophore through a ubiquitin-like conjugation cascade. Atg8 leads to autophagosome elongation and maturation. The autophagosome fuses with the vacuole to degrade its contents. 2. Atg4 reverses the covalent attachment, recycling Atg8 from the outer membrane before degradation in the vacuole. **C.** Putative Atg8 conjugation pathway in *Plasmodium*. Red line indicates the step of the conjugation pathway we attempted to target for inhibition in *Plasmodium*.

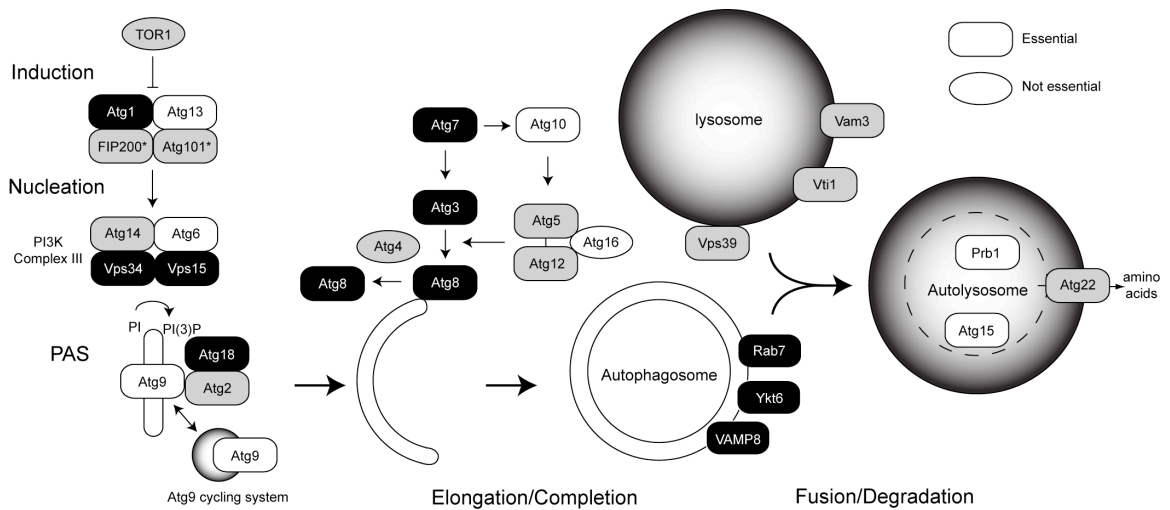


Figure 1.3. Conservation of autophagy proteins in *Plasmodium*. Proteins essential for macroautophagy are depicted as rectangles. Ovals represent proteins whose essentiality is not known. Black indicates strong evidence for homology (e-value less than $1e-10$ in initial BLAST within PlasmoDB and reciprocal identification using PSI-BLAST with e-value less than $1e-20$). Gray indicates homology less clear (initial e-value cutoff of 0.012 and identification of initial query in either PSI- or DELTA-BLAST with e-value that may not be significant). White indicates no orthologue identified. *Human proteins FIP200 and Atg101 thought to be functional homologues of yeast Atg31/Atg17/Atg29.

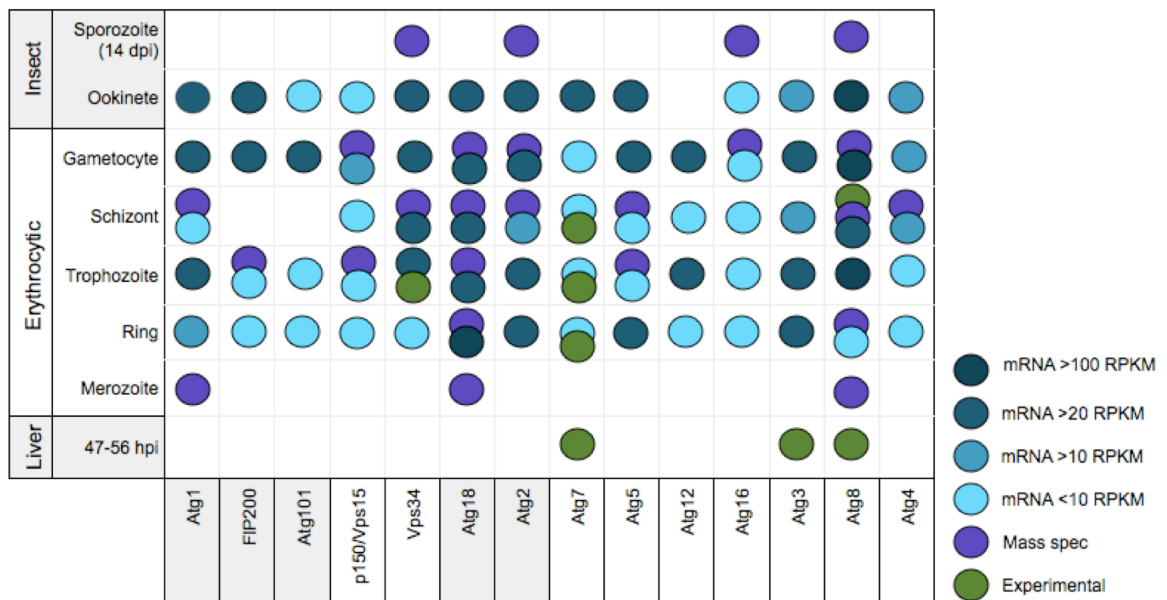


Figure 1.4. Expression data of autophagy proteins during *Plasmodium* life cycle. RNA-Seq and mass spectrometry data from PlasmoDB and data from published studies is compiled. All data is for *P. falciparum* homologues (Table A.1), except liver stage data derived from *P. berghei*.

Chapter 2

Structural and biochemical studies of the *Plasmodium* Atg8-Atg3 interaction

Previously published as:

Hain *et al.* Structural characterization and inhibition
of the *Plasmodium* Atg8-Atg3 interaction
J Struct Biol 2012

Vol 180, Issue 3, pg 551-562, <http://dx.doi.org/10.1016/j.jsb.2012.09.001>

Abstract

The autophagy-related proteins are thought to serve multiple functions in *Plasmodium* and are considered essential to parasite survival and development. We have studied two key interacting proteins, Atg8 and Atg3, of the autophagy pathway in *P. falciparum*. These proteins are vital for the formation and elongation of the autophagosome and essential to the process of macroautophagy. Autophagy may be required for conversion of the sporozoite into erythrocytic-infective merozoites and may be crucial for other functions during asexual blood stages. Here we describe the identification of an Atg8 family interacting motif (AIM) in *Plasmodium* Atg3, which binds PfAtg8. We determined the co-crystal structure of PfAtg8 with a short Atg3¹⁰³⁻¹¹⁰ peptide, corresponding to this motif, to 2.2 Å resolution. Our *in vitro* interaction studies are in agreement with our X-ray crystal structure. Furthermore they suggest an important role for a unique Apicomplexan loop absent from human Atg8 homologues. Together our structural and interaction studies represent a starting point for future antimalarial drug discovery and design for this novel protein-protein interaction (PPI).

Introduction

Atg8 is a conserved Ub protein, necessary for macroautophagy as well as many types of selective autophagy. In all structures determined, Atg8 homologues contain a Ub fold at its core with N-terminal helix extensions. Atg8 is also similar to Ub in its utilization of a conjugation pathway for covalent attachment to its substrate. Whereas Ub, SUMO, and other Ub-like proteins are covalently attached to other proteins, Atg8 is unique in its attachment to a lipid head group, phosphatidylethanolamine (PE) and possibly also phosphatidylserine (PS) (100).

Most Atg8 orthologues require proteolytic processing of one or several amino acids to expose a C-terminal glycine. The exposed C-terminus of Atg8 is attached to its E1 activating enzyme, Atg7, through a thioester bond that requires activation by ATP hydrolysis. Atg8 is then transferred to its E2 conjugating enzyme, Atg3, to form another thioester bond before being transferred to PE in the phagophore membrane (Figure 1.2B). In addition to thioester formation with Atg3, Atg8 interacts noncovalently with Atg3 prior to substrate attachment (101). *In vitro*, Atg8 lipidation is accelerated through the E3-like action of the Atg12-Atg5 conjugate (33). It is not known if a functional E3 exists in *Plasmodium* as putative orthologues have only been identified for a portion of the machinery (102). Additionally, *Plasmodium* Atg8 is synthesized with a C-terminal glycine, indicating that Atg4 would not be necessary for activation (68). However, a likely Atg4 homologue is present in *Plasmodium* and is thought to regulate Atg8 localization by releasing Atg8 from membranes as is seen in other species (Figure 1.2C).

Lipidation of Atg8 to the autophagosome instills Atg8 with unique features within the autophagy pathway. Atg8 serves as the canonical autophagy marker as it forms a stable interaction with the autophagosome early and remains associated through lysosome-autophagosome fusion and subsequent degradation (70) (Figure 1.2A). Autophagy also serves to recruit substrates into the autophagosome for selective autophagy through interaction with intermediary autophagic cargo receptors (reviewed in (103)). These receptors, like Atg3, interact with Atg8 through their Atg8-interacting motif (101).

Here we report x-ray crystal structure of PfAtg8 with a peptide corresponding to PfAtg3. We provide biochemical and structural evidence that *P. falciparum* (Pf) Atg8 binds PfAtg3 in a conserved mechanism as reported in other species, including humans. Despite this conservation we have discerned regions in the parasite protein that can be exploited by small molecules to specifically target the *Plasmodium* Atg8-Atg3 interaction.

Results

Verification of PfAtg8 and PfAtg3 interaction

Recombinant *Plasmodium* Atg8 (PF3D7_1019900) expressed in *E. coli* showed very low solubility in all species tested (PbAtg8, PvAtg8, and PfAtg8). While mutation of Lys26 to Pro in yeast Atg8 decreased aggregation and retained full autophagic activity (104, 105), Proline is already present at this position in *Plasmodium*. Through site-directed mutagenesis and thermal shift assays (TSAs), a triple cysteine mutant (C37I, C119S, C122S) was identified that had significantly increased solubility and is referred to here as the cysteine mutant (CM) (Figure 2.1). Because Cys37 was predicted with homology modeling to be buried within the Ub-like core, we mutated this residue to the hydrophobic amino acid, Ile. Exposed free Cysteine residues are often a source of aggregation and in otherwise refractory proteins, mutagenesis has been successful in yielding crystals (106). Similar procedures to decrease aggregation, such as cysteine carboxymethylation, were not found to alter the overall protein structure when compared to the native protein structure (107).

We also cloned and expressed the putative E2 conjugating enzyme, PfAtg3, in *E. coli*. Notably, amplification of blood stage strain 3D7 cDNA yielded a product matching the PF3D7_0905700.2 variant of Atg3 from the PlasmoDB database. Binding of PfAtg8 to PfAtg3 was tested through various methods, including native electromobility gel shift assays and dynamic light scattering (DLS) (Figure 2.2). Isothermal titration calorimetry (ITC) provided a dissociation constant (K_D) of 406 nM for the interaction and a one-to-one binding stoichiometry, in agreement with the DLS results (Figure 2.2). Surface

plasmon resonance (SPR) kinetic experiments showed a similar affinity for PfAtg3 to either wild type (WT) or CM PfAtg8 (Figure 2.3), validating our use of PfAtg8^{CM} in biochemical and structural studies. We next sought to elucidate the interaction interface on each protein.

Molecular Basis of Plasmodium Atg8-Atg3 Interaction

An Atg8 family interacting motif (AIM) has been identified in Atg8's conjugating enzyme, Atg3 as well as in Atg8-binding proteins involved in the cytoplasm-to-vacuole targeting (Cvt) pathway in yeast and selective autophagy in mammals. The motif is Θ XX Γ , where Θ is aromatic and Γ is hydrophobic, with nearby acidic residues preferred (108-110). We identified two potential AIMs in PfAtg3, shown in Figure 2.4, and mutated the Trp105 and Trp214 in each to Alanine. PfAtg3 was recombinantly expressed with a maltose binding protein (MBP) tag and binding to PfAtg8 was tested through MBP pulldown assays. PfAtg8 binding was unaffected in the PfAtg3^{W214A} mutant and decreased by 35% in PfAtg3^{W105A} as compared to wild type (Figure 2.4A). TSAs confirmed the decreased binding in the W105A mutant is not due to destabilization of the tertiary structure and implicates this region as a potential AIM (Figure 2.4B).

We next tested whether a synthetic peptide, corresponding to residues 103-110 of the potential AIM were sufficient for binding PfAtg8. The PfAtg3¹⁰³⁻¹¹⁰ peptide led to a concentration-dependent positive shift in the T_m of PfAtg8 in TSAs, indicating binding and stabilization of PfAtg8, while a control peptide of PfAldolase³⁶⁴⁻³⁶⁹ did not affect the T_m (Figure 2.5). To exclude nonspecific stabilization by the peptide, we evaluated whether the PfAtg3¹⁰³⁻¹¹⁰ peptide could compete with full length PfAtg3 for PfAtg8

binding in SPR studies. PfAtg8 was injected over a chip containing immobilized MBP-PfAtg3 with increasing concentrations of PfAtg3¹⁰³⁻¹¹⁰ or PfAldolase³⁶⁴⁻³⁶⁹ peptides and the SPR response was measured. The PfAtg3¹⁰³⁻¹¹⁰ peptide inhibited interaction with full length PfAtg3 in a concentration-dependent manner, whereas the control peptide did not have an effect (Figure 2.5), supporting the identification of a conserved AIM in PfAtg3, WLLP, responsible for PfAtg8 binding.

Crystallization of PfAtg8^{CM}-PfAtg3¹⁰³⁻¹¹⁰ complex

Protein crystals of PfAtg8^{CM} were obtained in the presence of the PfAtg3¹⁰³⁻¹¹⁰ peptide, presented in Figure 2.6A,B. The structure of the complex was solved by molecular replacement with an ensemble of 20 models using Phaser as described in the materials and methods section (111). The structure was refined to an R_{work}/R_{free} combination of 20.5/27.9% with a twin fraction of 9.4% and zero Ramachandran outliers (Table 2.1). The asymmetric unit contained three copies of Atg8 and three copies of the bound peptide corresponding to a 1:1 ratio of protein to peptide. The buried surface area between any two given chains of PfAtg8 is approximately 1,330 Å², not indicative of a stable multimer in solution. The three copies of PfAtg8 superimpose with an r.m.s.d. of 0.02 Å for 120 C_α-atoms. The PfAtg3¹⁰³⁻¹¹⁰ peptide also superimposes well except for the N- and C-terminal residues, which adopt different orientations in the crystal lattice. PfAtg8 contains an N-terminal domain composed of two alpha helices attached and stabilized via hydrogen bonding to a C-terminal ubiquitin (Ub)-like domain as has been visualized in other Atg8 homologues (108, 112-114). Our structure additionally contains two short beta strands, connected by a beta turn between α3 and β5 which is absent from

all other homologue structures (Fig. 2.7A). Sequence alignment shows that *Plasmodium* Atg8 contains an insertion of nine residues only conserved within Apicomplexa (Figure 2.7B), which we term the A-loop. These residues comprise $\beta 3$ and the turn in the loop. $\beta 3$ forms numerous hydrogen bonds with the antiparallel $\beta 4$ strand. The secondary structure observed for $\beta 3$ and $\beta 4$ may be due to crystal contacts as the loop forms numerous hydrogen bonds with the PfAtg3¹⁰³⁻¹¹⁰ peptide of another chain and may explain why we were unable to obtain crystals without the peptide (Figure 2.7C). We term the pocket formed between A-loop and the Ub core the A-loop pocket.

The cargo-receptor site

In yeast and mammals two hydrophobic pockets, termed the cargo receptor site, bind AIMs in diverse proteins. The “W-site” binds Trp and the “L-site” binds Leu in the AIM (101, 108, 115) (109, 116). Our crystal structure confirmed that two hydrophobic pockets in PfAtg8 are responsible for binding the PfAtg3¹⁰³⁻¹¹⁰ peptide (Figure 2.8A). This is similar to the determined structures of Atg8-Atg19^{peptide} and microtubule-associated protein 1 light chain 3 (LC3)-p62^{peptide} structures (108, 115). The side chain of PfAtg3 Trp105 binds deeply inside the W-site of PfAtg8, which consists of residues L4, E16, T17, I20, P29, V30, V31, K47, F48, L49, and Y112. Pro108 of the PfAtg3 peptide fits in the L-site, consisting of residues R27, F48, L49, V50, P51, M54, E58, F59, I62 and M99 (Figure 2.8B). The peptide additionally makes hydrogen bonds with the side chains of K45, E58, and H66 surrounding the W- and L-site.

Identification of Atg3-interacting residues

We next sought to identify the residues of PfAtg8 involved in binding PfAtg3. To verify that the W- and L-site pockets binds PfAtg3 in solution, the following mutants were made in and near the potential cargo receptor site: K47E, L49A, R27E, K47E/K19E, E44A/K45S/K46A, shown in Figure 2.9A. Our structure elucidated a loop of nine amino acids (68 to 76) located below the W/L-sites. Sequence alignment shows that these residues are conserved only within Apicomplexa (Figure 2.7B). As loops are often important for imparting specificity, we deleted residues 68-76. PfAtg8 variants were tested for binding using an MBP pulldown assay with immobilized MBP-PfAtg3 as before (Figure 2.9C). R27E, K47E, and L49A W-site mutations all reduced binding to MBP-PfAtg3. Binding was not reduced to the same degree in the L49A mutant as in the yeast system. The triple mutant PfAtg8^{E44A/K45S/K46A}, containing mutations near the W-site showed moderate decreases in binding. Strikingly, PfAtg8^{68-76Δ} binding was reduced by 80%, as quantified with ImageJ (117), suggesting a large interaction surface between PfAtg8 and PfAtg3. Thermal shift assays verified that, with the exception of R27E, the mutations were not structurally destabilizing (Figure 2.9D) (118). Our studies confirm that the cargo receptor site is conserved in PfAtg8 and is involved in binding PfAtg3.

Comparison of PfAtg8 to human Atg8 homologues

The overall conservation of the binding site makes it a challenging task to design specific inhibitors targeting *Plasmodium*, however differences exist in amino acid composition (Figure 2.8), electrostatic surface potential and cargo receptor pocket size. For example, the W-site of *Plasmodium* is $\sim 100 \text{ \AA}^3$ larger than the corresponding site in the human orthologues, microtubule-associated protein 1 light chain 3 (LC3), and Golgi-

associated ATPase enhancer of 16 kDa (GATE-16). Figure 2.10 compares the electrostatic surface on the Atg3-binding face of PfAtg8 with GATE-16 and LC3. All three proteins have a prominent positively charged band on the cargo receptor site face. Relative to PfAtg8, the orientation of this band is tilted 40° and 55° in GATE-16 and LC3, respectively. Both PfAtg8 and GATE-16 show striking differences compared to LC3, where the positive charge is concentrated around the central area of the protein and $\alpha 1$ and $\alpha 2$ form an acidic patch above the W-site that is basic in the other proteins. The L-site of GATE-16 is predominately positively charged whereas PfAtg8 is more neutral in this region. An acidic patch formed between $\alpha 3$ and the loop between $\beta 1$ and $\beta 2$ in both GATE-16 and LC3 is basic and neutral in our structure and forms a deeper groove due to the $\beta 3$ strand inserted in the PfAtg8 structure.

These differences led us to hypothesize that the human Atg8 homologues would not bind *Plasmodium* Atg3. We compared binding of recombinant human LC3 and PfAtg8 to immobilized PfAtg3 with SPR-based assays. Whereas PfAtg8 bound PfAtg3 with a dissociation constant of 296 nM, LC3 did not bind PfAtg3 (Figure 2.11), indicating the *Plasmodium* and human conjugation systems are not interchangeable.

Discussion

Our biochemical and structural studies indicate that PfAtg8 binds an AIM in PfAtg3. To date, the crystal structure of Atg3 has only been elucidated for yeast and *Arabidopsis thaliana* (PDB codes 4GSL, 3VX8, 2DYT, 3T7G). Biochemical analysis of yeast Atg3 indicates it interacts with the W- and L-site of Atg8 through an AIM located in the handle region of Atg3 (109). The handle region is severely truncated in *Plasmodium* Atg3, similarly as in the human homologue (Figure 2.12). Additionally, the PfAtg3 AIM differs from known motifs in yeast and humans by the presence of proline, rather than leucine or isoleucine at the fourth position of the motif (Θ XXT). Prolines are often found at the edges of beta-strands suggesting the possibility this region forms a beta strand in solution. Recent NMR and X-ray studies on yeast Atg7 and Atg8 suggest that substrates can bind the Atg8 cargo receptor site without forming an intermolecular beta sheet (119). Crystallization of full length *Plasmodium* Atg3 will help elucidate the secondary structure of the AIM while solution NMR experiments may reveal the different states of this region in the presence or absence of a substrate.

PfAtg8 shows the greatest sequence and structural similarity, with minimal r.m.s.d., to GATE-16, implicated in intra-Golgi trafficking and macroautophagy in mammals. Like GATE-16, it does not contain the extra beta strand located between β 3 and α 4 in LC3 and TbAtg8. Considering the 74% sequence similarity between the cargo receptor site of the human homologue LC3 and *Plasmodium* Atg8, it is surprising that LC3 cannot interact with PfAtg3. However, differences in the extent and orientation of charges, as well as the larger size of the pocket in PfAtg8 may explain the lack of binding

in the heterologous system. These charge and size differences can be exploited to selectively target the parasite autophagy system. Additionally, our structure contains a semi-ordered insertion of two beta strands between $\alpha 3$ and $\beta 5$ with respect to structures in other species. Our mutagenesis studies suggest an important role for the Apicomplexan-specific loop (A-loop) in mediating interactions between PfAtg8 and PfAtg3. Together our structural and biochemical studies implicate a unique pocket formed between the loop and the Ub-like core, which could potentially be targeted with a small molecule inhibitor. Further studies are required to determine how this region interacts with PfAtg3 and if it is amenable to drug design. While the cargo receptor site is well conserved across Atg8 homologues, there is more divergence on the other side of the protein, as well as regions just outside the receptor site including $\alpha 1$, which may be able to serve as anchoring points during drug design (Figure 2.13).

Future Directions:

Because the A-loop is specific to Apicomplexa, understanding how these residues bind PfAtg3 would help guide drug design. While *Toxoplasma gondii* (Tg)Atg8 expresses and purifies well, TgAtg3 showed low expression. We have created new constructs to test for improved expression. In the future we will attempt to co-crystallize the Atg8-Atg3 complexes from Toxoplasma and other Apicomplexa. Construct engineering was successful in producing a more stable Atg8 protein for crystallization. We could undertake similar strategies such as surface entropy reduction, cysteine mutation or methylation, or truncations with PfAtg3.

Methods & Materials

Cloning, expression, and purification: Unless otherwise stated, purification steps were conducted on ice or at 4°C. The purity of protein purification samples was assessed with SDS-PAGE, visualized with either Gelcode blue (Thermo Scientific) or coomassie stain.

Cloning, expression, and purification of PfAtg3: *PfAtg3* was cloned from *P. falciparum* 3D7 cDNA using primers containing either a His₆ tag and NcoI and BamHI restriction sites (A3HF and A3R (Table A.2 and A.3)), ligated into a pET45b vector or just NcoI and BamHI sites (A3MF and A3R (Table A.2 and A.3) ligated into a modified pET45b vector to have an N-terminal MBP tag followed by a TEV protease cleavage site (MBP-PfAtg3). Constructs were verified with DNA sequencing and transformed into *E. coli* BL21-R11 cells. A single colony was used to inoculate TB-media and grown at 37°C. Protein expression was induced at an OD₆₀₀=0.35 with 1 mM IPTG and expressed at 20°C for 16 hrs. Cells were harvested and the bacterial pellet resuspended in lysis buffer containing 50 mM Tris pH 7.0, 500 mM NaCl, with a Complete EDTA-free protease inhibitor cocktail tablet (Roche) and benzonase (Sigma). Cells were lysed with an EmulsiFlex C5 cell disruptor at 15,000 PSI and cleared with 35,000 x g for 35 min. MBP-PfAtg3 was applied to amylose resin and washed with lysis buffer. Bound protein was eluted in 50 mM Tris pH 7.0, 2 mM DTT, 20 mM maltose. His₆-PfAtg3 was purified with TALON™ resin (Clontech). Following a washing step with lysis buffer, PfAtg3 was eluted in 50 mM Tris pH 7.0, 300 mM imidazole. Constructs were further purified using anion exchange chromatography over a RESOURCE™ Q column (GE Healthcare)

with a gradient of 0 to 1 M NaCl in 50 mM Tris pH 7.0, 2 mM DTT using an ÄKTA purifier system.

Cloning, Expression, and Purification of PfAtg8: *PfAtg8* amplified from 3D7 cDNA and ligated into a PQE-30 vector (Qiagen) was kindly provided by Dr. I. Coppens, Johns Hopkins University, USA. *PfAtg8* was sub-cloned using primers A8MF and A8R (Table A.2 and A.3), containing NcoI and BamHI restriction sites, and ligated into a modified pRSF-1b vector with an N-terminal Maltose binding protein (MBP) tag and Tobacco etch virus (TEV) protease cleavage site. An N-terminal His₆-tagged construct was made using primers A8HF and A8R, containing NcoI and BamHI sites and hexahistidine tag, and ligated into a pRSF-1b vector (Novagen). Plasmids were transformed into *E. coli* BL21-RII cells containing a rare codon plasmid. A single colony was used to inoculate TB media containing 50 µg/mL kanamycin and 34 µg/mL chloramphenicol and grown at 37°C. At an O.D. 600 of 3.3, protein expression was induced with 0.3 mM IPTG and grown for 16 h at 20°C under vigorous shaking.

Cells were harvested by centrifugation at 4,000 x g, 30 min, resuspended in 50 mM HEPES pH 8.0, 500 mM NaCl, 1 mM MgCl₂, 10% glycerol, a tablet of Complete EDTA-free protease inhibitor cocktail tablet (Roche) and 500 U benzonase, and lysed using an EmulsiFlex C5 cell disruptor at 15,000 PSI. After centrifugation at 35,000 x g for 30 min, MBP-PfAtg8 lysate was incubated with amylose resin (NEB) and washed with lysis buffer before eluting with 50 mM HEPES pH 8.0, 20 mM maltose, 10% glycerol. Protein was dialyzed with homemade MBP-TEV protease at molar ratio of 1:100 in 50 mM MES pH 6.5, 10% glycerol, 0.5 mM EDTA, 1 mM DTT. Cleaved

protein was separated from TEV and MBP through cation exchange over a RESOURCE™ S column (GE Healthcare) using an ÄKTA purifier system. Pure fractions were dialyzed in 50 mM MES pH 6.5, 50 mM NaCl, 10% glycerol overnight and concentrated using a filter device with 3 kDa MWCO (Amicon).

After centrifugation, His₆-PfAtg8 lysate was incubated with Cobalt-charged TALON resin (Clontech), washed with lysis buffer, and eluted in 50 mM HEPES pH 8.0, 300 mM imidazole, 10% glycerol. Elutions were further purified with a RESOURCE™ S column as for MBP-PfAtg8.

Expression and Purification of hLC3: *MAP1LC3B* (hLC3) was amplified from a mammalian expression vector (generous gift of Dr. M. Hardwick, Johns Hopkins University) and ligated into a modified pET45b vector to contain an MBP N-terminal tag and TEV protease cleavage site using primers L3MF and L3MR containing NcoI and BamHI restriction sites (Table A.2 and A.3). MBP-LC3 was expressed and purified following the same protocol as MBP-PfAtg8.

Site-directed mutagenesis: Amino acid changes were introduced into constructs using the protocol and reagents in the QuickChange® Lightning site-directed mutagenesis kit (Agilent) (Table A.2 for primers, A.3 for constructs). A previously published, modified protocol was followed to delete residues 68-76 from PfAtg8 (120).

Native Electromobility Shift Assay (EMSA): His₆-PfAtg8 and His₆-PfAtg3 in 50 mM HEPES pH 8, 300 mM Imidazole, 10% glycerol, 1 mM MgCl₂, 10 mM DTT were mixed

in equimolar amounts and run in native loading buffer on a Tris-HCl 7.5% gel (Biorad) at 4°C, 80V for 4.5 hrs and visualized with Gelcode blue protein stain (Thermo Scientific).

Proteins were also run alone at the same concentration for comparison.

Isothermal titration calorimetry: Binding affinities and thermodynamic binding parameters for His₆-PfAtg8 and His₆-PfAtg3 were determined using a MicroCal VP-ITC instrument (GE Healthcare). His₆-PfAtg3 at 97.8 μM was titrated into cell containing 17 μM of His₆-PfAtg8 in 50 mM HEPES pH 7.0, 50 mM NaCl, 10% glycerol, 1 mM TCEP at 25°C. An initial injection of 3 μL was followed by 28 10 μL injections, 20 sec. each with 400 sec. spacing, a filter period of 2 and stirring speed of 500 rpm. Data analysis was performed with Origin 7 software using the heats of dilution of the titrant to normalize the raw heats of injection and a single site-binding model.

SPR: Runs conducted on a Biacore 3000 instrument (GE Healthcare). Unless otherwise stated, runs were conducted in running buffer (RB1) containing 354 μM KH₂PO₄, 1.87 mM Na₂HPO₄, 51.5 mM NaCl, pH 7.4, 0.01% v/v P20, 0.2 mg/ml BSA at 25°C (Quality Biologicals). Bound analyte was dissociated from the chip using 1 injection of 1 M MgCl₂ followed by 2 blank injections of RB between each concentration. Binding and equilibrium constants were determined with Scrubber (BioLogic™). A double referencing method was applied to correct for nonspecific binding to the chip with interspersed blank injections correcting for baseline drifts.

PfAtg3 immobilization: The surface chip was pre-conditioned with multiple injections of 20 mM glycine pH 2.2 prior to pH scouting for identification of optimal

conditions for Atg3 binding to the sensor chip. MBP-PfAtg3, dissolved in 10 mM Na Acetate pH 4.0, was immobilized by amine coupling to the surface of a CM3 sensor chip (GE Healthcare).

Determination of dissociation constants for PfAtg8 WT and CM: His₆-PfAtg8^{CM} and His₆-PfAtg8^{WT} were injected over MBP-PfAtg3-immobilized CM3 chip at 20 μL/min with 6 2-fold dilutions at the lowest concentration, increasing to 250 nM. Injection volumes were 40 μL and 60 μL and dissociation times were 120 sec and 150 sec, for CM and WT, respectively.

Inhibition of PfAtg8-PfAtg3 interaction by PfAtg3¹⁰³⁻¹¹⁰ peptides: A dilution series was set up with His₆-PfAtg8^{CM} at a constant concentration of 200 nM and 9 3-fold dilutions of peptide starting at 400 μM in RB. His₆-PfAtg8^{CM} without peptide injections were interspersed to check for chip decay or decreases in protein activity. Each concentration was run in triplicate at 20 μL/min, with 60 μL injections and a 150 sec dissociation time.

Binding analysis of PfAtg8^{CM} and hLC3: Binding was measured using purified His₆-PfAtg8^{CM} and hLC3 with 7 2-fold dilutions in 1.06 mM KH₂PO₄, 5.6 mM Na₂HPO₄, 154 mM NaCl, pH 7.4, 0.01% v/v P20, 0.2 mg/mL BSA (RB2) starting at 625 nM injected at 40 μL/min at 37°C.

Crystallization of PfAtg8^{CM}-PfAtg3¹⁰³⁻¹¹⁰: MBP-PfAtg8^{CM} was expressed and purified as specified. Pure fractions from the RESOURCE™ S column were further purified on a HiLoad S75 column (GE Healthcare) in 50 mM MES pH 6.5, 7% glycerol, 1 mM MgCl₂, 2 mM DTT. Equimolar PfAtg3¹⁰³⁻¹¹⁰ peptide was added to PfAtg8^{CM} at 2 mg/ml and

concentrated in a 3 kDa MWCO filter device (Amicon) to 8 mg/mL. More peptide was added to a final concentration of 2.5 mM. Original crystals were identified from a screen set up with 200 nL of protein and 200 nl reservoir using a Mosquito crystallization robot (TTP Labtech) containing 100 mM MES pH 6, 0.2 M Ca(OAc)₂, 20% w/v PEG 8000 equilibrated at 20°C in a 96-well sitting drop INTELLI-PLATE® (Art Robbins Instruments). Conditions were further optimized to obtain larger crystals using a 24-4 sitting drop INTELLI-PLATE® (Art Robbins) with reservoir containing 100 mM MES pH 6.5, 100 mM Ca(OAc)₂, 20% w/v PEG 8000 and sitting drops containing 2 µL protein at 8 mg/mL and 2 µL reservoir, equilibrated at 20°C. Crystals were mounted in a 0.3 mm nylon cryoloop (Hampton Research) and flash frozen directly in liquid nitrogen before shipping to the Stanford Synchrotron Radiation Lightsource. Data sets were collected at SSRL beamline 12-2 at λ 1.033 Å using a microfocus beam of 6 x 9 µm and the Berkeley Advanced Light Source beamline 5-01 at λ 0.977 Å with a 100x100 µm beam.

Data Collection and Structure Determination: The crystals belonged to the space group P2₁ with cell dimensions of a=33.30 Å, b=111.08 Å, c=57.09 Å and β =92.58°. Data reduction and scaling was carried out with XDS/XSCALE (121). The refined twin fraction was 9.6% as determined by Refmac (122). The asymmetric unit contained three monomers resulting in a solvent content of 48%. We initially failed to obtain a molecular replacement solution with various models using Phaser (111), MOLREP (123), and BALBES (124). Only the combination of 20 models including homology models generated by Robetta (125) yielded a molecular replacement solution using phenix.ensampler (126) together with phenix.automr (111). Manual rebuilding and

refinement was carried out in Coot (127). TLS refinement was performed with TLS groups determined by the TLSMD server (128) using Phenix (129, 130). PfAtg8 was refined to a crystallographic R_{work} of 20.5% and an R_{free} of 27.9% (131). The final structure was analyzed with validation tools in Coot (127) as well as MOLPROBITY (132), indicating zero Ramachandran outliers (133).

Tables

Table 2.1. Data collection, phasing and refinement statistics

	Native	
Data collection	SSRL12-2	ALS5-01
Space group	P2 ₁	P2 ₁
Cell dimensions		
<i>a, b, c</i> (Å)	33.30, 111.08, 57.09	33.26, 110.33, 56.57
α, β, γ (°)	90, 92.58, 90	90, 92.49, 90
Wavelength	1.0332	0.9774
Resolution (Å)	31 - 2.2 (2.24-2.18)	20 - 2.25 (2.3-2.25)
<i>R</i> _{merge}	21.5 (91.8)	10.1 (44.7)
<i>I</i> / σI	7.3 (1.6)	9.05 (2.2)
Completeness (%)	87.6 (45.0)	88.2 (46.2)
Redundancy	2.1 (2.2)	1.13 (1.54)
Wilson B (Å ²)	29.08	23.94
Beam size (μm)	6 x 9	100 x 100
Refinement		
Resolution (Å)	31 - 2.2	20 - 2.2
No. reflections	21538	15705
<i>R</i> _{work} / <i>R</i> _{free}	20.5/27.9	23.8/28.7
<i>Refined twin fraction</i> (%)	9.6	40.5
No. atoms		
Protein	3289	3289
Ligand/ion	23	23
Water	331	331
<i>B</i> -factors (Å ²)		
Protein	31.6	19.2
Ligand/ion	51.4	57.6
Water	46.2	54.77
R.m.s deviations		
Bond lengths (Å)	0.008	0.012
Bond angles (°)	1.197	1.306
<i>Ramachandran main chain dihedral analysis</i> **		
favored	96.9% (370/382)	97.1% (371/382)
allowed	3.1% (12/382)	2.9% (11/382)
outliers	0	0
<i>Molprobit side chain rotamer analysis</i> **		
bad rotamers	1.3% (5/372)	0.81 (3/372)

*Highest resolution shell is shown in parentheses.

** According to Molprobit (132).

Figures

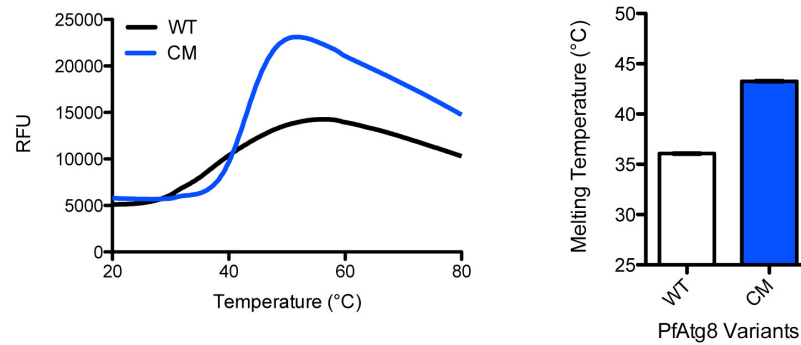


Figure 2.1. Thermal stability of PfAtg8 Cysteine mutant. Wild type (WT) and cysteine mutant (CM) His₆-PfAtg8 were expressed and purified concurrently and tested for thermal stability. **A.** Melting curve of PfAtg8 for CM (blue) and WT (black). **B.** The melting temperature of WT and CM was determined from the first derivative melting curve and plotted for three internal measurements. Error bars represent standard deviation (SD).

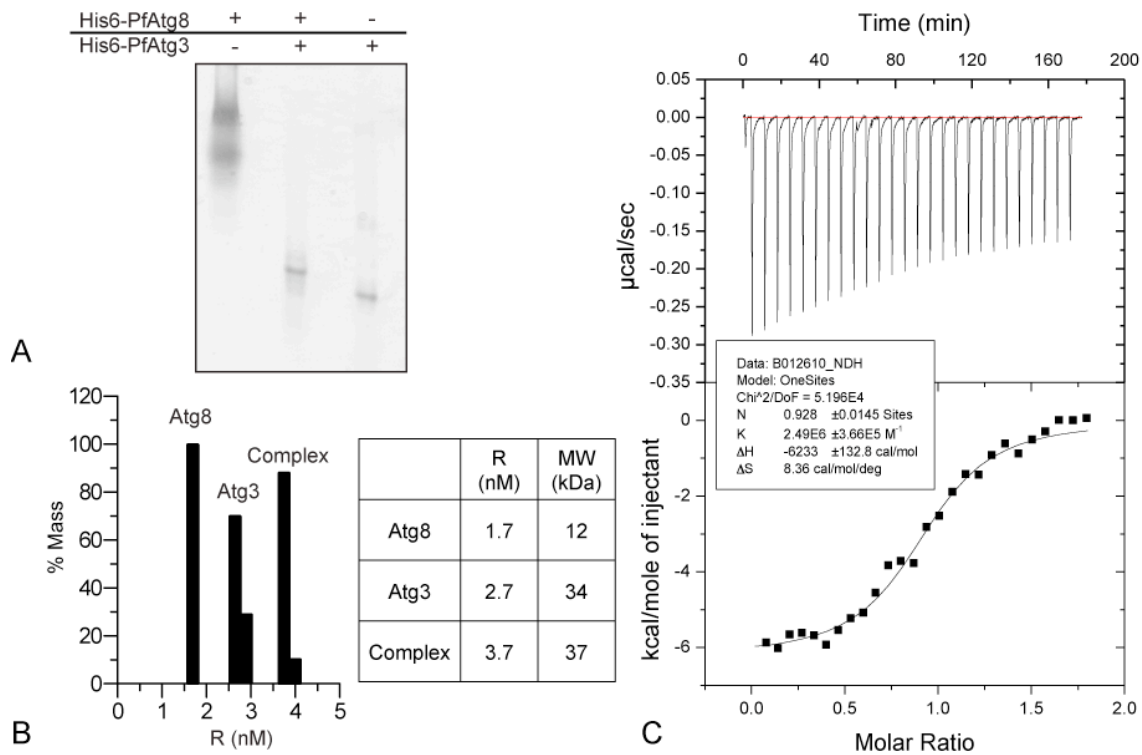
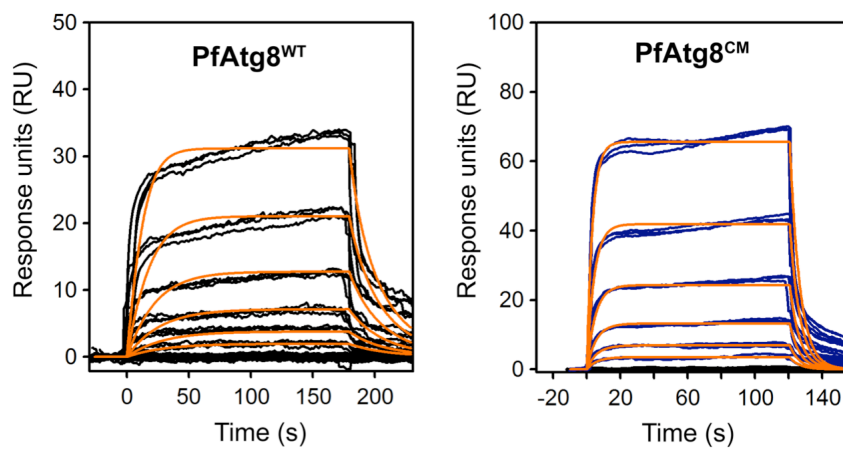


Figure 2.2. Protein interaction studies of recombinant PfAtg8 and PfAtg3. **A.** Native electromobility shift assay. His₆-PfAtg8 and His₆-PfAtg3 were run alone and together on a native PAGE and stained with Gelcode blue. **B.** Dynamic light scattering analysis of His₆-PfAtg8, His₆-PfAtg3, and the complex with the radius and predicted MW for a globular protein. **C.** Isothermal titration calorimetry analysis of His₆-PfAtg3 injected into cell containing His₆-PfAtg8. The stoichiometry of binding was determined to be one-to-one and the dissociation constant to be 406 nM.



Protein	k_a ($M^{-1}s^{-1}$)	K_d (s^{-1})	K_D (nM)
PfAtg8 ^{WT}	4.3×10^5	0.13	290
PfAtg8 ^{CM}	5.1×10^5	0.17	326

Figure 2.3. Comparison of PfAtg8 WT and CM binding to PfAtg3 with SPR-based Biacore studies.

MBP-PfAtg3 was immobilized on a CM3 chip and His₆-PfAtg8 variants were injected at six 2-fold serial dilutions in triplicate. Sensorgram shows response units over time of run. Orange lines indicate fit used by Scrubber data processing software (Biologic™ Software) to derive kinetics and dissociation constant, shown in table.

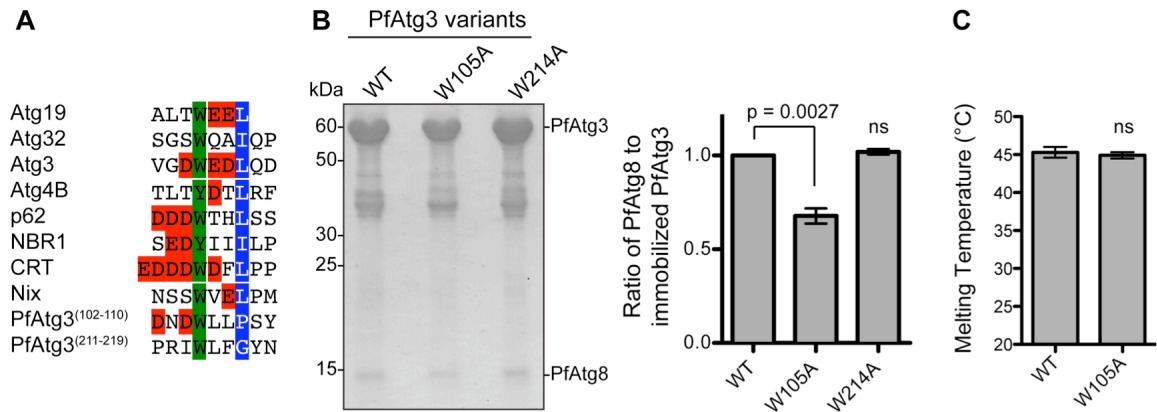


Figure 2.4. Identification of a putative AIM in PfAtg3. **A.** Alignment of known AIMs in other species with potential AIMs in PfAtg3. Aromatic residues at position 1 are denoted in green, hydrophobic residues at position 4 in blue, and acidic residues in red. **B.** *In vitro* MBP pulldown assay. His₆-PfAtg8^{CM} was co-expressed with MBP-PfAtg3 variants and purified with an amylose affinity column. Left: Bound proteins were subjected to SDS-PAGE and visualized with coomassie stain. Gel represents one of three independent experiments. Right: Binding was quantified with ImageJ as the ratio of PfAtg8 to PfAtg3, normalized to WT binding levels. Error bars represent means and standard deviation (SD) from three independent experiments. **C.** Thermal shift assay of His₆-PfAtg3 WT and W105A mutant. Error bars represent means and standard deviation (SD) from triplicate measurement.

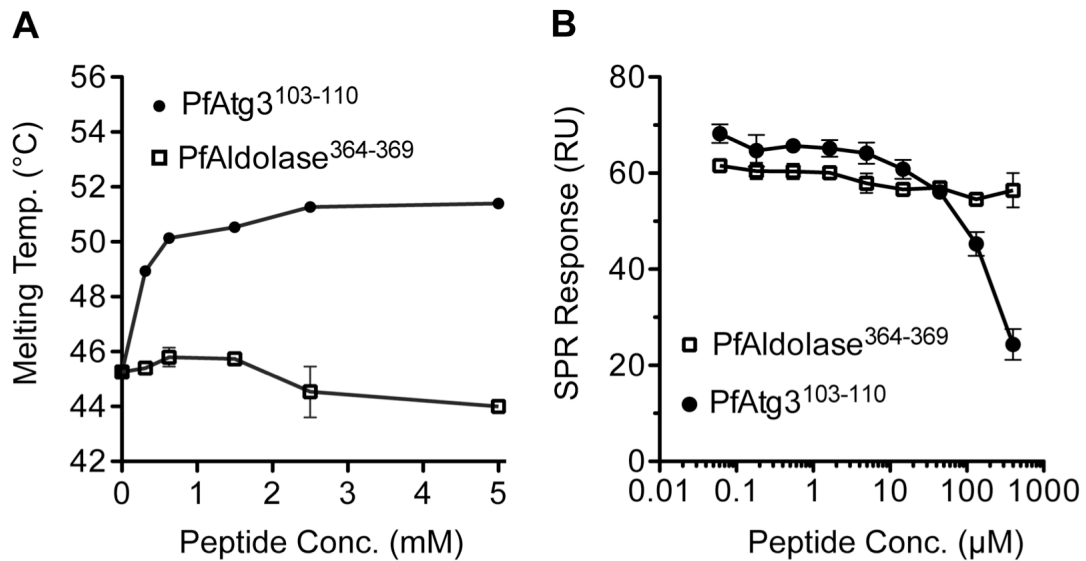


Figure 2.5. Identification of a PfAtg3 peptide that binds PfAtg8. **A.** TSA with peptides. His₆-PfAtg8^{CM} was incubated with increasing concentrations of PfAtg3 and PfAldolase peptides and fluorescence of SYPRO® orange dye was measured from 20-80°C over 60 min. **B.** SPR competitive binding assay. His₆-PfAtg8^{CM} was injected over an MBP-PfAtg3-conjugated chip with increasing concentrations of PfAtg3¹⁰³⁻¹¹⁰ or PfAldolase³⁶⁴⁻³⁶⁹ peptide and binding response was measured.

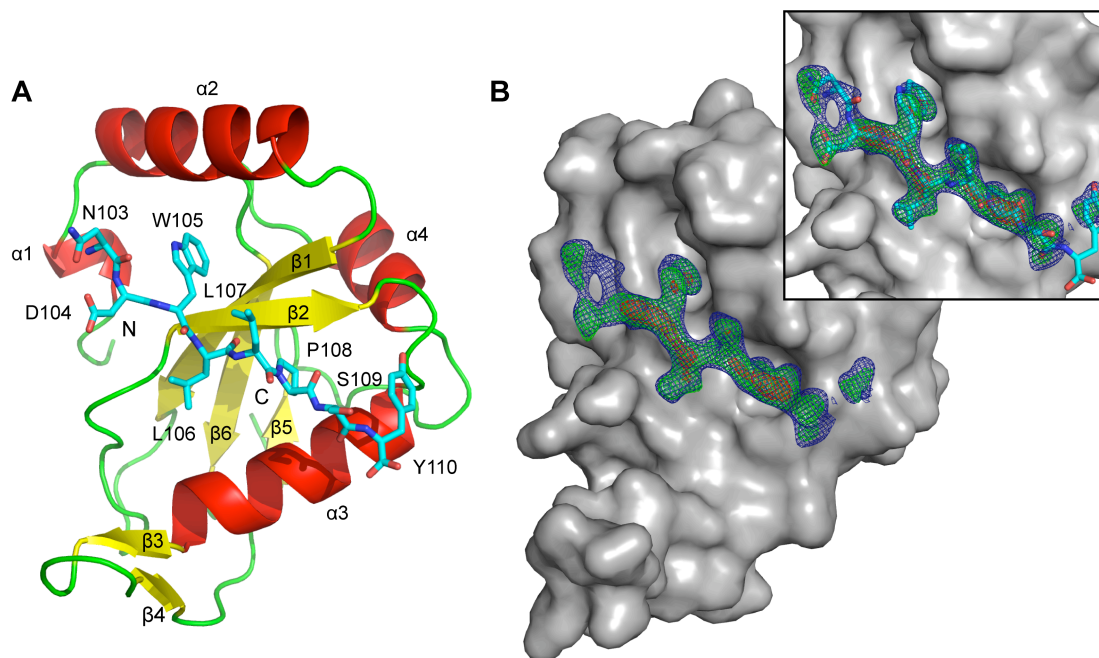


Figure 2.6. Overall structure of PfAtg8^{CM}-PfAtg3¹⁰³⁻¹¹⁰. **A.** The overall structure of PfAtg8^{CM} is shown as a cartoon representation with the PfAtg3-peptide as a stick model. Beta sheets are colored yellow and alpha helices colored red. **B.** Electron density corresponding to PfAtg3¹⁰³⁻¹¹⁰ peptide is shown bound to cargo receptor site of PfAtg8. 2Fo-Fc map electron density for peptide is shown in blue at 1 σ . Fo-Fc difference map is shown at 5 σ (red) and 3 σ (green) level. Stick model of PfAtg3-peptide is shown in inset.

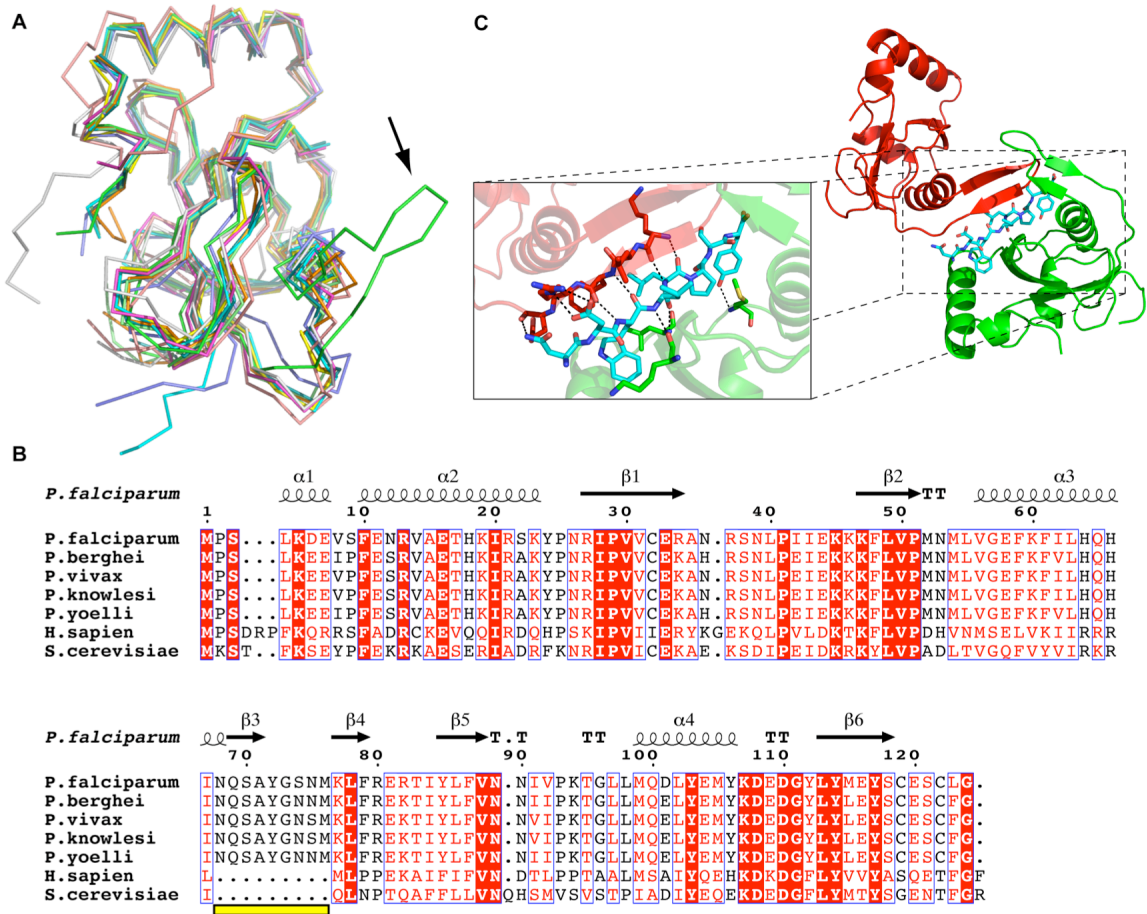


Figure 2.7. Identification of an Apicomplexan-specific loop in PfAtg8. **A.** Superposition of structures of Atg8 homologues (PDB code in paratheses) from *Saccharomyces cerevisiae* (2DYT), *Homo sapiens* (1GNU, 3ECI), *Bos Taurus* (1EO6), *Rattus norvegicus* (1UGM, 1KJT), *Bombyx mori* (3M95), and *Trypanosoma brucei* (3H9D) represented as ribbons. PfAtg8 is shown in lime green, with arrow highlighting loop absent in other structures. **B.** Multiple structural sequence alignment of Apicomplexa, human, and yeast Atg8 homologues. Plasmodial Atg8 homologues were aligned with *H. sapiens* LC3 and *S. cerevisiae* Atg8 using 3D-Coffee (www.tcoffee.org) (PDB codes 1EOY, 2ZJD, and 2ZPN, respectively) and visualized with ESPript (<http://esprict.ibcp.fr/ESPript/>). Structural elements shown above sequence are based on the PfAtg8 crystal structure. Loop region unique to Apicomplexa is highlighted in yellow. **C.** Crystal contacts between neighbor PfAtg8 molecules mediated by PfAtg3-peptide. Inset shows PfAtg3 peptide (cyan) hydrogen bond network with PfAtg8 A-loop residues in the nearest symmetry mate (red) as well hydrogen bond and hydrophobic interactions with the cargo receptor site of PfAtg8 (green).

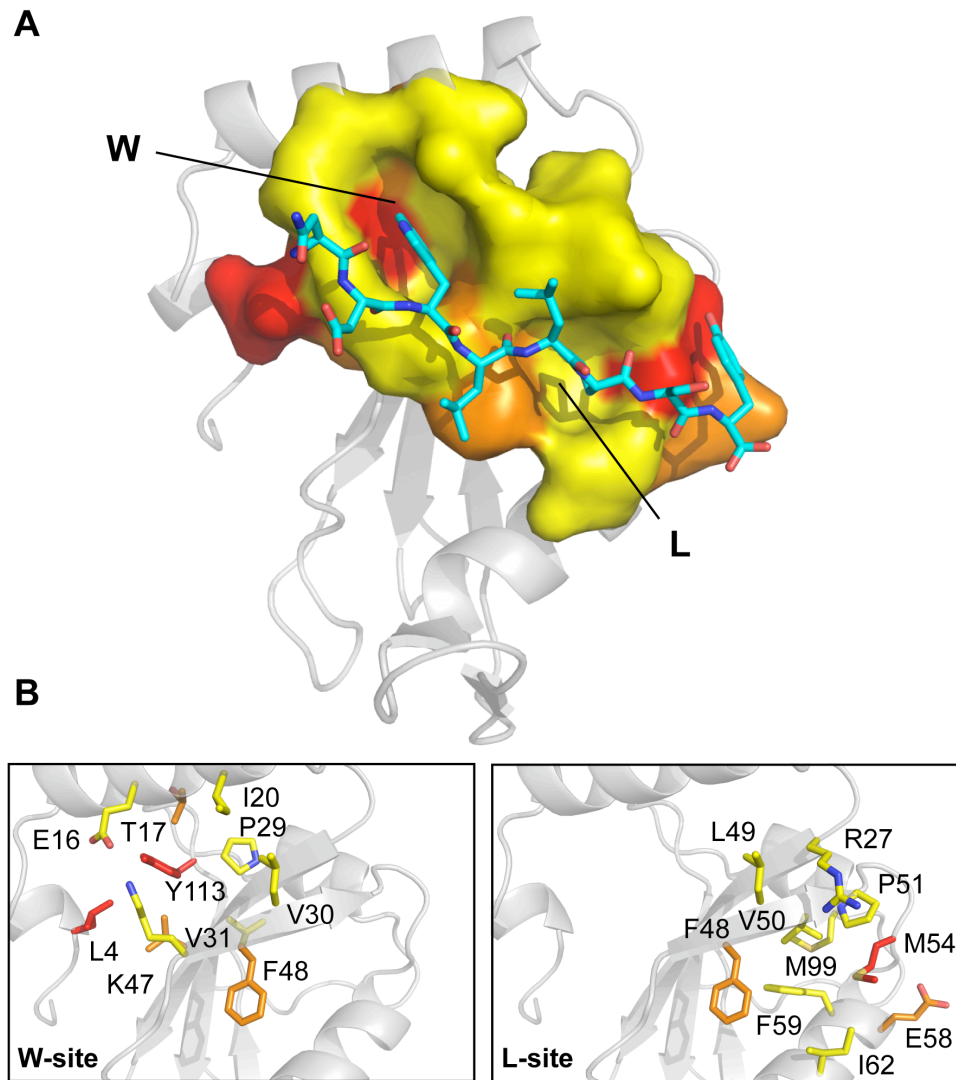


Figure 2.8. Analysis of the cargo receptor site of PfAtg8. **A.** The overall structure of PfAtg8 is displayed as a cartoon with the cargo receptor site as surface representation. The PfAtg3-peptide is shown in cyan. Residues are color-coded depending on presence in the human homologue, GATE-16; yellow = identical, orange = similar, red = different. **B.** Close-up of cargo receptor site. Residues composing the W- and L-sites are shown with the same color-coding for conservation as in A.

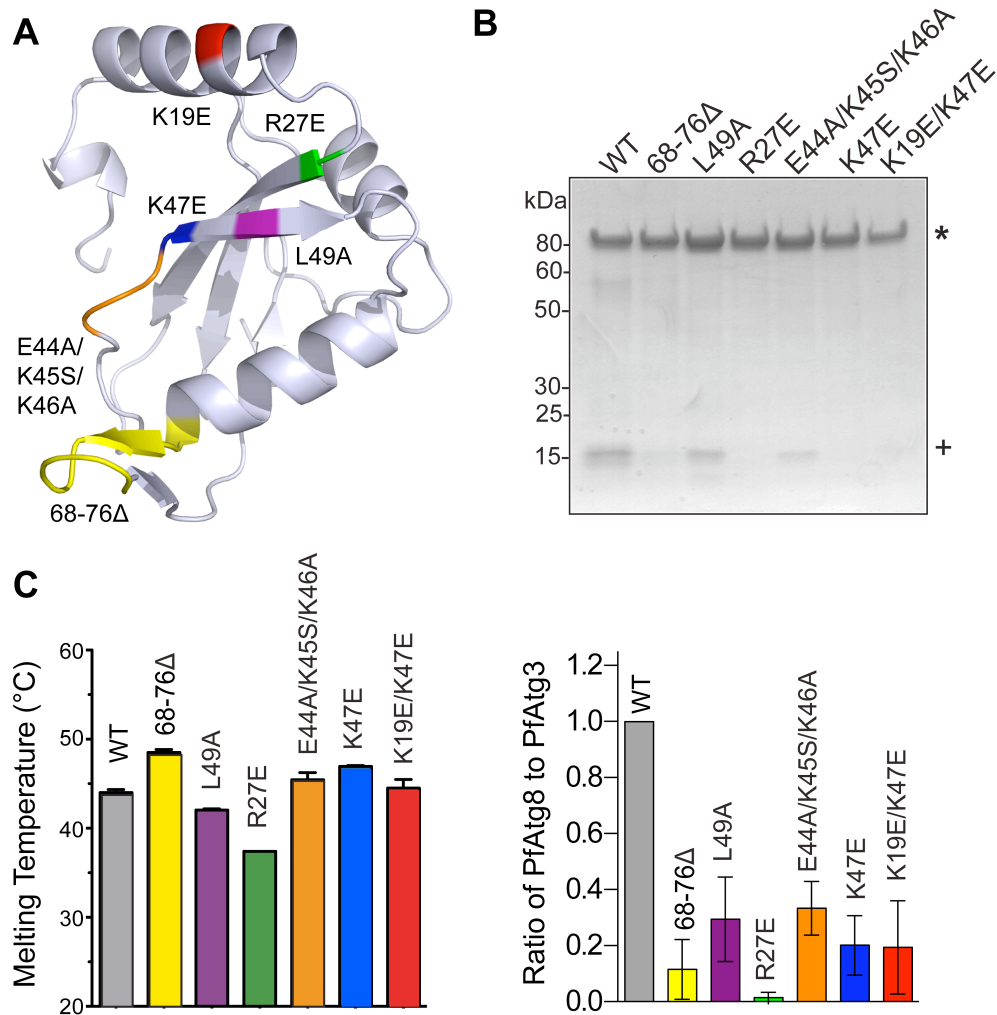


Figure 2.9. Identification of Atg3-interacting residues in PfAtg8. **A.** PfAtg8 mutations color-coded on the crystal structure. **B.** *In vitro* MBP pulldown assay. Immobilized MBP-PfAtg3 was incubated with His₆-PfAtg8 mutants. Bound proteins were subjected to SDS-PAGE. Asterisk denotes MBP-PfAtg3 and plus sign denotes His₆-PfAtg8. Gel is representative of three experiments. Bottom: Binding was quantified with as the ratio of bound PfAtg8 to PfAtg3, normalized to WT levels. Bars represent the mean and SD of three experiments. **C.** Thermal shift assay of PfAtg8 mutants. Mean and SD are shown for triplicate measurements.

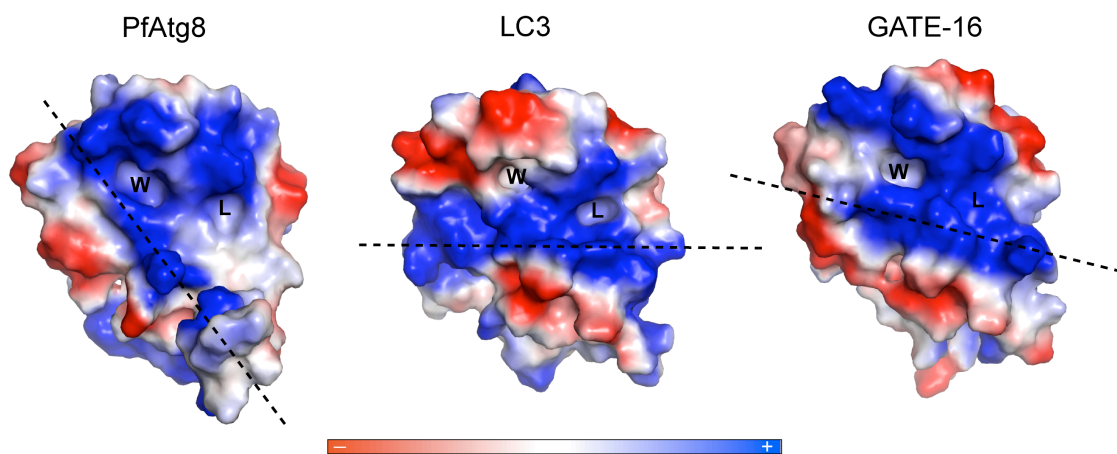


Figure 2.10. Electrostatic surface potential of Atg8 homologues. Dashed line indicates orientation of positively charged band in Atg8 homologues. The band is tilted 54° in PfAtg8 compared to LC3 and 41° to GATE-16.

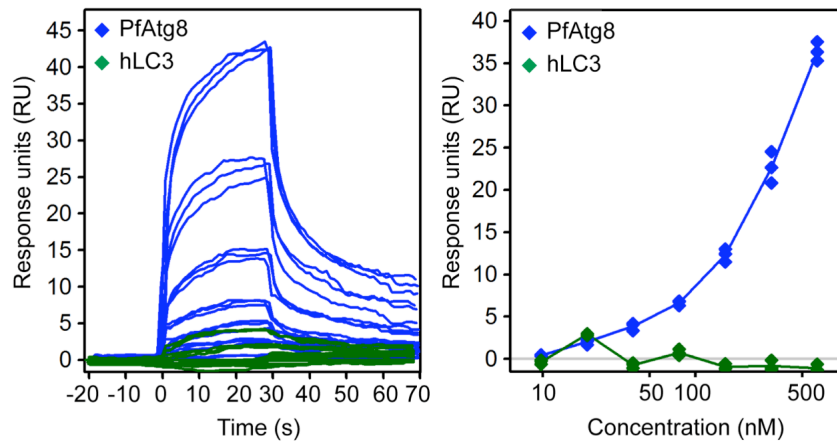


Figure 2.11. Human LC3 does not bind PfAtg3. Binding to the MBP-PfAtg3 CM3 chip was determined by SPR with triplicate injections of PfAtg8^{CM} (in blue) and hLC3 (in green) at seven concentrations. Left: SPR sensorgram. Right: dose-dependent binding curves for PfAtg8^{CM} and hLC3.

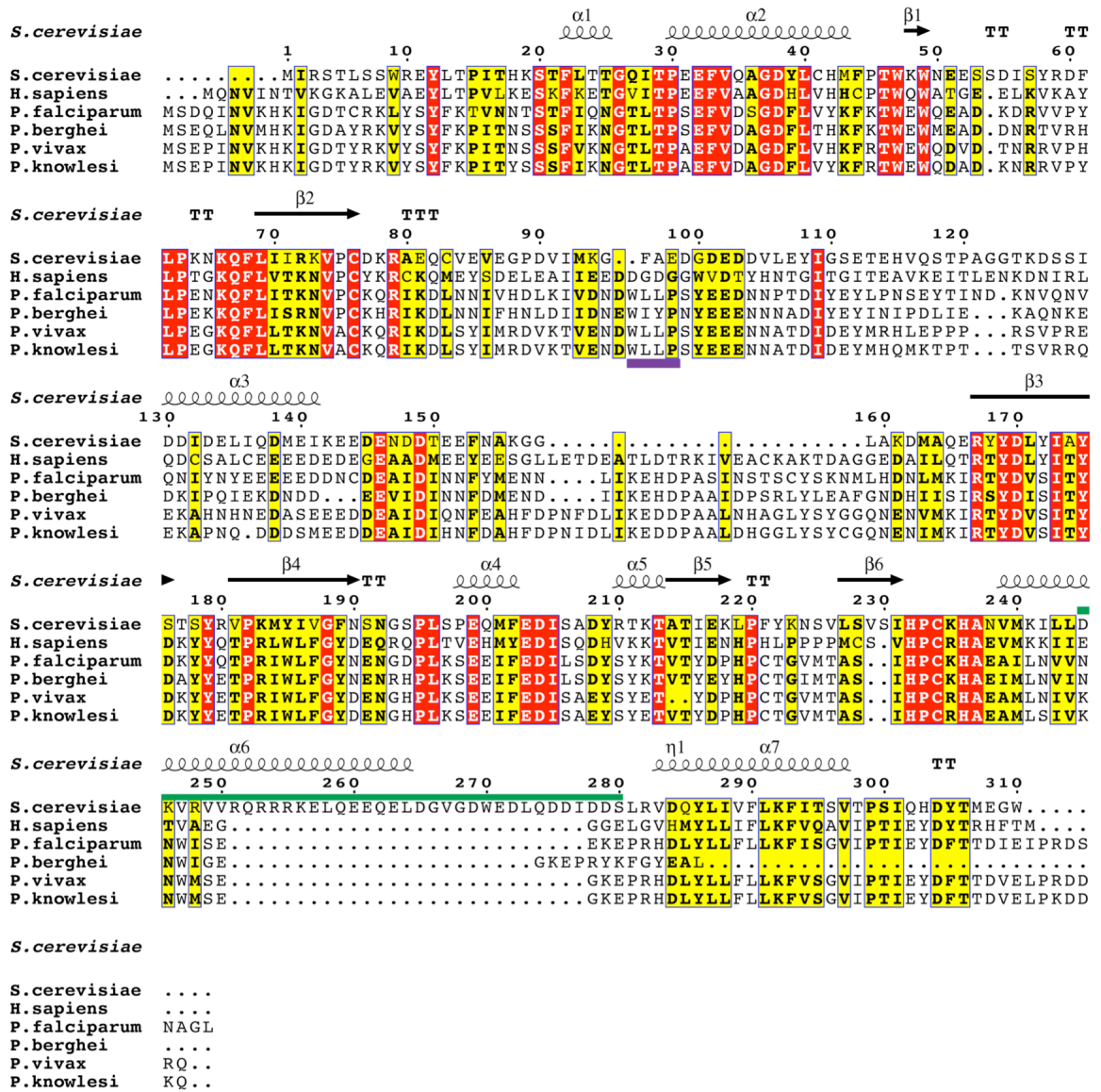


Figure 2.12. Multiple sequence alignment of Atg3 homologues. The newly identified AIM is marked with a purple bar and is conserved across *Plasmodium* species. Green bar denotes the handle region of yeast Atg3 shown to bind ScAtg8. Sequences were aligned with ClustalW2 (134) (<http://www.ebi.ac.uk/Tools/msa/clustalw2/>) and visualized in ESPript (<http://esprint.ibcp.fr/ESPript/>).

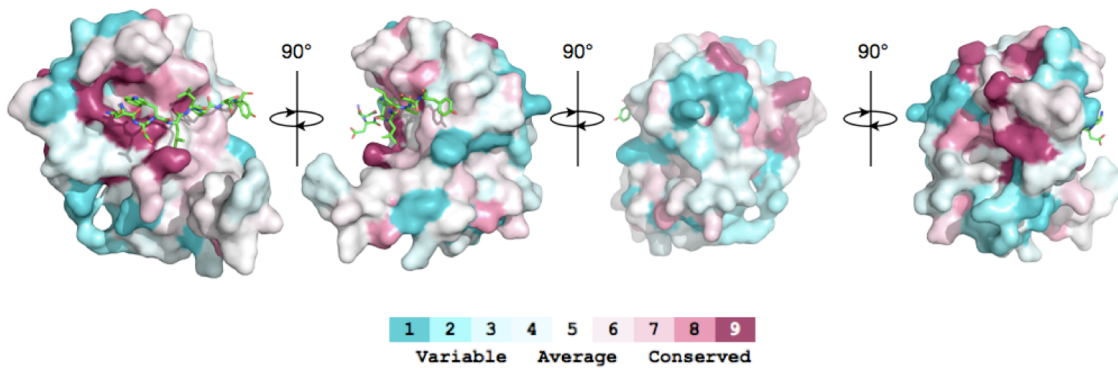


Figure 2.13. Conservation of PfAtg8 surface residues. Pf, Pv, and PbAtg8 and human homologues, LC3, GATE-16, and GABARAP, were aligned with ClustalW2 (134) (<http://www.ebi.ac.uk/Tools/msa/clustalw2/>) and visualized on the PfAtg8 structure using the ConSurf server (<http://consurf.tau.ac.il/>) (135, 136). PfAtg3¹⁰³⁻¹¹⁰ is shown as stick model in green. Abbreviations: Pf – *P. falciparum*, Pb – *P. berghei*, Pc – *P. chabaudi*, Pv – *P. vivax*.

Chapter 3

Identification of inhibitors against the plasmodial Atg8-Atg3 interaction

Sections currently submitted as:

Hain *et al.* Identification of an Atg8-Atg3 protein-protein interaction inhibitor from the MMV Malaria Box active in blood and liver stage *P. falciparum* parasites.
J Med Chem. 2013

Abstract

Atg8 is an ubiquitin-like autophagy protein in eukaryotes that is covalently attached (lipidated) to the autophagosome membrane. Autophagy is increasingly appreciated as a target in diverse diseases from cancer to eukaryotic parasitic infections. Much of the autophagic machinery is conserved in the malaria parasite, *Plasmodium falciparum*, including the conjugation pathway for Atg8 lipidation. Although Atg8's function in the parasite is not well understood, it is essential for *Plasmodium* growth and survival and localizes to the apicoplast, an indispensable organelle in Apicomplexans. We pursued independent strategies to identify unique inhibitors, such as fragment and library screening with SPR and *in silico* docking. Here we describe identification of inhibitors for the protein-protein interaction PfAtg8 and its E2-conjugating enzyme, PfAtg3. These inhibitors have demonstrated activity in blood and liver stage parasites.

Introduction

With vital and diverse roles in cell stress and survival, autophagy is seen as a potential target in many diseases, including cancer, neurodegeneration, and protozoan infections (68, 137, 138). The Atg8-Atg3 interaction has emerged as an important modulator of Atg8 lipidation and overall levels of autophagy. In mammals, the viral FLICE-like inhibitor protein (FLIP) binds Atg3 and competes for LC3 interaction to prevent LC3 lipidation and autophagy-mediated host cell death (139). We envision a similar strategy in developing a small molecule compound that will disrupt the Atg8-Atg3 interaction in the malaria parasite.

Although drug design has long focused on targeting enzyme active sites, PPIs are considered by many to be the next generation of drug targets (140). Targeting PPIs both increases the number of potential targets, as there are estimated to be approximately 400,000 PPIs in humans (141), and allows for selectivity. Recent successes such as completion of Phase II clinical trials by navitoclax against Bcl-2 family proteins demonstrate the specificity in targeting non-active sites (142). Navitoclax exhibits high affinity for Bcl-2, Bcl-X_L, and Bcl-w, but not the other Bcl-2 family prosurvival members, Mcl-1 and A1 (143). Other successes include inhibition of the BRD4/histone interaction in squamous carcinomas (144) and the MDM2-p53 interaction to slow tumor growth (145). Though the cancer field has led the way in PPI drug development, the strategy is being sought in other diseases, including HIV and parasitic infections (140, 146, 147).

There are several approaches to targeting a protein-protein interaction. *In vitro* high-throughput screening (HTS) against a molecular drug target is a popular choice as once the setup is established it is widely applicable to a range of drug targets and will likely lead to initial hits. However it does not provide molecular information of where and how the drug is binding the protein, making further optimization difficult. A powerful alternative is structure-based drug design (SBDD) because the binding mode is revealed. X-ray crystallography, nuclear magnetic resonance (NMR), or even *in silico* docking against the known structure are SBDD methods that can be used both for initial screening and optimization further down the drug design line. Figure A.1 diagrams an overview of the drug design approach from target identification to clinical trials.

Virtual library screening

Virtual library screening, an *in silico* method where compounds are docked to the known protein structure, has several advantages over empirical screening. Inherently virtual libraries can be much larger and more comprehensive than physical compound libraries. Although computation-intensive, compounds can be sampled more quickly. Additionally VLS is not dependent on the ability to obtain robust crystals for crystal soaking experiments or the stability of the protein in NMR experiments.

Unfortunately, there are also impediments to the success of VLS. The enormous flexibility inherent in receptor-ligand complexes makes screening all possible conformations difficult. However programs are increasingly able to handle these difficulties, rapidly sampling an exhaustive set of ligand conformations and using a range of rigid to semi-rigid to fully flexible protein receptors (148, 149). Although there are still

setbacks, VLS can predict known ligands for a given receptor correctly, docking them in the correct pose 40-60% of the time (150).

Fragment screening

Compared to typical drug-like compounds, screening molecular fragments, molecules between 100 to 300 daltons, samples chemical space more efficiently (151). Generally fragments follow the rule of three for hydrogen bond donors and acceptors, number of rotatable bonds, and ClogP, and have an upper limit on polar surface area of 60 Å² (152). Because of their smaller size, molecular fragments bind weakly, with K_{DS} in the 0.1 to 1 mM range but the ligand efficiency is expected to be high, allowing for optimization without surpassing a drug-like size (153, 154). Additionally, the likelihood of a hit is higher compared to HTS and allows for the development of compounds that would not have been identified otherwise (155). Of the fragment-based drug design (FBDD) successes in clinical trials, most target kinases (156, 157). PLX-4032, targeting the kinase B-Raf in metastatic melanoma is on course to become the first clinically approved drug arising from a FBDD program (158, 159). Examples of FBDD-derived compounds in phase 2 clinical trials include an Aurora kinase inhibitor for cancer, an agonist of proliferator-activated receptor in type 2 diabetes, and the PPI inhibitor, navitoclax against Bcl-2/Bcl-xL in cancer (142, 160, 161).

Fragment-based approaches center on the ability to “grow” the molecule in steps using structure-activity relationships (SAR) and SBDD to eventually create a potent drug-like molecule. The anticipation is the creation of a more efficient ligand than would have been identified through traditional drug screening approaches. Alternatively, one

can identify fragments that bind in two nearby pockets and link them together. While this method has been successful, it is important to ensure the linker does not strain the attached molecules or change their orientation (162-165). If the pockets are too far apart the tethered molecule may be too large to be bioavailable and cell permeable.

The most well known methods to identify fragments are NMR, SPR, and X-ray crystallography. In fragment cocktail crystallography (FCC), protein crystals are soaked with a milieu of small molecular weight compounds. Changes in electron density indicate binding to the crystallized protein. While extremely powerful in terms of providing detailed knowledge on binding mechanism, FCC is dependent on the ability to obtain reliable, well-diffracting crystals of the protein. Additionally, this method may miss molecules that destabilize the crystal lattice and prevent diffraction.

SPR experiments have become a standard technique for fragment and drug screening, especially in industry. Detection of binding by SPR typically involves immobilization of one ligand onto an SPR chip. The analyte is passed over the immobilized protein ligand and changes in refractive index near the surface, due to ligand binding, is read out as SPR response. A great strength is that the Biacore sensor is sensitive enough to measure binding of molecular fragments around 100 daltons to a protein many times its size as long as a high density of immobilization is reached, described by the following formula. Maximal SPR response (RUs) = $(MW_{\text{Analyte}}/MW_{\text{Ligand}}) \times \text{stoichiometry of binding} \times R_L$, where R_L is the amount of immobilized ligand in RUs.

Previous studies using simultaneous approaches of empirical and virtual screening have identified distinct classes of ligands that would have been overlooked by either

approach alone (166). Pursuing a multi-pronged approach of *in silico* and *in vitro* screening combined with SBDD will increase the probability of identifying novel inhibitors of the *Plasmodium* autophagy system. Our structural and biochemical studies presented in Chapter 2 suggested the PfAtg8-PfAtg3 interaction was exploitable to selectively target the plasmodial interface and laid a foundation for use of SBDD.

Results

We attempted to obtain crystals suitable for soaking experiments. The PfAtg8 crystals obtained in Chapter 2, with the PfAtg3¹⁰³⁻¹¹⁰ peptide did not diffract reliably, requiring time-consuming screening of identical crystals at the synchrotron source. Additionally, the presence of the PfAtg3-peptide in the crystals prevents soaking with compounds competing for the W- or L-site. We attempted to optimize these crystals and obtain crystals of PfAtg8 alone for crystallography soaking experiments. Numerous constructs (Table A.3), purification schemes, matrix screens, and additives failed to yield diffracting crystals. While continuing to pursue this extremely powerful structural technique, we undertook alternative methods to identify inhibitors.

Identification of PfAtg8-binding fragments

We chose to screen a library of 352 small molecular fragments from Zenobia Therapeutics, Inc. with an average molecular weight of 150 Da because of the high solubility, non-toxic nature, and functional diversity of the compounds as well as the compatibility of the library with fragment-based co-crystallization experiments. We utilized SPR-based differential fragment screening in order to identify fragments that bind the W-site of PfAtg8, important for the Atg8-Atg3 interaction. Binding of injected molecules to immobilized His₆-PfAtg8^{WT} and the W-site mutant His₆-PfAtg8^{K19E/K47E} was compared (Figure 3.1A,B). Hits eliciting 1.5 x's the response (RU) over noise and 1.5 x's greater normalized binding for wild type than mutant were further validated for PfAtg8 binding with TSAs (Figure 3.1C). Likely due to the high internal fluorescence of

F410 and F470, we were not able to measure the effect of these compounds on the T_m of PfAtg8. Three fragments, F268, F408, and F537, showed significant binding in the TSA and were tested, along with F410, for their ability to inhibit the PfAtg8-PfAtg3 interaction in SPR competition studies. PfAtg8^{CM} was injected at a constant concentration over the MBP-PfAtg3 chip with an increasing concentration of fragments F268, F408, F410, and F537. While F268 and F537 showed no inhibition, two benzenetriols led to dose-dependent inhibition (Figure 3.1D). F410, benzene-1,2,3-triol and F408, benzene-1,2,4-triol, inhibited the PfAtg8-PfAtg3 interaction with an IC_{50} of 150 μ M and 1 mM, respectively. With higher concentrations of F410, the response levels off and slightly increases with the highest concentration. This was due to F410 binding to the MBP-PfAtg3 chip as injection of F410 alone led to a concentration-dependent response (Figure A.2). Therefore the actual IC_{50} may be lower.

Optimization of hydroxybenzene fragments with an oxime library

In lieu of structural information of benzenetriol's binding mechanism, we sought to screen for more potent hydroxybenzene derivatives. We utilized an oxime library approach, where two aldehyde building blocks are linked together through dialkoxamine linkers to create a bivalent library (167). Our lab had previously synthesized an oxime screen together with Dr. J. Stivers (Johns Hopkins School of Medicine) for another molecular target. The R_1 group, 3,4-dihydroxybenzaldehyde, was similar to the benzenetriols we identified in our Zenobia fragment screen leading us to screen this library against PfAtg8-PfAtg3 (Figure 3.2A). 3,4-dihydroxybenzaldehyde was tethered to

240 different R₂ aldehydes with linker lengths ranging from two to four carbons (Figure 3.2B).

We screened the library using a surface plasmon resonance (SPR)-based competition assay where PfAtg3 is immobilized onto an SPR chip and PfAtg8^{CM} is injected in the presence of DMSO or a compound and binding is measured by the SPR response. Three compounds led to at least 50% inhibition in binding, two of which were derivatives of benzenetriols, similar to our Zenobia fragment hits (Figure 3.2C). Follow-up experiments failed to validate dimethylbenzaldehyde as a hit but confirmed inhibition by 3,4,5-trihydroxybenzaldehyde.

In the original screen, each well contained a mixture of 12 reactants because of the varying linker lengths and the formation of heteromeric and homodimeric compounds. We sought to deconvolute which of the linker length species led to the observed inhibition. Reactions were set up with only one linker length and tested with SPR. Binding was decreased the most with a three-carbon linker but the difference was not significant (Figure A.3A). In thermal shift assays, all of linker length species increased the melting temperature of PfAtg8 (Figure A.3B). Therefore, it is unclear which of the linkers are responsible for inhibition in the original screen. We set up co-crystallization matrix screens of PfAtg8^{CM} with the two and three-carbon species individually. Several conditions led to crystals in one or both of the compounds, absent in the protein only control, but these crystals did not diffract at the SSRL synchrotron source.

Virtual library screening to identify Plasmodial Atg8 inhibitors

Because the A-loop region of PfAtg8 is divergent from human Atg8 homologues, we sought to identify A-loop-binding compounds. Using our crystal structure (PDB code 4EOY), a PfAtg8 receptor was prepared in fred_receptor (www.eyesopen.com) for *in silico* docking studies (168). A suite of libraries consisting of FDA-approved drugs, the Medicines for Malaria Venture (MMV) malaria box, and Chembridge CORE, totaling nearly 400,000 compounds, was docked against the receptor with FRED (www.eyesopen.com) (168) (Figure 3.3A). VLS hits were ranked according to chemgauss3 score, known toxicity data, diversification, predicted solubility, and balance between polar and apolar interactions. Fifteen compounds were purchased from Hit2Lead and tested *in vitro* for inhibition of the PfAtg8-PfAtg3 interaction using SPR (Figure 3.3B). Many of the compounds predicted to bind PfAtg8 led to inhibition. C25 and C24, the best hits, were chosen for verification of dose-dependent inhibition of the interaction. Only C25 led to dose-dependent inhibition with an IC_{50} of $18.5 \pm 2.1 \mu\text{M}$ (Figure 3.4A). C25 led to dose-dependent decrease in the T_m of PfAtg8^{CM}, measured in thermal shift assays, indicating binding to PfAtg8, but also that the compound may not be well suited for co-crystal matrix screening due to its destabilizing effect on PfAtg8 (Figure 3.4B). Of note, C25 had the second highest ranking in the original docking screen, docking pose is shown in Figure 3.4C,D.

Identification of inhibitors from the MMV Malaria Box library

The MMV Malaria Box of 200 drug-like and 200 probe-like molecules was screened with our established SPR-based competition assay against the PfAtg8-PfAtg3 interaction (Figure 3.5A) (169). Compounds leading to at least twenty-five percent

inhibition of binding were further tested for dose-dependent inhibition using SPR (Figure 3.5B). Three of the six primary hits demonstrated a constant level of inhibition independent of concentration of the small molecule and were not further investigated. The other three compounds led to dose-dependent inhibition with an SPR inhibitory concentration ranging from six to 18 μ M (Figure 3.5C). Interestingly, these compounds shared a common scaffold: 4-pyridin-2-yl-1,3-thiazol-2-amine (abbreviated here as PTA), incorporated as the N-substituent in various anilines or benzamides. For simplification we will refer to these compounds based on their plate ID and well position in the MMV May 2012 plate setup: PAH9 (N-(4-methylphenyl)-4-pyridin-2-yl-1,3-thiazol-2-amine), PAC5 (2-methylsulfanyl-N-(4-pyridin-2-yl-1,3-thiazol-2-yl)benzamide), and PBB8 (2-bromo-N-(4-pyridin-2-yl-1,3-thiazol-2-yl)benzamide) (Table 3.2). Hits were tested for their effect on the stability of PfAtg8^{CM} using fluorescence-based thermal shift assays (TSAs). None of the compounds significantly affected the melting temperature (T_m) indicating the compounds did not impact the tertiary structure of PfAtg8 (Figure 3.5D).

Determination of the PTA binding site on PfAtg8

We tested whether these compounds bound directly to PfAtg8 using SPR. PfAtg8^{CM} was immobilized onto an SPR Ni-NTA chip via a twelve histidine N-terminal tag. PAH9, chosen for its better solubility, was injected over the chip and binding was measured. PAH9 led to a dose-dependent increase in SPR response, indicating binding to PfAtg8^{CM} (Figure 3.6A). We next sought to determine the binding site for the PTA compounds with *in silico* docking.

The OpenEye software package (www.eyesopen.com) (168) was used to dock conformers of the compounds against the X-ray structure of PfAtg8 (PDB code 4EOY) (45). All three compounds docked to the W-site of PfAtg8 (Figure 3B). PBB8 and PAC5 bound with the pyridine ring in the W-site, whereas PAH9 was predicted to bind with the pyridine ring in the L-site, the thiazole ring positioned between the pockets and the methylbenzene group in the W-site. An alternate pose was enriched within the top ten poses output by the docking study, where PAH9 is contained solely within the W-site in a more compact conformation. It is worth mentioning that PAH9 is missing a donor oxygen compared to PBB8 and PAC5 and therefore may adopt a different mode of binding to the W- and L-sites of PfAtg8. PAC5 docked with the pyridine ring in the W-site and the methylsulfanylbenzene group bound to the L-site of PfAtg8. Docking was repeated using a version of the receptor for which the carbonyl of Lys47 was defined as a hydrogen bond acceptor constraint (Figure BA inset). PBB8 had the same docking pose in both studies. PAH9 had similar binding pose to the highest ranked pose from the unconstrained docking, while PAC5 was slightly different, with the pyridine ring rotated 90° in the W-site and the benzene ring positioned just below and to the left of the L-site pocket, with the methylsulfanyl group reaching into the mostly hydrophobic L-site.

Synthesis of a novel PTA derivative with a functional handle

Our studies indicated that the PTA scaffold is a good platform for hit-optimization. David Bartee in Dr. C. Myers laboratory (Johns Hopkins University) synthesized a PTA-benzaldehyde derivative, 4-formyl-N-(4-pyridin-2-yl-1,3-thiazol-2-yl)benzamide with a functional handle extending off the common hydrophobic ring

system, termed PTA-AL (Table 3.2, Figure 3.7A). PTA-AL was prepared from commercially available PTA and 4-formyl benzoic acid through a DCC-promoted amide coupling. The benzaldehyde derivative, PTA-AL, can be tethered through a dialkoxymine linker to a library of aldehydes and screened using our primary SPR competition assay against the PfAtg8-PfAtg3 interaction (167). Docking against PfAtg8 suggests it is possible for an extension of the aldehyde to occupy the A-loop pocket (Figure 3.7B). A gain in parasite selectivity for such bifunctional analogs is expected as the A-loop is missing in the human Atg8 homologues (45). To confirm binding to PfAtg8, we tethered PTA-AL to (+)-biotinamidohexanoic acid hydrazide (BACH), through its reactive aldehyde group and tested binding with SPR. The biotinylated PTA compound, PTA-Biotin, was immobilized onto a neutravidin coupled SPR chip. His₁₂-PfAtg8^{CM} injected at various concentrations PfAtg8^{CM} led to a dose-dependent increase in SPR response, indicating PfAtg8 directly binds PTA-Biotin (Figure 3.7C).

Dr. C. Myers lab then converted PTA-AL to the hydrochloride salt and subjected it to acid-catalyzed acetal formation with methanol and trimethyl orthoformate under microwave irradiation to provide the dimethyl acetal PTA-D0, an unreactive derivative, to confirm activity of the starting platform (Table 3.2, Figure 3.7A). PTA-D0, 4-(dimethoxymethyl)-N-(4-pyridin-2-yl-1,3-thiazol-2-yl)benzamide, has similar shape and distribution of acceptor and donor pairs as the original PTA compounds. Docking of the unreactive PTA-D0 compound suggested similar binding to the W- and L-site of PfAtg8 as PAC5 with the functional group for extension pointing in direction of the A-loop pocket (Figure 3.7B). SPR studies confirmed PTA-D0 inhibited the PfAtg8-PfAtg3 interaction with an IC₅₀ of 2.86 μ M in SPR (Figure 3.7D).

Inhibition of Plasmodium blood stages

The IC₅₀s for the MMV compounds in *P. falciparum* 3D7 blood stages are previously reported and located on the NCBI PubChem database (<http://pubchem.ncbi.nlm.nih.gov>). The reported IC₅₀ for PBB8 ranged from 1.36 to 4.52 μM, while PAC5 ranged from 0.20 to 6.8 μM (PubChem bioassay ID (AID): 660866 and 449707) (170). PAH9 has a reported IC₅₀ of 350 to 400 nM (PubChem AID: 660866 and 449703) (171). We focused on PAH9 for further studies because the reported cytotoxicity in human cell lines is much lower compared to PAC5 and PBB8 (PubChem AID: 660872, 685525, and 449705).

We measured growth inhibition of *P. falciparum* 3D7 blood stage cultures by C25, PAH9, PTA-D0, and the well-characterized antimalarial chloroquine (CQ) using the SYBR green I assay (172) in collaboration with Dr. D. Sullivan (Johns Hopkins University, USA). This assay exploits the absence of nuclei in erythrocytes with a fluorescent dye that is unquenched upon binding to nucleic acids, preferentially double-stranded DNA. In two of three independent experiments, the IC₅₀ of PAH9 was 768 nM, similar to previously published results, while in a third experiment, the IC₅₀ was 3.3 μM, resulting in an average IC₅₀ of 1.61 μM ± 1.47 (171). PTA-D0 had a similar potency as PAH9 against the blood stage of *P. falciparum*, with an average IC₅₀ of 1.48 ± 0.6 μM. C25 was less potent with an IC₅₀ of 19 ± 6 μM. In our assay CQ had an IC₅₀ of 3 ± 2 nM (Figure 3.8).

Inhibition of Plasmodium liver stages C25 and PAH9

PfAtg8 is expressed and lipidated during the liver stage where it partially localizes to the apicoplast (38). Treatment of early liver stage parasites with the autophagy inhibitor 3-methyladenine is reported to delay conversion of the parasite into its trophozoite form (36). We therefore hypothesized that our PPI inhibitors PAH9 and C25 would have activity against the liver stage. PAH9 was previously tested in *P. yoelii* liver stage cultures and did not display >50% inhibition at the screening concentration of 10 μ M; an IC₅₀ was not reported (pubchem AID: 602118 and 602156) (173, 174). *P. yoelii* and *P. berghei* are often used to test drugs for liver stage inhibition as they are easier to culture. However, these are rodent malaria models and may not be indicative of activity in *P. falciparum*. Analysis of the W/L-site revealed differences in the amino acid composition that could affect drugs predicted to bind in that region (Figure A.4). We utilized a recently established *P. falciparum* liver stage *in vitro* model whereby sporozoites isolated from infected mosquitos' salivary glands invade HC-04 hepatocytes (175). HC-04 is a unique immortalized cell line, with expression of biochemical markers characteristic for normal hepatocytes, allowing the full development of the human malaria parasite, *P. falciparum* (175-177).

With the help of Dr. J. Levitskaya (Johns Hopkins University, USA) we used this system to assess the effect of PAH9 and C25 on the development of *P. falciparum* 3D7-GFP parasites (178) in human hepatocytes cultures. No change in the viability of HC-04 cells was detected in response to treatment with 3 μ M or 30 μ M of PAH9 or C25 during the 96 hr treatment (Figure 3.9). We observed a 45% reduction in the proportion of hepatocytes infected with *P. falciparum* 3D7-GFP sporozoites (GFP+/PI- cells) in response to treatment with 30 μ M, but not 3 μ M of PAH9 (Figure 3.10A). Additionally,

there was a dose-dependent reduction in the intensity of GFP fluorescence at both concentrations of PAH9, indicating inhibition of parasite development within hepatocytes, at least *in vitro* (Figure 3.10B). C25 had little effect on GFP fluorescence intensity, but did decrease the number of infected cells by 30% at 30 μ M (Figure 3.10A,B). Because C25 and PAH9 did not affect cell survival or cell growth of HC-04 cells, the compound's effect on the parasite is unlikely to be a result of host cell toxicity.

Validation of drug effect on PfAtg8 in parasite cultures

We next sought to determine whether PAH9 or C25 had a direct effect on PfAtg8 in *P. falciparum* blood stage cultures. In immunoblot assays, we observed a very faint band corresponding to PfAtg8 in DMSO-treated control cells (Figure 3.11). Incubation of cells in minimal media lacking human serum for six hours led to a very slight increase in PfAtg8. In contrast, treatment with 50 μ M PAH9 for five hours led to a drastic increase in PfAtg8 protein levels as well as a shift in mobility, likely corresponding to the unlipidated form of PfAtg8. PfAtg8 protein levels were also increased, though not to the same extent with 100 μ M C25 and led to a similar shift in mobility. We also looked at heat shock protein 70 (PfHsp70) in treated cells. Interestingly, PfHsp70 was present at the expected molecular weight of 73 kDa in control and starved cells, while PAH9-treated cells had a fainter band at this size and a prominent band at 35 kDa, possibly indicative of a cleavage product.

Attempts to obtain structural information

Although crystals of PfAtg8 with our compounds have not been obtained, nuclear magnetic resonance (NMR) could alternatively be used to provide molecular information on binding. Prior to solving the structure of PfAtg8-PfAtg3¹⁰³⁻¹¹⁰ with X-ray crystallography, we pursued NMR experiments on PfAtg8^{CM} with the help of Ananya Mayumdar at the JHU NMR facility. The initial ¹H-¹⁵N Heteronuclear Single Quantum Coherence (HSQC) 2D spectrum showed a good dispersion of peaks, indicative of a well-folded protein, but Atg8 was subsequently found to be too unstable to collect a complete data set and acquisition of NOESY spectrum was not possible (Figure A.5). This was due to irreversible precipitation of PfAtg8 above 25°C after 24 hours, leading to a low signal to noise ratio. However, data collection at lower temperatures may allow for sufficient protein stability in the future. Potentially, the binding site for C25, benzene-1,2,3-triol, PAH9, and the PTA-derivatives could be determined with NMR.

Discussion

Targeting protein-protein interactions has long been overlooked in the drug development field. PPIs usually involve shallower pockets and a more extensive network of residues than enzymatic active sites so that a small molecule must mask an area of 800-1000 Å² to competitively inhibit the interaction (156). However PPIs are less conserved than active sites (179), offering the opportunity for more selectivity, an important concept when targeting a eukaryotic parasite protein within a eukaryotic host. Using a combination of approaches, we have identified three starting platforms against the PfAtg8-PfAtg3 interaction.

Two benzenetriols were identified from the Zenobia fragment screen as inhibitors against the PfAtg8-PfAtg3 interaction. Benzene-1,2,3-triol showed the greatest inhibition with an IC₅₀ of 150 μM. Our SPR experiments suggest the fragments compete for binding of Trp105 of Atg3 in Atg8's W-site. The observed inhibition of our fragments falls within the expected range for small molecule fragments (153, 180). Benzenetriol was independently identified as a hit in our oxime library screen. Although the screen was chosen because of the similarity of R₁ group to the benzenetriol, it appears the benzenetriol and benzenediol, at least when combined in a divalent molecule, bind in different pockets.

We also used an *in silico* approach to target the A-loop pocket of PfAtg8. This approach led to the discovery of a compound that inhibits the Atg8-Atg3 interaction and shows activity in blood and liver stages. Though the potency is sub-optimal, C25 was well tolerated in human liver cells at high micromolar concentrations. It may be

worthwhile to pursue optimization of C25 through SAR studies and would be of great interest to determine if C25 binds the A-loop pocket, as predicted in our docking studies. C25 may be better suited as a molecular probe to elucidate the function of PfAtg8 during different stages of the malaria life cycle as its function is currently unclear (181).

Using *in vitro* screening, we identified PTA, N-(4-methylphenyl)-4-pyridin-2-yl-1,3-thiazol-2-amine, as a scaffold inhibiting the PfAtg8-PfAtg3 interaction. We demonstrated activity in blood- and liver-stage *Plasmodium* parasites by one PTA compound, PAH9. All PTA-containing MMV compounds had a Ligand Efficiency by Atom Number (LEAN) score greater than 0.3 in the blood stage, indicative of high ligand efficiency and a promising starting point for expansion (182). PAH9 was previously reported to have low cytotoxicity with a LD₅₀ (lethal dose) of 18.2 μM in HepG2 cells and half maximal cytotoxic concentration (CC₅₀) and IC₅₀ of 32 μM in Huh7 cells (PubChem AID: 685525, 660872, 449705). PAH9 only inhibited liver stage parasites significantly within the reported cytotoxic range in human cells, although no cell death was observed in HC-04 cells at these concentrations in our study.

Treatment of *P. falciparum* with high levels of PAH9 led to a drastic increase in, presumably unlipidated PfAtg8 protein levels. This increase could be due to an up-regulation of PfAtg8 synthesis to compensate for inhibition or a buildup of existing protein levels due to a blockade in autophagic degradation. In yeast, nitrogen starvation leads to induction of Atg8 expression while inhibition of later stages of autophagy leads to accumulation and even greater protein levels of Atg8 (183, 184). Further studies are necessary to determine if PfAtg8 is upregulated at the transcriptional, translational, or degradation level in response to PAH9 treatment. The intriguing effect of PAH9 on

PfHsp70 was unexpected and may indicate a cellular response to stress induced by inhibiting Atg8 lipidation. The putative Hsp70 cleavage fragment of ~30-35 kDa is reminiscent of Hsp70.1 cleavage observed in hippocampal cornu *Ammonis* neurons in response to ischemic stress. Hsp70.1 in these cells is carbonylated and cleaved by μ -calpain, leading to lysosomal rupture, release of cathepsin, and subsequent neuronal death (185). It is premature, yet tempting, to envision a similar stress pathway in *Plasmodium* activated under prolonged exposure to high concentrations of PAH9. It has been previously shown that cytotoxic levels of CQ leads to food vacuole permeabilization and features of programmed cell death in *P. falciparum* (186). In the future, we could examine Hsp70 fragmentation under CQ treatment.

Of note, the IC_{50} of PAH9 in parasite cultures was lower than the IC_{50} measured with SPR. This could be due to an accumulation of the drug inside the parasite or because even slight inhibition of PfAtg8 lipidation has drastic effects on parasite growth, similar to reaching the tipping point on a balance or could be due to off-target effects. The IC_{50} of C25 and PTA-D0 was in good agreement in the SPR and parasite growth assays.

Autophagy is increasingly being targeted in certain types of cancer (187). Our identified inhibitors, and their derivative compounds will be tested for inhibition of the human Atg8-Atg3 interaction *in vitro* to determine toxicity and alternative utilization as leads in cancer drug development.

Future directions:

We are currently in the process of creating an oxime library with our PTA-AL derivative in collaboration with Dr. C. Myers (Johns Hopkins University). Because of the

difficulties deconvoluting the dihydroxy screen, we will synthesize the PTA-AL screen to contain one species per well. In the near future, this library will be screened using the Atg8-Atg3 SPR-competition assay with the hopes of identifying a compound with better inhibition in the asymptomatic liver stage. It is of great interest to test these inhibitors against *P. vivax* dormant hypnozoite forms, though these studies would be more cost intensive, requiring a mouse model.

Now that we have identified promising candidates, it is crucial to obtain structural information to guide further changes. The ability to synthesize the PTA derivatives in collaboration with Dr. C. Myers, allows us to pursue co-crystallization matrix screens. Table A.3 illustrates the numerous constructs of PfAtg8 that we have attempted to crystallize. Some of these constructs could be re-screened with our inhibitor molecules. In addition to its potential for development into a therapeutic drug, PAH9 could serve as a tool to elucidate the biological function of PfAtg8. Chapter 4 present preliminary results using PAH9 as a molecular probe.

Methods & Materials

SPR: SPR runs were conducted on a Biacore 3000 instrument (GE Healthcare). Unless otherwise stated, runs were performed in running buffer 2 (RB2) containing 354 μM KH_2PO_4 , 1.87 mM Na_2HPO_4 , 51.5 mM NaCl , pH 7.4, 0.01% v/v P20, 0.2 mg/ml BSA at 25°C (Quality Biologicals). See Chapter 2 Methods & Materials for RB1. Bound analyte was dissociated from the chip using 1 injection of 1 M MgCl_2 followed by 2 blank injections of RB between each concentration. Binding and equilibrium constants were determined with Scrubber (BioLogic™). A double referencing method was applied to correct for nonspecific binding to the chip with interspersed blank injections correcting for baseline drifts. Changes in refractive index from DMSO were adjusted with a DMSO calibration curve.

Identification of fragments that bind Atg8 near the cargo receptor site: His₆-PfAtg8 WT and K19E/K47E were immobilized with maximal levels onto different flowcells of an NTA-Chip (GE Healthcare) preconditioned with nickel. A library of 352 fragments (library 1 from Zenobia Therapeutics, Inc.) was screened for binding at a concentration of 0.1 mM diluted in running buffer containing 50 mM HEPES pH 8, 50 mM NaCl , 3% DMSO, 0.005% v/v P20. 50 μL of each compound was injected at 20 $\mu\text{L}/\text{min}$ and dissociation time of 150 sec.

PfAtg3 immobilization: A CM3 or CM5 surface chip (GE Healthcare) was preconditioned with multiple injections of 20 mM glycine pH 2.2 prior to pH scouting for identification of optimal binding conditions of Atg3 to the sensor chip. MBP-PfAtg3 or

His₆-PfAtg3, dissolved in 10 mM Na Acetate pH 4.0, was immobilized by amine coupling.

Dose-dependent inhibition by fragment: His₆-PfAtg8^{CM} at a constant final concentration of 250 nM was injected in the presence of a 2-fold dilution series of fragments starting at 1 mM, with eight concentrations over His₆-PfAtg3 CM3 chip. RB1 contained 3% DMSO and no BSA. Injections of His₆-PfAtg8^{CM} without fragment were interspersed to control for loss of protein activity over time. Each concentration was run in triplicate at 50 μ L/min with 30 μ L injections and a 40 sec dissociation time starting with the lowest fragment concentration.

Competition screen with VLS compounds: 25 μ L of 150 nM His₆-PfAtg8^{CM}, with either 500 μ M compound or equivalent DMSO (0.5% v/v) in RB2 was injected over His₆-PfAtg3 CM3 chip at 40 μ L/min. ***IC₅₀ determination for C25:*** 40 μ L of 200 nM His₆-PfAtg8^{CM}, diluted in RB2 (0.2% DMSO), was injected over a MBP-tev-PfAtg3-immobilized CM5 chip in the presence of increasing amount of C25 (7 2-fold dilutions, done in triplicate, highest compound concentration is 200 μ M). His₆-PfAtg8^{CM} was dissociated from chip between injections using a 15- μ L injection of 1 M MgCl₂.

MMV SPR competition assay: MBP-PfAtg3 was immobilized onto a CM5 chip (GE Healthcare) as described previously with MBP immobilized on reference flowcell(45). Compounds were added to 300 nM His₆-PfAtg8^{CM} in RB2 (containing 3% DMSO) at a final concentration of 5 μ M. 40 μ L were injected, followed by a 12.5 μ L of 2 M MgCl₂ for dissociation. ***Dose-dependent inhibition:*** 30 μ L of PfAtg8^{CM} at 200 nM was injected in the presence of a 2-fold dilution series of compound (highest concentration of 50 μ M) or equivalent volume of DMSO (final DMSO concentration was

1%). Each injection was followed by a 10 μ L injection of 2 M $MgCl_2$. All measurements were conducted in triplicate.

Direct binding of PAH9 to PfAtg8^{CM}: His₁₂-PfAtg8^{CM} was injected over an NTA-chip (GE Healthcare) preconditioned with nickel, leading to capture of 3,000 response units (RUs). Running buffer contained 3% DMSO. A 4 2-fold-dilution series of compounds, highest concentration of 75 μ M, was injected over PfAtg8 variants at 40 μ L/min.

Direct binding of PTA-Biotin to PfAtg8^{CM}: PTA-Biotin was injected over a neutravidin coated SPR chip (GE Healthcare) on one flowcell, with 130 RUs immobilized, while BACH was injected over a reference flowcell (150 RUs immobilized). His₁₂-PfAtg8^{CM} was injected in triplicate in running buffer containing 3% DMSO. Protein was dissociated from the chip after each cycle with 10 μ L injection of 20 mM HEPES pH 7.4, 1% w/v SDS regeneration solution.

Thermal shift assay: Assays were conducted in 1x PBS with 1:1800 final dilution of SYPRO[®] orange dye (Invitrogen). Measurements made in triplicate for each condition. Concentration of His₆-PfAtg8^{CM} in assay was 65 μ M. Fluorescence was measured from 20 °C to 80 °C in a Biorad C1000™ thermal cycler. For MMV screen: 100 μ M PTA compounds or equivalent volume of DMSO was added to His₆-PfAtg8^{CM}. C25 was added at increasing concentrations in triplicate up to 2 mM. Amount of DMSO in all conditions was kept constant.

Docking: Docking was conducted using the OpenEye software package using standard parameters if not specified otherwise (www.eyesopen.com) (168). *VLS:* The OpenEye software program fred_receptor was used to make an unconstrained receptor. A second receptor was created around the A-loop pocket with specific constraints to hydrogen bond with His67. Initial screening was conducted with the constrained receptor. Hits were screened with the unconstrained receptor to verify binding to the A-loop pocket. Omega2 (188, 189) was used to generate 200 conformers for each compound in each library which were docked with FRED (168). Results were visualized using the OpenEye visualization software, VIDA. *MMV docking:* An unconstrained receptor for PfAtg8 was made with make_receptor from OEDocking toolkit covering the whole molecule to detect potential binding pockets on the surface. Three main pockets (W-site, L-site, A-site) were identified with 377, 271, and 513 Å³ volumes, used in first docking studies. A second receptor was generated with specific constraints to the carbonyl of Lys47 as hydrogen bond donor. A maximum of 2000 conformers per compound was prepared with Omega2 (188, 189) and docked onto constrained and unconstrained receptors with FRED (168).

Synthesis of PTA derivatives: *General.* All reagents were obtained from commercial suppliers and used without further purification. Acetonitrile was distilled after drying on CaH₂ then stored over 3 Å molecular sieves. Yields of all reactions refer to the purified products. Dynamic Adsorbents 32 – 63 µm silica gel was used for flash column chromatography and 250 µm w/h F254 plates were used for thin layer chromatography (TLC). Microwave-assisted reactions were carried out using a Biotage Initiator Microwave Synthesizer (300 W). ¹H and ¹³C NMR spectra were acquired on a Bruker

Avance III 500 spectrometer operating at 500 MHz for ^1H and 125 MHz for ^{13}C . Chemical shift values are reported as δ (ppm) relative to CHCl_3 at δ 7.27 ppm and DMSO at δ 2.50 ppm for ^1H NMR and CHCl_3 at δ 77.0 ppm and DMSO at δ 39.51 ppm for ^{13}C NMR. Mass spectrometry analysis was carried out at University of Illinois at Urbana-Champaign, School of Chemical Sciences, Mass Spectrometry Laboratory. The purity of synthesized compounds was $\geq 95\%$ as analyzed by HPLC (Beckman Gold Nouveau System Gold) on a C_{18} column (Grace Alltima 3 μm C_{18} analytical Rocket[®] column, 53 mm \times 7 mm) using 50 mM triethylammonium acetate buffer, pH 7, and acetonitrile (ACN) as eluent, flow rate of 3.0 mL/min, detection at 300 nm.

4-formyl-N-[4-(pyridin-2-yl)-1,3-thiazol-2-yl]benzamide (PTA-AL). Synthesis conducted by Dr. C. Myer's lab. To a solution of 4-(pyridin-2-yl)-1,3-thiazol-2-amine (0.059 g, 0.33 mmol) in 2.0 mL ACN, the following was added sequentially: 76 mg dicyclohexylcarbodiimide (370 μmol), 50 μg 4-formylbenzoic acid (330 μmol), and 12 mg N,N-dimethylamino pyridine (100 μmol). The mixture was heated at 50°C for 17 hrs, then allowed to cool to RT. Solids were removed by vacuum filtration, and the resulting filtrate was condensed under reduced pressure. The resulting yellow solid was re-dissolved in 5.0 mL CHCl_3 and 5.0 mL 1M HCl was added to give a yellow-tan emulsion at the liquid-liquid interface. This solid was collected by centrifugation at 4,000 rpm for 5 min followed by manual collection of the resulting cake (this acid precipitation was necessary to remove closely eluting impurities). The solid was then purified by silica flash column chromatography (DCM:MeOH:Triethylamine 94:5:1) $R_f=0.32$. The product was obtained as a yellow powder (23 mg, 22% yield). ^1H NMR (500 MHz, DMSO- d_6) δ (ppm) = 12.95 (br. s., 1H), 10.13 (s, 1H), 8.63 (d, $J = 3.93$ Hz, 1H), 8.31 (d, $J = 8.17$ Hz,

2H), 8.07 (d, $J = 8.33$ Hz, 2H), 8.03 (d, $J = 7.86$ Hz, 1H), 7.92 (s, 1H) 7.91 (td, $J = 2.00$ Hz, 8.75 Hz, 1H), 7.35 (ddd, $J = 1.10, 4.79, 7.47$ Hz, 1H) ^{13}C NMR (500 MHz, DMSO- d_6) δ (ppm) = 192.90, 164.74, 158.91, 152.03, 149.54, 149.38, 138.50, 137.30, 137.15, 129.41, 128.94, 122.88, 120.06, 112.30. HRMS (ESI) m/z : calc'd 310.0650 (M-H^+); found 310.0651 (M-H^+).

4-(dimethoxymethyl)-N-[4-(pyridin-2-yl)-1,3-thiazol-2-yl]benzamide (PTAD0).

Synthesis conducted by Dr. C. Myer's lab. PTA-AL dissolved in CHCl_3 was treated with 1M HCl as described above to form the hydrochloride salt. 40 μg of PTA-AL HCl (120 μmol) was suspended in 500 μL MeOH and 10 μL trimethylorthoformate (910 μmol) was added followed by *p*-toluene sulfonic acid monohydrate (3 mg, 12 μmol). This solution was heated by microwave irradiation at 130°C in a sealed vial for 5 min and stirred at RT 36 hrs, at which time a precipitate formed. The solvent was removed under reduced pressure and the residue was dissolved in 10 mL DCM and washed with saturated 10 mL NaHCO_3 brine, and dried with Na_2SO_4 . Condensation under reduced pressure yielded the product as a yellow powder (26 mg, 61% yield). ^1H NMR (500 MHz, CDCl_3) δ (ppm) = 9.81 (br. s., 1H), 8.64 (d, $J = 4.24$ Hz, 1H), 7.96 (d, $J = 8.17$ Hz, 2H), 7.91 (d, $J = 7.86$ Hz, 1H), 7.74 (s, 1H), 7.74 (td, $J = 1.73, 7.70$ Hz, 1H), 7.62 (d, $J = 8.17$ Hz, 2H), 7.22 (dd, $J = 4.95, 6.84$ Hz, 1H), 5.47 (s, 1H), 3.35 (s, 6H) ^{13}C NMR (500MHz, CDCl_3) δ (ppm) = 164.24, 158.12, 152.24, 149.85, 149.62, 143.32, 136.84, 131.80, 127.51, 127.29, 122.69, 120.50, 112.21, 102.08, 52.71. HRMS (ESI) m/z : calc'd 356.1069 (M-H^+); found 356.1070 (M-H^+).

4-[[2-[6-[5-[(3aR,4R,6aS)-2-oxo-1,3,3a,4,6,6a-hexahydrothieno[3,4-d]imidazol-4-yl]pentanoylamino]hexanoyl]hydrazinyl]methyl]-N-(4-pyridin-2-yl-1,3-thiazol-2-

yl)benzamide (PTA-Biotin). Synthesis conducted by Dr. C. Myer's lab. 25 μ L 50 mM PTA-AL dissolved in DMSO was incubated with 20 μ L 50 mM BACH (5-[(3a*S*,4*S*,6a*R*)-2-oxo-1,3,3a,4,6,6a-hexahydrothieno[3,4-*d*]imidazol-4-yl]-N-(6-hydrazinyl-6-oxohexyl)pentanamide) (Sigma-Aldrich) dissolved in DMSO and 10 μ L sodium acetate (pH 4.5) with 0.02% sodium azide at 37 °C O/N. Final concentration of PTA-Biotin was 18 mM.

***P. falciparum* blood stage culturing:** *P. falciparum* 3D7 and FCR3 cultures were maintained using modified, previously published methods at 37 °C, 2% hematocrit of human red blood cells (190). Complete culture media consisted of sterile RPMI 1640 media (Life Technologies), supplemented with 10% human serum, 0.005% hypoxanthine, and buffered with final concentrations of 0.6% (w/v) HEPES and 0.26% (v/v) NaHCO₃. The FCR3 strain was maintained at 3% CO₂ and 5% O₂, 92% N₂ atmosphere, while the 3D7 strain was maintained at 5% CO₂, 5% O₂, 90% N₂ atmosphere.

Immunoblot analysis of *P. falciparum* blood stage: *P. falciparum* FCR3 (generously provided by Dr. J. Smith, Seattle BioMed) asynchronous culture, 25% parasitemia, was washed in starvation media lacking human serum and resuspended in complete media with 50 μ M PAH9, 100 μ M C25 or equivalent DMSO, or starvation media with equivalent DMSO for five hours. RBCs were harvested with centrifugation and lysed with 0.2% saponin. Parasites were harvested by centrifugation and washed in 1x PBS with Complete EDTA-free protease inhibitors (Roche) and lysed by repeated vortexing

and boiling in SDS reducing sample buffer. Lysates were separated with SDS-PAGE on a 15% polyacrylamide gel and subjected to western blotting with 1:400 α -TgAtg8 (generously provided by Dr. P. Roepe, Georgetown University) and 1:1000 α -PfHsp70 (generously provided by Dr. N. Kumar, Tulane University). HRP-conjugated secondary antibodies (Southern Biotech) were detected by SuperSignal West Femto (Thermo Scientific) or Amersham™ ECL™ Prime (GE Healthcare) chemiluminescent substrate. Total protein levels were visualized with ProAct™ Membrane Stain (Amresco) and quantified with ImageJ.(117)

SYBR Green I growth inhibition assay. 10 μ L of 10x compound diluted in RPMI 1640 media (Gibco) with a constant concentration of 1% DMSO was added to a 96 well plate (Costar). 90 μ L of 1.5% ring stage, synchronized with 5% w/v sorbitol *P. falciparum* 3D7 parasites, 1% hematocrit, in culture media with 10% v/v human serum with 10 μ g/mL gentamycin. Each compound concentration and 1% v/v DMSO controls were run in triplicate. Plates were incubated at 37°C in 5% O₂, 5% CO₂ and 90% N₂ for 72 hrs. Plates were frozen, thawed, and incubated with 100 μ L 2xSYBR green in lysis buffer (20 mM Tris pH 7.5, 5 mM EDTA, 0.008% Saponin, 0.08% TritonX-100) in the dark for at least one hour. Fluorescence was measured with a plate reader (HTS 7000, Perkin Elmer) at excitation/emission wavelengths of 485/535 nm.

***In vitro* infection of human hepatocytes with *P. falciparum* 3D7-GFP:** HC-04 cells (ATCC, Manassas, VA, USA) were maintained in complete medium (IMDM) containing 2.5% FCS, 100 units/ml penicillin, 100 μ g/ml streptomycin and 2 mM L-glutamine,

(GIBCO®, Life Technologies). *P. falciparum* 3D7-GFP parasite strain (178) was propagated in the Parasitology Core facility, Johns Hopkins Malaria Research Institute. *In vitro* infection of human hepatocytes was done as described previously (175). Briefly, salivary glands were dissected from infected *Anopheles gambiae* mosquitoes 17 days after exposure to infective blood meal. Sporozoites were isolated with an OptiPrep™ Density Gradient (Sigma-Aldrich) at 12,000 x g for 10 min, washed in complete medium and counted with a hemocytometer. Sporozoites were incubated with HC-04 cells at 3:1 sporozoite to hepatocyte ratio for 2 hrs at 37°C. Cells were incubated with DMSO, 3 µM or 30 µM of PAH9 or C25 in complete media, replenishing media and compound after 48 hrs. Flow cytometry based detection of infected cells was done 72 hrs post infection using FACSCalibur flow cytometer (BD Biosciences) and analyzed using FlowJo software (Tree Star, Inc.).

HC-04 cell viability under 3 µM and 30 µM C25 and PAH9, or equivalent DMSO in complete media was assessed after 96 hrs. Annexin-V positive and PI-positive cells in hepatocyte cultures were detected by flow cytometry according to the manufacturer's instruction (Invitrogen™, Life Technologies).

Nuclear Magnetic resonance: His₆-PfAtg8^{CM} BL21-RII cells were grown O/N as normal and expanded to 2 L in TB. At an OD₆₀₀ of 2.2, cells were harvested at 3000 x g, 4°C, 20 min and the cell pellet was washed with chilled 1xM9 salt solution (3 g/L KH₂PO₄, 6.8 g/L Na₂HPO₄, 5g/L NaCl, pH 7.2) and centrifuge. The cell pellet was resuspended in isotopically-labelled minimal media (1xM9 salt solution, 1 g/L ¹⁵NH₄Cl, 6g/L Dextrose, 10 mg/L thiamine, 2 mM MgSO₄, 0.1 mM CaCl₂), grown for one hour,

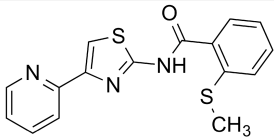
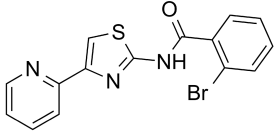
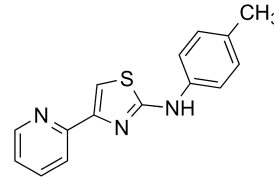
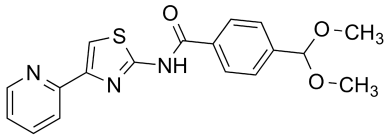
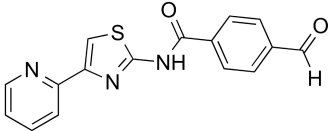
induced with 0.5 mM IPTG, and grown O/N, 20°C. Harvesting and purification with affinity tag, cation exchange, and size exclusion was performed the same as for unlabeled His₆-PfAtg8^{CM} with final buffer 25 mM MES, 5% glycerol, 0.5 mM MgCl₂, pH 6.5. Data was acquired at 25°C on an 800 MHz (¹H) Varian Inova spectrometer at the JHU Biomolecular NMR Center.

Tables

Table 3.1. Virtual library screening compounds

ID	Name	CID	Mol wt.	Structure
C5	5-nitro-N-(pyridin-3-ylmethyl)furan-2-carboxamide	693996	247.20	
C6	N-[(8-hydroxyquinolin-7-yl)-phenylmethyl]benzamide	2871881	354.40	
C11	N-[(7-pyridin-4-yl-2,3-dihydro-1-benzofuran-2-yl)methyl]-4,5,6,7-tetrahydro-1-benzothiophene-3-carboxamide	45176114	390.49	
C13	1-(4-bromophenyl)sulfonyl-N-(furan-2-ylmethyl)piperidine-4-carboxamide	1327632	427.31	
C16	N-[(1-ethylpyrazol-4-yl)methyl]-5-phenyl-1H-pyrrole-2-carboxamide	56751948	294.35	
C17	N'-(6-ethyl-1-methylpyrazolo[3,4-d]pyrimidin-4-yl)-N-pyridin-3-ylethane-1,2-diamine	56894679	297.35	
C18	N-[2-[methyl(methylsulfonyl)amino]ethyl]-5-phenyl-1H-pyrrole-2-carboxamide	56745406	321.39	
C19	3-ethyl-N-[(2-pyrazin-2-yl-1,3-thiazol-4-yl)methyl]-1H-indole-2-carboxamide	50956056	363.43	
C20	5-(2-chlorophenyl)-2-methyl-N-[(4-oxo-1H-pyrimidin-6-yl)methyl]furan-3-carboxamide	50965334	343.76	
C22	2-ethyl-4-methyl-N-[(2-pyrimidin-2-yl-1,3-thiazol-4-yl)methyl]-1,3-thiazole-5-carboxamide	50974374	345.44	
C24	N-[[1-(1H-imidazol-5-ylmethyl)pyrrolidin-3-yl]methyl]-8-methylimidazo[1,2-a]pyridine-2-carboxamide	56723508	338.40	
C25	1-[(3-methylphenyl)methyl]-3-[[1-(pyridin-2-ylmethyl)pyrrolidin-3-yl]methyl]urea	56750287	338.44	
C28	N-[[2-(dimethylamino)pyridin-3-yl]methyl]-4-phenyl-1H-imidazole-5-carboxamide	56749897	321.37	
C29	5-(1-cyclopentylpyrrolidin-2-yl)-N-[(6-methyl-4-oxo-1H-pyrimidin-2-yl)methyl]thiophene-2-carboxamide	45200702	386.51	
C30	N-[(2-pyrazin-2-yl-1,3-thiazol-4-yl)methyl]-4H-thieno[3,2-b]pyrrole-5-carboxamide	50952642	341.41	

Table 3.2. Structures and inhibition data for PTA compounds^a

Compound	CID [MMV ID]	Structure	Mol wt.	IC ₅₀ (μM) (LEAN)	
				SPR	Blood stage
PAC5	2526359 [MMV001246]		327.42	14.95 (0.22)	0.20* (0.30)
PBB8	2454286 [MMV665909]		360.23	6.03 (0.25)	1.58* (0.35)
PAH9	746602 [MMV007907]		267.34	18.16 (0.25)	1.47 (0.31)
PTA-D0	N/A		355.41	2.86 (0.22)	1.48 (0.23)
PTA-AL	N/A		309.34	Not tested	

^aPTA-containing compounds used in studies listed with PubChem Compound Identification (CID), MMV ID, chemical structure, molecular weight (g/mol), IC₅₀ in SPR and blood stage assays, and LEAN score, calculated as $-\log(\text{IC}_{50})/\text{number of heavy atoms}$. Asterisks denote IC₅₀ values derived from the literature.

Figures

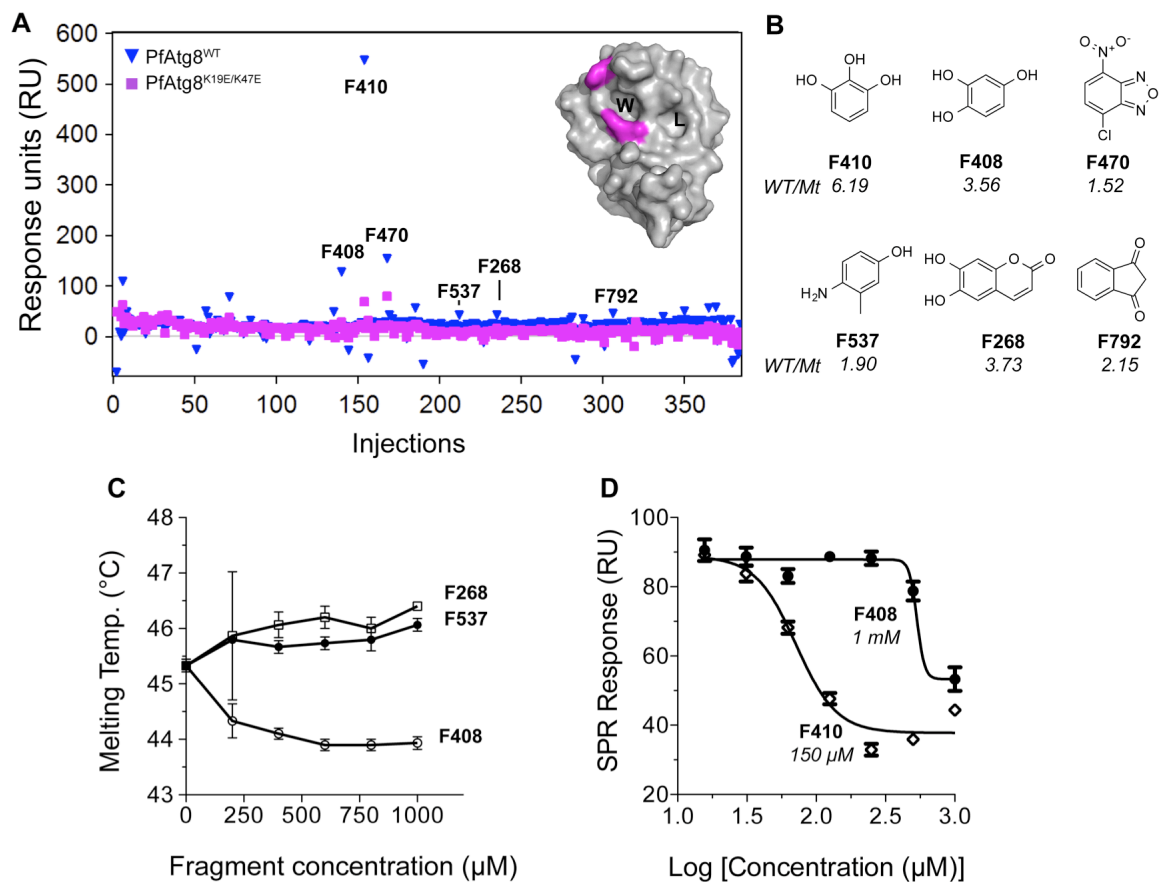


Figure 3.1. Identification of molecular fragments that inhibit PfAtg8-PfAtg3 interaction. **A.** Zenobia fragments were screened for binding to the W-site of PfAtg8 using SPR. PfAtg8 WT and K19E/K47E W-site mutant were immobilized and fragments were injected. **B.** Chemical structure of fragments hits giving 1.5x response over noise for WT and at least 1.5x's normalized response for WT over K19E/K47E (Mt). **C.** TSA of SPR hits with His₆-PfAtg8^{CM}. The melting temperature of His₆-PfAtg8^{CM} was measured with increasing concentration of fragments. **D.** SPR-based inhibition assay. His₆-PfAtg8^{CM} was injected over the MBP-PfAtg3-conjugated chip with increasing concentrations of fragment. Solid line indicates mean response with no fragment for reference. Approximate IC₅₀ values shown in italic.

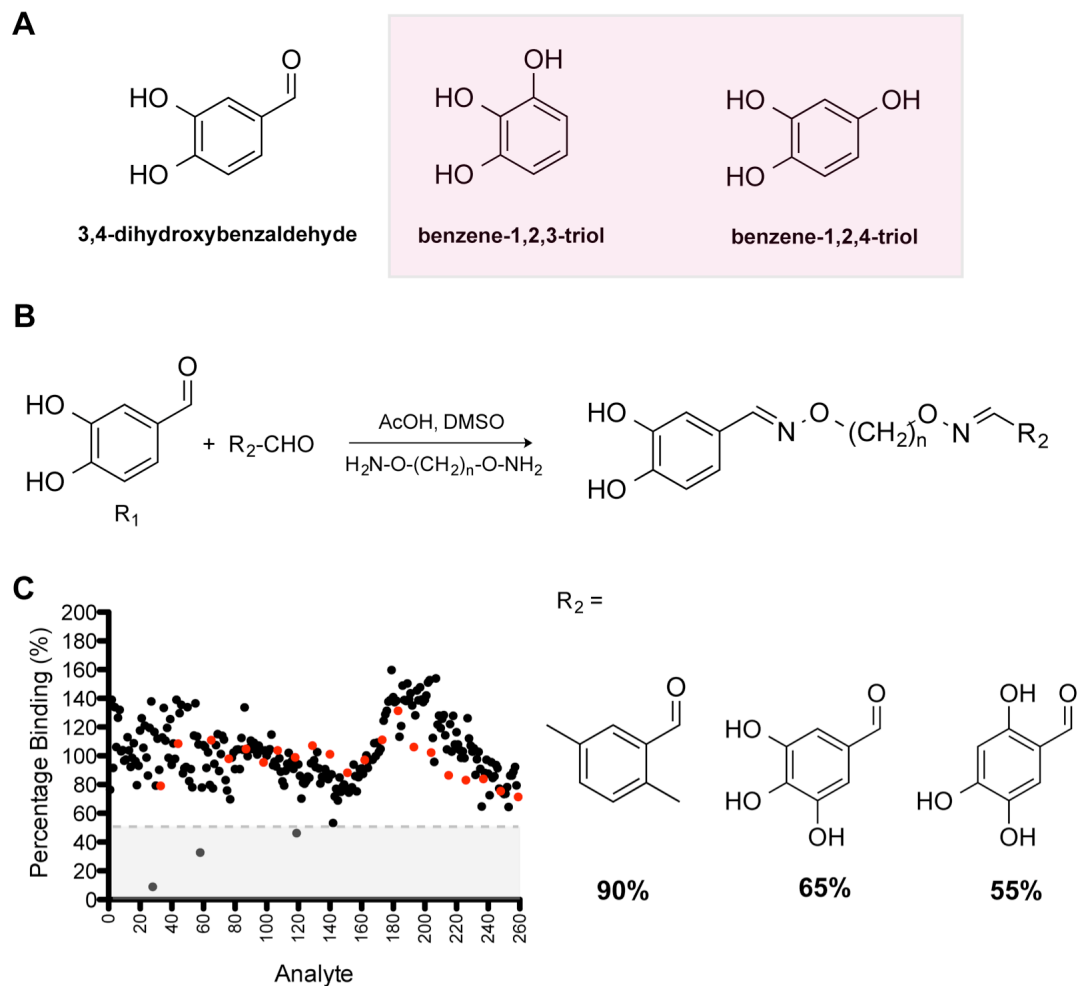


Figure 3.2. Screening of hydroxybenzene oxime library. **A.** Comparison of oxime library R_1 group to fragment hits (in pink box) identified against PfAtg8. **B.** Reaction scheme for synthesis of hydroxybenzene oxime library. 240 different aldehydes were screened. Red dots denote injections of PfAtg8 with DMSO for baseline binding. **C.** Oxime library was screened using the PfAtg8-PfAtg3 competition assay with SPR at 20 μM . The R_2 groups of hits, leading to 50% inhibition or greater, are shown at right.

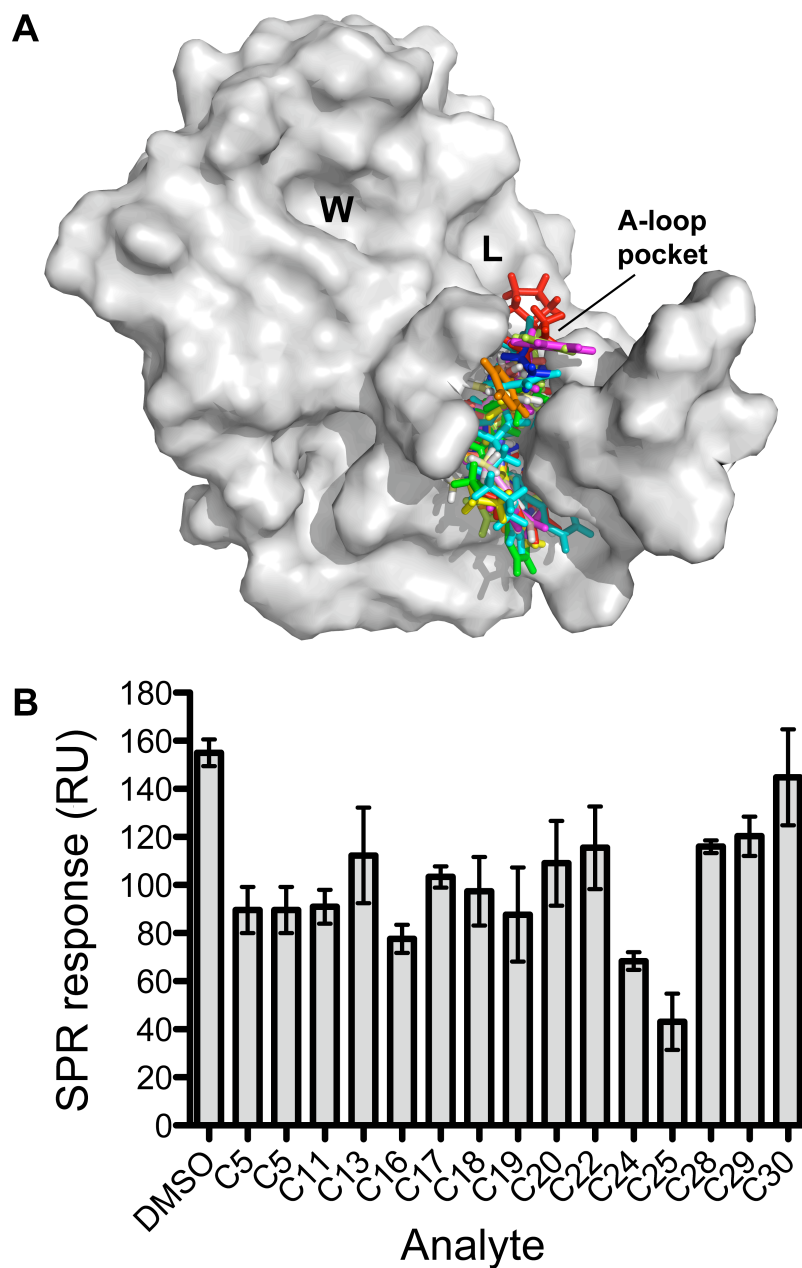


Figure 3.3. Virtual library screening for A-loop pocket binders. **A.** VLS compounds docked onto the structure of PfAtg8. **B.** *In vitro* screening of VLS compounds. PfAtg8 was injected over an SPR chip immobilized with PfAtg3 in the presence of DMSO or 15 VLS compounds. Bars represent mean and SD for triplicate measurement.

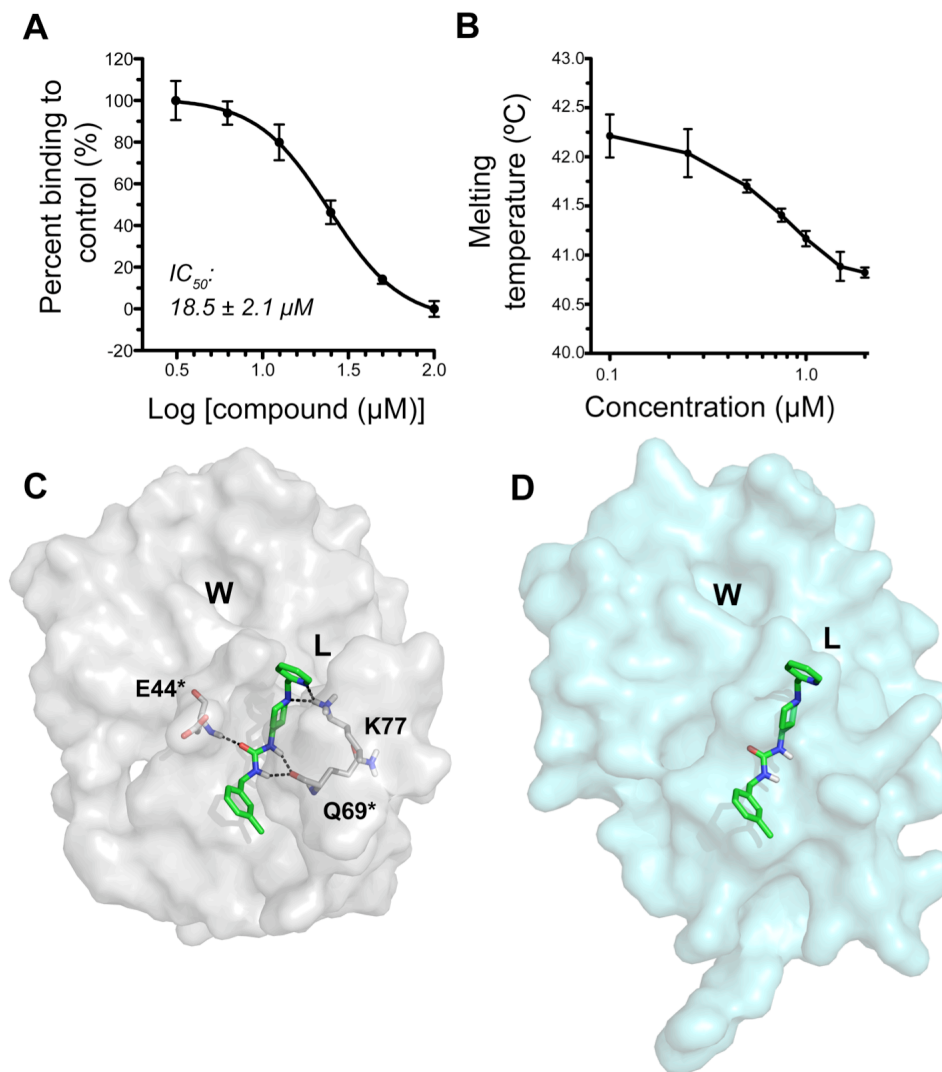


Figure 3.4. Dose-dependent inhibition with VLS compound, C25. **A.** Dose-dependent inhibition by C25. Curve is representative of two independent experiments with an average IC_{50} of $18.5 \pm 2.1 \mu M$. **B.** Docking of C25 to PfAtg8 (PDB code 4EOY). Hydrogen bond contacts between PfAtg8 residues and C25 are shown. Asterisk denotes contact to main chain nitrogen or oxygen. **C.** Human Atg8 homologue, GATE-16 (PDB code 1EO6) was superposed onto PfAtg8 to illustrate the absence of A-loop pocket in human homologues.

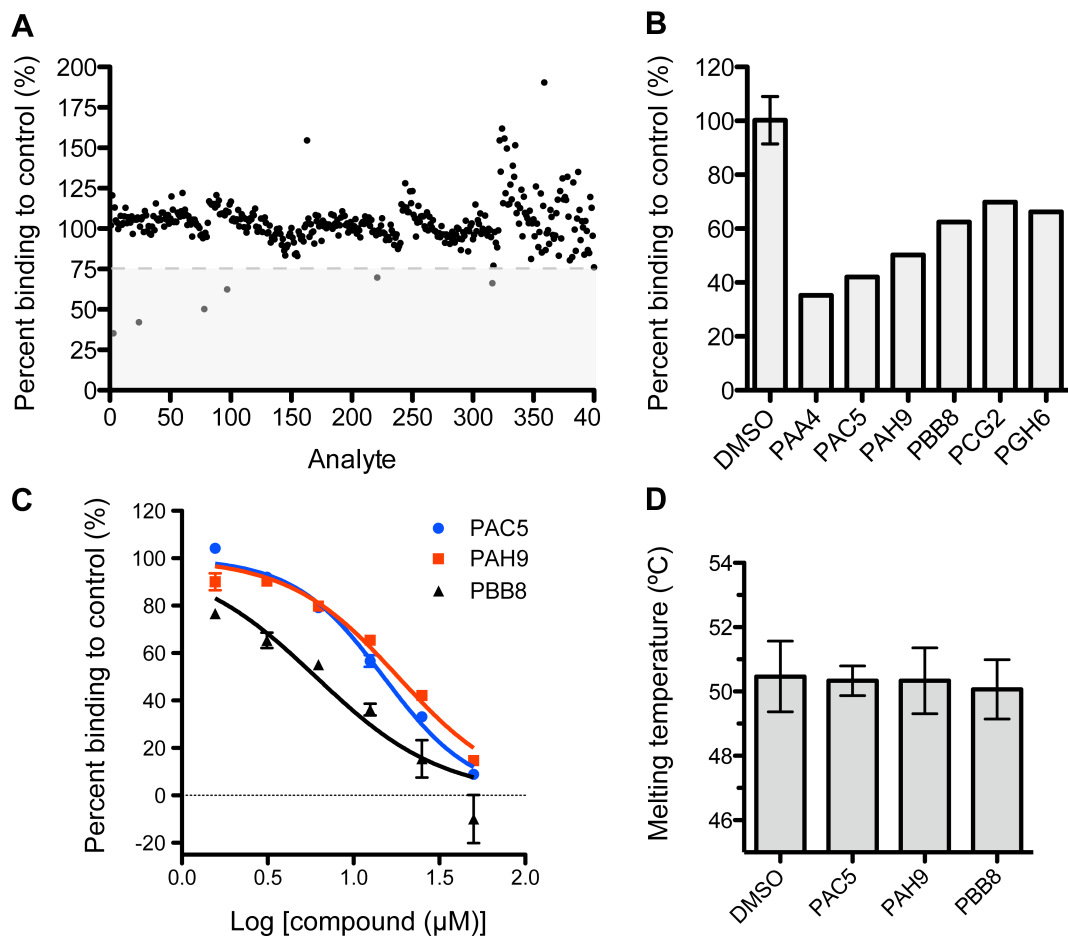


Figure 3.5. Identification of a common scaffold that inhibits Atg8-Atg3 from the MMV malaria box.

A. Primary screen of MMV Malaria Box with SPR competition assay (169). Gray box denotes compounds meeting the threshold of greater than 25% inhibition. **B.** Bar graph showing inhibition of hits in primary screen, denoted by plate position. **C.** Dose-dependent inhibition of PfAtg8-PfAtg3 interaction by MMV compounds. Inhibition was measured with increasing amount of compound in SPR competition screen. Mean and SD of 3 injections are shown. **D.** Thermal stability assay of PfAtg8^{CM} with the three MMV hits. Error bars represent SD of 3 measurements.

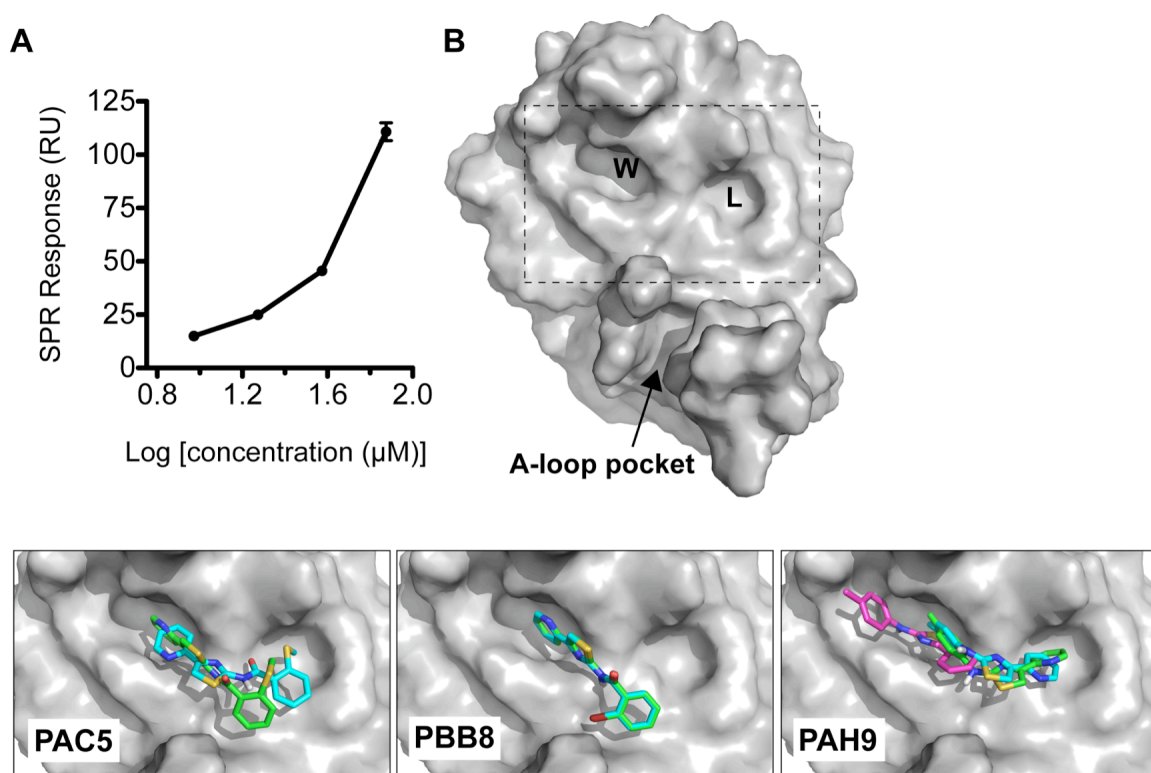


Figure 3.6. *In vitro* and *silico* studies on PfAtg8-PTA compound binding. **A.** Binding of PAH9 to PfAtg8. His₁₂-PfAtg8^{CM} was immobilized onto a nickel-charged NTA SPR chip. PAH9 was injected over variants in two separate runs at 4 concentrations. Graph shows mean \pm SD of binding from PAH9. **B.** *In silico* docking of PTA compounds to PfAtg8^{CM} (PDB code 4EOY). Overall structure of PfAtg8 with W- and L-site and A-loop demarcated. Below: best poses for each compound. The predicted pose for unconstrained docking is shown in cyan. Docking was also performed constraining to the carbonyl of Lys47, located between the W- and L-site. Predicted pose for constrained docking is shown in green. For PAH9, an alternate pose, highly ranked in the unconstrained docking and enriched in top ten poses is shown in magenta.

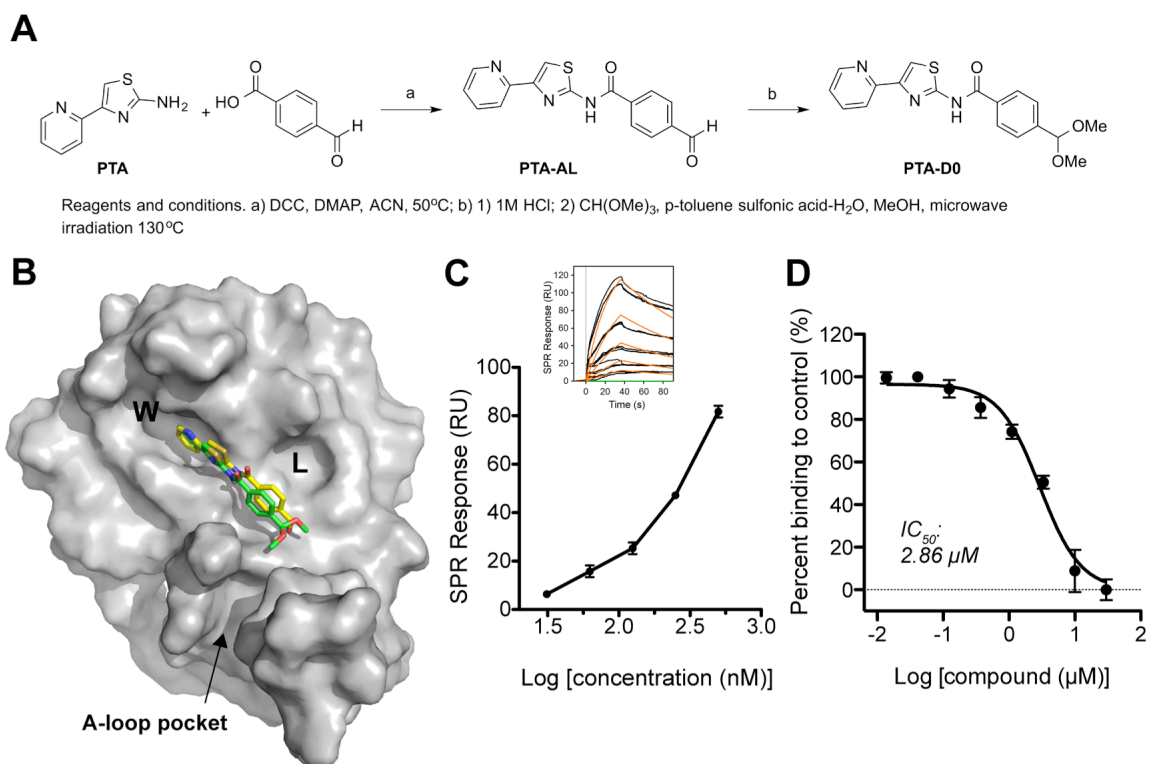
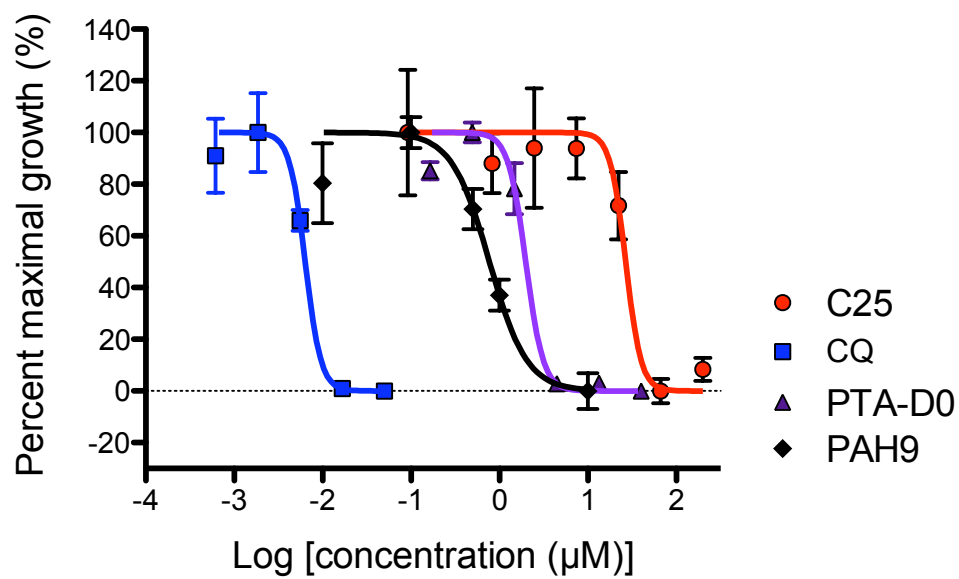


Figure 3.7. Synthesis of a PTA derivative with a functional handle. **A.** Reaction scheme for synthesis of PTA-AL and PTA-D0. **B.** *In silico* docking of PTA-derivatives onto PfAtg8. PTA-AL (yellow) and PTA-D0 (green) were docked onto the constrained receptor of PfAtg8^{CM} (PDB code 4EOY) with OpenEye docking suite (168). **C.** Direct binding of PTA scaffold to PfAtg8. PTA was linked to biotin through a PEG linker and immobilized onto an SPR chip. PfAtg8 was injected, leading to dose-dependent binding (sensorgram shown in inset). **D.** Inhibition of PfAtg8-PfAtg3 interaction by PTA-D0. SPR response of PfAtg8 injected over immobilized PfAtg3 was measured in the presence of increasing concentration of PTA-D0. IC₅₀ was determined as 2.86 μM. Mean ± SD of 3 injections are shown.



Cmpd	IC ₅₀ (μM)			Mean (μM) ± SD
	1	2	3	
CQ	0.005	0.007	0.002	0.003 ± 0.002
PAH9	0.768	3.312	0.769	1.61 ± 1.47
PTA-D0	-	1.050	1.900	1.47 ± 0.60
C25	26.74	13.42	16.75	18.97 ± 6.92

Figure 3.8. Inhibition of *P. falciparum* blood stages. SYBR green I assays were used to measure inhibition of parasite growth by CQ, PAH9, C25, and PTA-D0. Growth inhibition curves are shown for one experiment, with SD. IC₅₀ values from two to three experiments are shown in table inset.

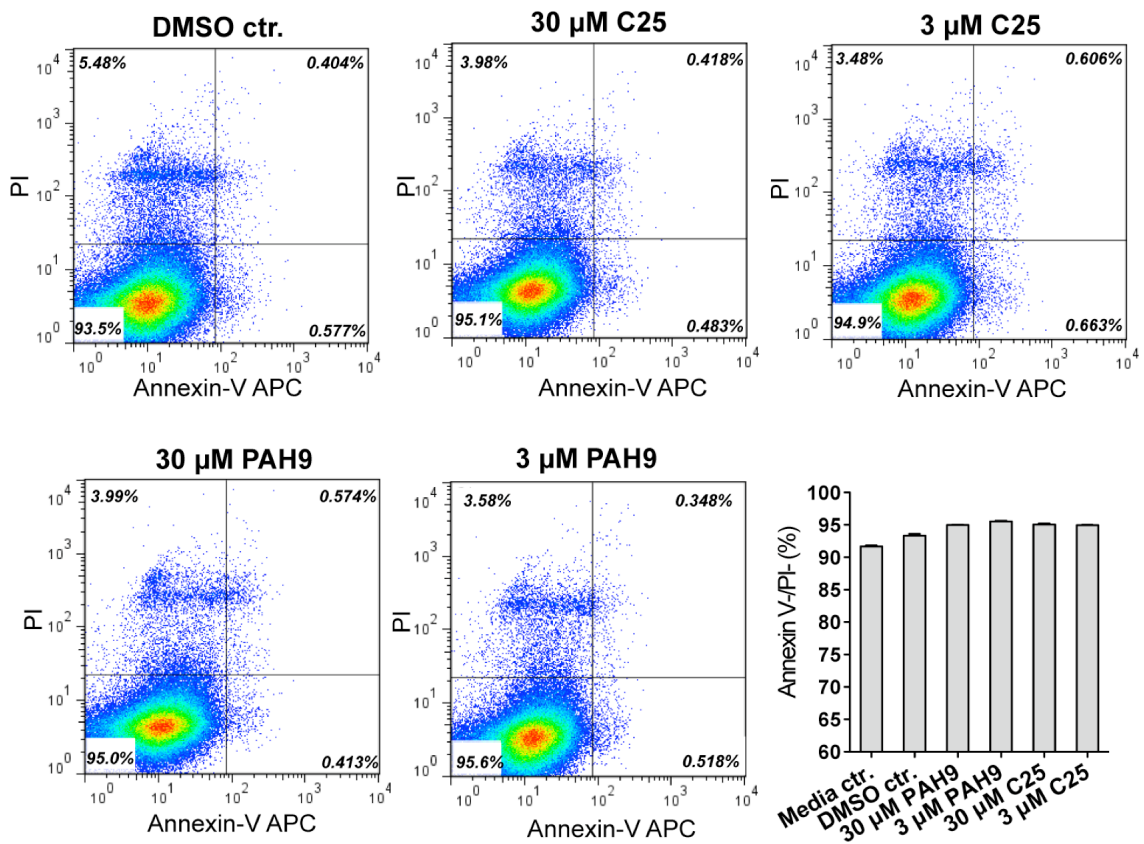


Figure 3.9. Effect of PAH9 and C25 treatment on viability of human HC-04 cells *in vitro*. Flow cytometry was used to detect Annexin-V and PI positive cells in HC04 hepatocyte cultures treated with C25 and PAH9. Dot plot graphs represent pattern of staining, bar graphs show mean and SD of viable cells in three independent cell cultures.

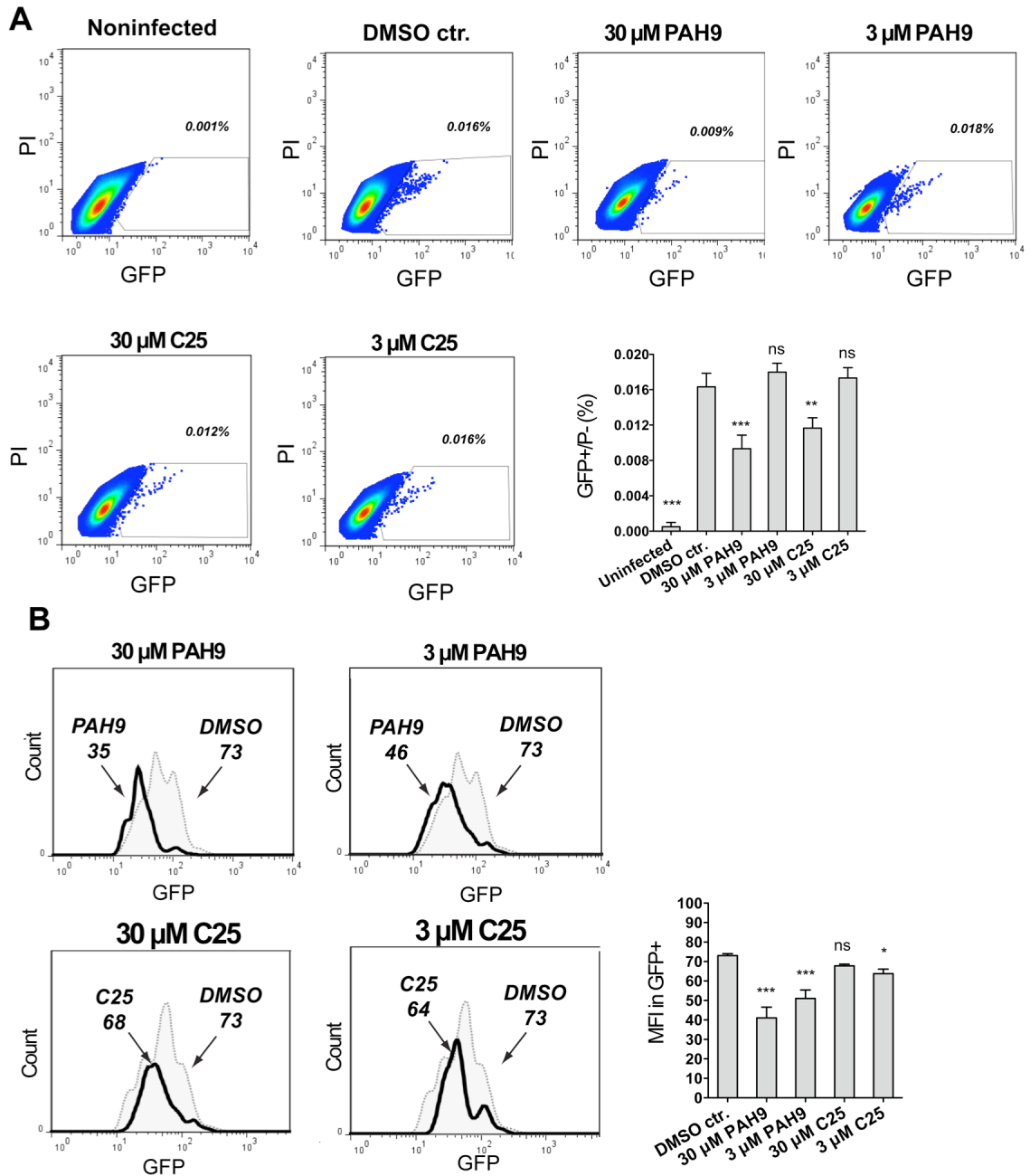


Figure 3.10. Effect of PAH9 and C25 treatment on the development of *P. falciparum* 3D7 GFP parasite in HC-04 cells *in vitro*. **A.** Viable, *P. falciparum*-infected hepatocytes (GFP+/PI-) exposed to drug treatment were detected by flow cytometry 72 hrs post-infection. Dot plot is representative of pattern of staining. Numbers indicate percentage of GFP+ cells in PI- cell population. Bar graph shows mean and SD of three independent cultures. **B.** GFP fluorescence intensity of *P. falciparum*-infected hepatocytes exposed to drug treatment was assessed with flow cytometry. Histograms demonstrate one representative

staining pattern, numbers indicate mean fluorescence intensity (MFI) of GFP+/PI- populations. Bar graph shows MFI of GFP mean and SD in three independent cultures.

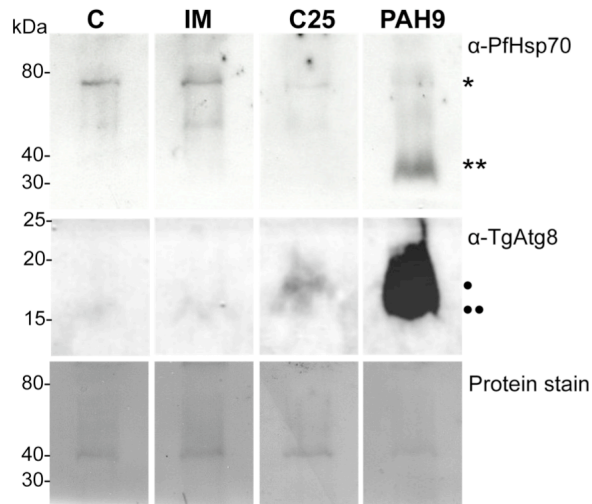


Figure 3.11. PAH9 and C25 increase PfAtg8 protein levels. *P. falciparum* FCR3 was treated with DMSO (C), starved with incomplete media (IM), or C25 or PAH9 for five hours. Parasite lysate was separated with SDS-PAGE and PfAtg8 and PfHsp70 detected with Western Blot. Asterisk denotes expected molecular weight of Hsp70. Double asterisk denotes smaller band detected in PAH9 sample with mobility ~ 35 kDa. Double dot indicates mobility of control and starved sample, potentially the PE-lipidated form of Atg8, which runs with faster mobility. Single dot indicates slower mobility of C25 and PAH9 treated samples, possibly representing the unlipidated form of Atg8. Below is membrane stained with Ponceau S protein stain as loading control.

Chapter 4

Preliminary studies into Atg8 functions in *Plasmodium*

Abstract

Interest in autophagy has surged in the past five years and is now seen as a therapeutic target in many diseases including cancer, neurodegeneration, and infectious diseases. While much was known about the role of autophagy in the protozoans *Leishmania*, *Trypanosoma*, and *Toxoplasma*, the story is less conclusive for the malaria parasite *Plasmodium*. Atg8 is essential in *Plasmodium* but it is not known if a classical autophagy pathway exists. Suggested variations on traditional autophagy include roles in hemoglobin transportation, drug detoxification, and protein and organelle export to the parasitophorous vacuole and possibly beyond.

Atg8 homologues in other species are involved in diverse processes including trafficking within the Golgi apparatus, regulation of fibronectin translation, and interaction with lipid rafts to mediate apoptosis. We undertook an unbiased mass spectrometry approach to identify PfAtg8-binding proteins in the red blood cell stage of infection. Many exported proteins were identified, leading us to examine localization of PfAtg8 with exported proteins using immunofluorescence assays. Our studies suggest Atg8 is involved in trafficking proteins to the PV and host cytoplasm under basal conditions in the red blood cell. However these studies are preliminary and much work remains to be done on this possibly extremely important role.

Introduction

As described in detail in Chapter 1, the function of Atg8 in *Plasmodium* is unclear and it is still under dispute if there is a bona fide autophagic pathway in *Plasmodium*. Strictly speaking, confirmation of macroautophagy in *Plasmodium* would require the presence of Atg8-labelled double-membrane vesicles, fusion of these vesicles with a lysosomal-like compartment, and breakdown and recycling of the autophagosome cargo. The strongest evidence is the recent report of Atg8 on double-membrane vesicles near and inside the acidic food vacuole upon starvation (66).

The unique biology of the parasite as well as the adaptability of the machinery in other organisms for non-autophagic purposes (191) makes alternative roles quite feasible and even likely. Kitmura et al. first described co-localization of PfAtg8 with the apicoplast markers histone-like protein, heat unstable (HU) and apicoplast localizing protein, (ACP) suggesting a hitherto unpredicted function distinct from autophagy (192). This co-localization does not appear to be complete, however (64, 66), and changes upon starvation or CQ treatment (66, 67). There is much work to be done determining the role of PfAtg8 in *Plasmodium*. This is complicated by the inability to knockout *Plasmodium* Atg8 and the difficulty in making conditional knockouts. PfAtg8 is lipidated (39) and the C-terminal glycine for lipidation is required for PfAtg8 localization (66). Therefore the Atg8 conjugation machine, including interaction with its conjugating enzyme, Atg3 is required for PfAtg8 localization and function. We attempted to use our Atg8 inhibitors, described in Chapter 3, as molecular probes to explore functions of PfAtg8 in the blood

stage. Together with results from our mass spectrometry-based PfAtg8 interactome study, we suggest a role for PfAtg8 in trafficking proteins to the host.

Results

Identification of PfAtg8 interactors

Atg8 homologues bind diverse proteins in other species to accomplish homologue-unique functions. We sought to identify PfAtg8 interacting proteins in order to gain insight into its function(s). PfAtg8 was immobilized via its hexahistidine tag and incubated with blood stage *P. falciparum* 3D7 protein lysate along with controls of either Ni-NTA resin or the unrelated *Plasmodium* proteins, PfGAP50 (PF3D7_0918000) and PfMTIPΔ60 (PF3D7_1246400) (193, 194). After extensive washing, His₆-PfAtg8 and bound proteins were eluted and separated with SDS-PAGE (Figure 4.1A). Bands were cut out of Atg8 and control samples and analyzed with tandem mass spectrometry (MS/MS) (Figure 4.1B) by Dr. D. Colquhoun in the Graham laboratory (Johns Hopkins University, USA). In all replicates, peptides corresponding to endogenous PfAtg3, a known PfAtg8 interactor (Chapter 2, Figure 2.2), were identified in the PfAtg8 sample (Figure 4.1). In a reciprocal pulldown experiment, we immobilized PfAtg3 and incubated with parasite lysate. 13 unique peptides corresponding to Atg8 were identified with 78% coverage.

We segmented identified proteins from three PfAtg8 pulldown experiments into tiers according to their specificity for Atg8 and their repeated identification. Proteins identified in more than one replicate and in none of the controls were considered the strongest candidates in Tier 1A. Proteins appearing twice in the Atg8-immobilized sample and in one of the controls were considered Tier 1B. Proteins identified in the Atg8-immobilized sample in one experiment and in none of the controls were classified

as Tier 2. Tier 3 proteins were identified in one of the Atg8 samples with 100% probability and less than 30% probability in the controls (Table 4.1). Other proteins identified by MS/MS but not meeting these criteria are shown in Table A.4.

Four proteins were classified as tier 1A. Two of the four candidates, falcilysin (PF3D7_1360800) and m1-aminopeptidase (PF3D7_1472400), are located in the food vacuole and associated with hemoglobin degradation (195-198). Seven proteins were classified as tier 1B. Many chaperone proteins were present, including TCP-1 family proteins, 14-3-3I, and heat shock-family proteins. Chaperones were also present in the nonhits list, but not to the same extent (Table A.4). Ribosomal proteins and tRNA-binding proteins were enriched in the Atg8 sample and were also prevalent in the non-hits list.

Figure 4.2 depicts the cellular location of candidates while figure 4.3 shows the biological processes represented and known interactions within them. A range of biological processes is represented, but protein translation and protein folding/trafficking are enriched. Hits were additionally arranged according to sub-cellular location, as indicated by the literature. Exported proteins, present at the parasite membrane, parasitophorous vacuole, trafficking organelle Maurer's clefts (MC), and parasite membrane, are enriched. Among the exported proteins identified, the major virulence factor, PfEMP1 was identified in two independent experiments. PfEMP1 is exported to parasite-derived knob structures on the RBC surface. Though normally exported, these proteins were likely interacting with Atg8 within the parasite PM membranes, as infected red blood cells were saponin-treated to lyse the RBC (and PVM) membranes and washed with RPMI and PBS to remove erythrocytic cytoplasmic proteins.

Localization of endogenous PfAtg8 in blood stage

Because PfEMP1 was identified as a possible interacting partner in our mass spectrometry studies, we were interested to test if a pool of Atg8 co-localizes with PfEMP1 either inside the parasite or in the RBC cytoplasm. PfEMP1 is encoded by the multiplicity *var* gene family with ~60 variants, switching its expression regularly to evade host immunity (98, 199). Immuno-based studies against PfEMP1 are therefore difficult. However, only one Var member binds the placental receptor chondroitin sulfate A (CSA) (200, 201). By selecting for infected red blood cells (RBCs) that bind CSA, a parasite population is isolated that predominantly expresses Var2csa. *P. falciparum* FCR3-CSA parasites, kindly provided by Dr. J. Smith at Seattle BioMed, were exploited to examine localization of PfAtg8 and PfEMP1.

Because PfAtg8 was shown by several groups to localize to the apicoplast in blood and liver stages (38, 39, 66, 202), we first examined whether this was the case in our *P. falciparum* FCR3 CSA-selected strain. Using IFA, we observed co-localization between PfAtg8 and the apicoplast marker, ACP, throughout the blood stage (Figure 4.4).

Interestingly, when IFAs were conducted with parasites at a much higher parasitemia (26% rather than 5%) PfAtg8 did not co-localize with ACP and PfAtg8 was enriched at the parasite plasma membrane throughout the blood stage (Figure A.6). High parasitemia likely decreases the available nutrients compared to lower parasitemia culture conditions. Starvation has previously been shown to lead to re-localization of PfAtg8, to the RBC cytoplasm in one study (67) and to Rab7 vesicles and the food vacuole in another (66).

We next tested whether PfAtg8 co-localized with PfEMP1 Var2csa under normal conditions. Although PfEMP1 could be detected outside the parasite, the signal was much higher within the parasite in our assays. Within, the parasite, PfAtg8 partially co-localized with PfEMP1 (Figure 4.5). PfEMP1 is trafficked to the RBC membrane via the Maurer's cleft and skeleton binding protein-1 (SBP1) a MC-localized protein, is required for PfEMP1 transport to the RBC surface (203, 204). We therefore sought to determine if PfAtg8 and PfSBP-1 (antibody kindly provided by Dr. C. Breton-Braun, Université Montpellier, France) co-localized under normal culture conditions. Using two different antibodies against either the amino end (BR5) or carboxy end (B28) of SBP1, we observed PfSBP-1 staining in the parasite as well as punctae in the RBC cytosol, consistent with the MC. Co-localization with PfAtg8 was again limited to a large pool of SBP-1 inside the parasite (Figure 4.6). Co-localization with both PfEMP1 and SBP-1 persisted through the trophozoite and schizont blood stages.

Inhibition of PfAtg8 with PAH9 (MMV007907)

Because a pool of PfAtg8 co-localized with the exported protein PfEMP1 and SBP-1, we hypothesized PfAtg8 might be involved in trafficking of PfEMP1. We treated cells with PAH9 for six hours and observed changes to PfAtg8 and PfEMP1 localization with immunofluorescence images. We did not observe any obvious changes to PfAtg8 localization or co-localization with Var2csa at any stage (Figure A.7). However, it is possible that changes were too subtle to observe by eye. As mentioned previously, the signal of PfEMP1 in the RBC cytoplasm and surface was drastically lower compared to within the parasite. This may be an artifact of our fixation or staining procedure as RBC

structure appeared compromised in many cells. Therefore it was impossible to determine with IFA if drug treatment led to a decrease in PfEMP1 staining at the RBC surface. We therefore turned to flow cytometry to quantify PfEMP1 trafficking to the surface.

To quantify the amount of PfEMP1 on the surface of parasites, late rings were treated with PAH9 and PTA-D0 for 17 hrs. Cells were stained with rabbit antiserum immunized against Var2csa or rabbit antiserum as a control. Cells were further stained with secondary antibody, DRAQ5 for sorting of iRBCs, and subjected to flow cytometry. 84% of parasite-infected control cells were PfEMP1 positive (Figure 4.7A). The percentage of parasite-infected cells staining for PfEMP1 on the RBC surface decreased to 67.7% with 3 μ M PAH9 and 46.8% with 30 μ M PAH9 (Figure 4.7B,D). Similarly, 64.2% of cells stained positive for PfEMP1 with 3 μ M PTA-D0, however this decreased marginally with 30 μ M treatment (Figure 4.7C,D). 3 μ M drug treatment had no effect on the number of DRAQ5 positive cells. There was a 42% decrease in DRAQ5-positive cells with 30 μ M PAH9 and 27% reduction with 30 μ M PTA-D0, consistent with PAH9's more potent inhibition in the SYBR green assays in Chapter 3.

Discussion

Our MS/MS interactome study identified candidate PfAtg8-interacting proteins involved in a wide array of biological functions. Two known autophagy proteins were identified, PfAtg3 (PF3D7_0905700.2) and cell division cycle protein 48 (Cdc48) homologue (PF3D7_0619400), an AAA family ATPase necessary for autophagosome biogenesis in yeast and mammals (205, 206). We expected to find more autophagy proteins in our pulldown and were surprised by the absence of the E1-activating enzyme, Atg7, as Atg7 is important for blood stage parasite growth (65).

Represented biological processes:

Protein translation: Many ribosomal subunits and RNA-binding proteins critical for protein translation were identified, representing about 30% of the PfAtg8 hits. It is important to keep in mind that they represented 25% of nonhits. Ribosomal proteins are acidic in nature, while PfAtg8 is basic so these hits could represent nonspecific charge-charge interactions. However the mammalian Atg8 homologue, LC3, regulates protein translation and stability of fibronectin through binding to an AU-rich element in the 3'UTR (207, 208).

Chaperones: Chaperone family proteins constituted 13% of PfAtg8 candidates and 6% of non-hits. Chaperones are thought to play an important role in the *Plasmodium* parasite as it cycles between different temperatures and physiological conditions in the mosquito vector and human host, reviewed in (209). In addition to a cytoprotective role, it has been suggested that the Hsp70 family is involved in protein trafficking and export

(210). PfHsp70-3 (PF3D7_1134000) was a tier1B hit. PfHsp70-3 has been identified in the Maurer's clefts (211, 212) and the parasitophorous vacuole (213). PfHsp70-3 phylogenetically clusters with mitochondrial Hsp70 homologues, which drive translocation of proteins into the mitochondrial matrix (214) but also has high homology to human HspA9 (209), which is implicated in antigen export in humans (215, 216). Additionally, yeast-two hybrid studies with PfHsp70-3 identified many malarial exported proteins (data available on www.plasmodb.org).

In Chapter 3 we described an interesting effect on Hsp70 with drug treatment. Treatment of parasites with high levels of our inhibitor, PAH9, led to what appeared to be a cleavage of Hsp70 as well as accumulation (or induction of synthesis) (Figure 3.11). In mammals Hsp70 and its co-chaperone BAG3 deliver aggregates to p62 bodies, or aggresomes, in chaperone-assisted selective autophagy (CASA) (217). p62 is an autophagic receptor that recruits substrates to the autophagosome through interaction with the Atg8 homologue, LC3. Another chaperone identified in our study, 14-3-3 (PF3D7_0818200) was recently elucidated as a major regulator in CASA through interaction with BAG3 (218).

Protein trafficking: A tier3 candidate, the small GTP-binding protein sar1 (PF3D7_0416800) is a component of the COPII vesicle machinery for trafficking between the ER and Golgi. Sar1 was shown to have similar localization to the ER and small vesicle compartments in *P. falciparum* blood stages as in yeast, at the ER site for secretion of proteins (219, 220). m1-family aminopeptidase (PF3D7_1472400) was identified as a tier1B hit. It is implicated in hemoglobin degradation and has an interesting trafficking route first to the PV and then to food vacuole (197). The human

Atg8 homologues are involved in numerous vesicle trafficking pathways. For example, GATE-16 (Golgi-associated ATPase Enhancer of 16 kDa) is involved in intra-Golgi trafficking (221) and GABA (GABA(A) receptor-associated protein) is involved in GABA_A receptor trafficking in neurons (222). Our study was enriched for proteins that are trafficked outside the parasite plasma membrane (Figure 4.2). Unconventional protein secretion, termed exophagy, utilizes the autophagosomal machinery as well as GRASP65 and the t-SNARE, Sso1, which have putative homologues in *Plasmodium* (223, 224). Exophagy utilizes the COPII machinery but bypasses Golgi processing and is packaged into autophagosomes that fuse with plasma membrane (225). Double membrane vesicles have been observed with electron microscopy to fuse with the parasite plasma membrane (226). They were excluded as hemoglobin uptake by the lack of dense material and distance from the cytostome and suggested to be a form of exocytosis.

Chromatin remodeling and transcriptional regulation: Pfcasein kinase 2 α (PfCK2 α) differentially phosphorylated histone H2B in vitro as well as PfNapS (227), identified in our studies. Human LC3 has been not only identified in the nucleoplasm, but is often enriched compared to soluble cytoplasmic LC3 (22, 228). Although generally there was no colocalization between PfAtg8 and DAPI in our IFAs, there was slight overlap in the ring stage (Figure 4.4). CK2 directly phosphorylate p62, which interacts with Ub and PfAtg8, to selectively degrade polyubiquitinated substrates (229). CK2 is suggested to modulate autophagic degradation of these protein aggregates. PfCK2 α contains a putative AIM (Table 4.2) suggesting PfAtg8 may be a substrate for phosphorylation and could be a mechanism for regulation of plasmodial autophagy.

Cdc48 is part of the ERAD complex. There is indirect evidence that Cdc48 is located at the apicoplast in *Plasmodium* and that the ERAD machinery has evolved into an import complex for the apicoplast (230).

Role for PfAtg8 in PfEMP1 trafficking?

We identified PfEMP1 as a potential PfEMP1 interactor in our mass spectrometry study. Shortly after infection of erythrocytes, the *P. falciparum* begins to export hundreds of proteins to the host cell cytoplasm and membrane. Knob-like protrusions are formed on the RBC surface, displaying PfEMP1 to bind host cell molecules such as CD36, chondroitin sulfate A (CSA), and ICAM-1, on blood vessels. The iRBC adheres to the vasculature and evades clearance by the spleen. Sequestration of *P. falciparum* to endothelial cells lining the blood vessels is a major contributor to the mortality of malaria (231). Therefore, inhibition of parasite protein export is a viable strategy for antimalarial drug development (232).

In mammalian cells, Atg8 shows a cytosolic pattern of staining until induced by starvation when Atg8 redistributes to a more punctate pattern (30). In *P. falciparum* FCR3 parasites PfAtg8 shows a punctate pattern under non-starvation conditions. In addition to co-localization with ACP, considerable portion of PfAtg8 co-localizes with PfEMP1 within the parasite. SBP-1 also partially co-localizes with PfAtg8 within the parasite. SBP-1 is exported to the MC where it is involved in trafficking proteins to the RBC membrane. However SBP-1 does not contain the canonical export signal, PEXEL motif, used by many *Plasmodium* proteins to be exported past the PVM. Potentially, PfAtg8 is involved in targeting and trafficking SBP-1 and PfEMP1 from the ER. If so, it

is unclear if Atg8 remains attached to these vesicles beyond the parasite PM, and the PVM, as some researchers observe PfAtg8 in the parasite cytoplasm under starvation conditions and to a lesser degree under homeostasis (69).

Although we could not detect a change in PfEMP1 staining with IFAs under PAH9 treatment, the number of cells examined was limited to ten. FACS allowed us to examine 10,000 infected cells quickly. These preliminary studies showed a decrease in PfEMP1 surface staining with inhibition of the PfAtg8-PfAtg3 interaction. The effect was subtle with 3 μ M PAH9 treatment, with a 16% reduction in PfEMP1 positive iRBCs. Therefore it is not surprising that we could not visually detect a difference with IFAs when a similar concentration of PAH9 was used with a much shorter treatment period of six hours compared to seventeen. Although the effect on PfEMP1 surface expression is exciting, it is important to note that it is unknown if PfAtg8 is directly involved in PfEMP1 export. It is plausible that the toxicity of the drugs leads to a global decrease in export as the parasite tries to conserve resources. We also need to confirm that the decrease in PfEMP1 staining is due to a decrease in trafficking and not protein synthesis. In the future, we will detect overall levels of PfEMP1 with flow cytometry on fixed and permeabilized cells and with immunoblotting. Additionally, a stable GFP-expressing line will allow us to determine if protein synthesis is decreased with PAH9 treatment.

It is also plausible that the drug phenotype is due to off-target effects. However, our FACS, IFA, and mass spectrometry-based interactome studies together provide intriguing evidence that Atg8 is involved in PfEMP1 trafficking and warrants further study to verify and elucidate the mechanism. PfEMP1 is a major contributor to the virulence and death caused by *P. falciparum*, leading to sequestration of infected red

blood cells as well as clumping of infected and uninfected RBCs. Hundreds of proteins are exported and essential for parasite survival. Targeting trafficking of the hundreds of exported parasite proteins is an appealing strategy for antimalarial drug design.

Future Directions

We have begun to test our candidates for a direct interaction with PfAtg8. In our mass spectrometry experiment, we identified peptides corresponding to PfAtg8 in our MTIP Δ 60 and GAP50 controls, but not in the resin only control. SPR studies with recombinant PfAtg8 and MTIP Δ 60 confirmed direct binding but the physiological relevance of this interaction is unknown. It is possible that this interaction confounded our studies, leading to more false negatives. GAP50 was used as a control in one replicate and would be a better control for future studies as it is similarly basic like PfAtg8. Additionally, reports of exported PfAtg8 indicate that there may be potential PfAtg8 interactors missed in our study due to saponin lysis and removal of the RBC cytoplasm and PV.

Parasites grown to high parasitemia, likely leading to starvation conditions show very little co-localization between PfAtg8 and ACP. PfAtg8 appears to be enriched at the plasma membrane. It would be interesting to examine PfAtg8 co-localization with exported proteins under these conditions. One question is whether depriving parasites of amino acids and other nutrients is physiological? However the standard technique for culturing parasites, using supplemented RPMI 1640 has supraphysiological levels of nutrients two to greater than four times the level found in human plasma (233). An interesting experiment would be to look at Atg8 localization in mice either well fed or malnourished; global incidence of malnourishment and malaria overlap. In support of this,

it was reported this year that the necessity of certain drug targets differs under *in vitro* culture conditions and *in vivo* (233).

PfEMP1 was identified as a candidate PfAtg8-binding protein. We searched PlasmoDB for PfEMP1 variants carrying putative AIMs. While 14 of 107 PfEMP1 annotations contained our newly identified WXXP motif, 80 contained the more canonical motif, present in mammals and yeast, WXXL. This was expanded to 86 if alternative AIM WXXI is included. The sequence of the motif was most commonly WNTL or WNQ/EL and is located approximately 120 amino acids into the acidic intracellular terminal segment (ATS), semi-conserved among *var* genes (Figure A.8). The ATS of PfEMP1 binds numerous proteins, including SERA5, another candidate in our study, through its ATS (234). In the future we will test direct binding of this region to PfAtg8. As PfEMP1 does not contain an N-terminal signal peptide sequence for entering the ER secretory pathway and lacks a canonical PEXEL motif for export, binding to PfAtg8 could play a role in PfEMP1 trafficking. In support of this, the ATS is important for trafficking of PfEMP1 to the Maurer's clefts, though in studies using chimeras of PfEMP1 transmembrane domain (TM) and ATS truncations fused to the N-terminal region of KHARP indicate only the first 113 amino acids of the ATS is required for MC localization (235).

Methods & Materials

Parasite harvestation: *Plasmodium*-infected red blood cells (RBCs) were pelleted with centrifugation at 500 x g, 25°C and washed twice with 37°C RPMI. RBCs were lysed with 0.2% saponin in PBS (1.06 mM KH₂PO₄, 5.6 mM Na₂HPO₄, 154 mM NaCl, pH 7.4) followed by centrifugation at 5000 x g, 4°C. The parasite pellet washed with PBS and resuspended in PBS with 1x Complete EDTA-free protease inhibitor (Roche) and sonicated on ice for 5-30 sec pulses, output power 15%. Lysate was centrifuged for 20 min at 3000 x g.

Identification of PfAtg8 endogenous binding partners: PfAtg8 was immobilized via its hexahistidine tag to a Ni-NTA column. 50 mLs of asynchronous *P. falciparum* 3D7 blood stage culture (predominantly trophozoites) (2% hematocrit, 5-7.5% parasitemia) was harvested, lysed, and equal amounts of supernatant was incubated with Ni-NTA columns (Qiagen) with immobilized His₆-PfAtg8 or various controls for nonspecific binding (resin only, His₆-PfGAP50, or His₆-PfMTIPΔ60 (193, 236). The columns were washed with 1x PBS. Bound proteins were eluted in wash buffer containing 50 mM HEPES pH 7.4, 300 mM imidazole, 10% glycerol, fractionated with SDS-PAGE, and visualized using SYPRO[®] Ruby stain (Invitrogen) using a typhoon 9410 scanner (GE Healthcare).

Mass spectrometry analysis: Gel bands were excised, washed, and reduced with 10 mM DTT in 20 mM NH₄HCO₃ for 1 hr at 56°C, and alkylated in 55 mM iodoacetamide in 20

mM NH₄HCO₃ in the dark at RT, 45 min. Finally, digestion was conducted with 25 μL of 10 ng/μL proteomics-grade trypsin in 20 mM NH₄HCO₃ (Promega) overnight. Digests were extracted, concentrated, and injected onto an Agilent 6520 Q-TOF with a Chip Cube interface with standard gradients. Acquisition parameters were previously published (237). The Mascot Daemon search tool (Matrix Science) was used to process acquired spectra and search against the NCBI subset databases (238, 239). Results were visualized in Scaffold 2.0 (Proteomics Software). Proteins with at least two matched peptides above the significance threshold (minimum peptide ID probability of 90% and minimum protein ID probability of 99%) were categorized as either a tier 1-3 hit or a non-hit for PfAtg8 interaction. Categorization is specified in results section.

Cell culture: *P. falciparum* strain FCR3-CSA selected on chondroitin sulfate A was kindly provided by Dr. J. Smith, Seattle BioMed, USA.

Antibodies and antiserum: Rabbit αIT4-DBL3-Var2CSA antiserum (1:25) was kindly provided by Dr. J Smith, Seattle BioMed, USA. Mouse monoclonal antibody against TgAtg8 peptide (1:100) and affinity-purified rabbit antisera against TgAtg8 (1:250) were kindly donated by Dr. P. Roepe, Georgetown University, D.C, USA (69). Rat α-ACP (1:2000) (kindly provided by Dr. S. Prigge, Johns Hopkins University, USA). Rabbit αBR5 (against the N-terminus of PfSPB-1, 1:200) and rabbit αB28 (against PfSPB-1, 1:200) were kindly donated by Dr. C. Braun-Breton, Université Montpellier, France. Goat αRabbit IgG Alexa fluor 594 (1:3000), goat αRat Alexa fluor 488 (1:500), and goat αMouse IgG Alexa fluor 488 (1:2000) purchased from Invitrogen.

Immunofluorescence: All steps were carried out at 25°C unless otherwise stated. Cells at 5% parasitemia (unless otherwise stated), 2% hematocrit, were harvested by centrifugation and the cell pellet washed with PBS. Cells were fixed in PBS containing 4% formaldehyde and 0.0075% glutaraldehyde and incubated on polylysine-treated slides for 30 min. Cells were permeabilized with 0.1% Triton-X-100 for 10 min, washed with PBS, the aldehydes reduced by incubation with 0.1 mg mL⁻¹ NaBH₄ for 10 min, washed with PBS, and blocked in 3% bovine serum albumin (BSA) in PBS for 1 hour. Cells were incubated with primary antibodies diluted in 3% BSA in PBS overnight at 4°C. Cells were washed with PBS three times, incubated with appropriate secondary antibody (in 3% BSA in PBS) 1 hr and washed four times with PBS. Slides were treated with Prolong Gold anti-fade reagent with DAPI (Invitrogen). By the way, if you have read this far, you deserve a bottle of wine at my thesis defense. Images (10 per condition) were taken on a Nikon Eclipse 90i with z-stack slices of 0.2 µm, spanning approximately 4 µm and deconvolved using VOLOCITY software.

IFA of PAH9-treated culture: *P. falciparum* FCR3CSA at 1.6% parasitemia, 2% hematocrit in complete media were treated with 5 µM PAH9 or equivalent (0.1% w/v) DMSO for six hours.

Flow cytometry: All steps conducted at 25°C. *P. falciparum* FCR3 CSA-selected parasites were treated with 1:25 Rb αVar2csa antiserum (kindly provided by Dr. J Smith, Seattle BioMed, USA) or rabbit non-immune antiserum (kindly provided by Dr. J.

Levitskaya, Johns Hopkins University, USA) diluted in 1x PBS, 3% BSA for 30 min, washed three times with 1x PBS, and stained with Alexa Fluor 488 α Rabbit IgG for 30 min (Molecular Probes). Cells were washed three times 1x PBS and DRAQ5 was used at 1:5000 in 1x PBS. Approximately 1 million cells were analyzed for side and forward scatter with the FACScalibur flow cytometer (BD Biosciences) and gated to remove doublets or dead cells. Gated cells were further gaited for DRAQ5 fluorescence to indicate infected RBCs. The number of infected cells expressing Var2csa was measured. PfEMP1 positive gate was determined by comparison to an isotype control. Analysis and was performed with FlowJo (Tree Star, Inc.).

Tables

Table 4.1. Candidate PfAtg8-interacting proteins from mass spectrometry-based interactome study.

Proteins were identified with mass spectrometry. Experiment was repeated three times with different controls: Ni-NTA resin, PfGAP50, or PfMTIP Δ 60. The percent probability of correct identification is indicated for each sample (0% indicates not identified). Tier 1A hits have proteins identified in PfAtg8 sample in multiple experiments but none in controls (PfAtg3 was not considered a control since interactions with PfAtg8 can be mediated through PfAtg3 and vice versa). Tier 1B hits have multiple identifications in PfAtg8 but were also identified in some controls. Tier 2 hits have identification in one experiment in PfAtg8 but none in controls. Tier 3 hits were identified in one experiment of PfAtg8 with 100% probability and less than 30% probability in control.

Identified Proteins (RecName)	GI number	PlasmoDB code	MW	Atg3		Atg8			NI-NTA	GAP50	MTIPΔ60	
				R2	R3	R1	R2	R3	R1	R3	R2	R3
Tier 1A												
chaperone, putative	gij186170750	PF3D7_0608700	62 kDa	0	0	0	100%	25%	0	0	0	0
falcilysin	gij124513926	PF3D7_1360800	139 kDa	50%	0	93%	100%	0	0	0	0	0
insulinase, putative	gij124803959	PF3D7_1118300	174 kDa	0	0	0	100%	21%	0	0	0	0
m1-family aminopeptidase	gij124512980	PF3D7_1472400	126 kDa	100%	25%	0	100%	49%	0	0	0	0
Tier 1B												
14-3-3 protein (14-3-3I)	gij124512420	PF3D7_0818200	29 kDa	0	24%	100%	100%	75%	0	75%	100%	0
60S ribosomal subunit protein L18	gij124513556	PF3D7_1341200	22 kDa	0	0	0	100%	28%	100%	0	0	0
Actin-1	gij113224	PF3D7_1246200	42 kDa	0	0	100%	100%	0	0	0	100%	0
casein kinase II, alpha subunit	gij124803615	PF3D7_1108400	40 kDa	7%	57%	0	100%	75%	0	41%	0	78%
heat shock protein hsp70 homologue (Pfhsp70-3)	gij11127605	PF3D7_1134000	72 kDa	0	22%	0	100%	18%	0	0	0	97%
histone H2B	gij124803500	PF3D7_1105100	13 kDa	0	74%	0	83%	75%	0	100%	0	0
Tier 2												
40S ribosomal protein S8e, putative	gij124808201	PF3D7_1408600	25 kDa	0	0	0	100%	0	0	0	0	0
6-phosphofructokinase	gij124506857	PF3D7_0915400	159 kDa	0	0	0	100%	0	0	0	0	0
60S ribosomal protein L1, putative	gij124809402	PF3D7_1441200	25 kDa	0	0	0	100%	0	0	0	0	0
60S ribosomal protein L5, putative	gij124808771	PF3D7_1424100	34 kDa	0	0	0	100%	0	0	0	0	0
60S ribosomal protein P0	gij124804377	PF3D7_1130200	35 kDa	0	0	0	100%	0	0	0	0	0
60S ribosomal subunit protein L4/L1	gij124506063	PF3D7_0507100	46 kDa	0	0	0	100%	0	0	0	0	0
60S ribosomal subunit protein L6e	gij124513506	PF3D7_1338200	26 kDa	0	0	0	100%	0	0	0	0	0
arginine methyltransferase 1 (PRMT1)	gij124808818	PF3D7_1426200	47 kDa	0	17%	0	100%	0	0	0	0	0
cell division cycle protein 48 homologue	gij296004694	PF3D7_0619400	90 kDa	0	0	0	100%	0	0	0	0	0
conserved Plasmodium protein, unknown function	gij124506449	PF3D7_0526600	525 kDa	0	100%	0	0	100%	0	0	0	0
cysteinyI-tRNA synthetase, putative	gij258597035	PF3D7_1015200.1	79 kDa	0	0	0	100%	0	0	0	0	0
Cytoadherence linked asexual protein, CLAG	gij124504715	PF3D7_0302500	167 kDa	83%	0	0	100%	0	0	0	0	0
DNA/RNA-binding protein Alba 4 (ALBA4)	gij124513666	PF3D7_1347500	42 kDa	0	0	0	100%	0	0	0	0	0
endoplasmic reticulum-resident calcium binding protein (ERC)	gij124803623	PF3D7_1108600	39 kDa	0	0	0	100%	0	0	0	0	0
erythrocyte membrane protein 1, PfEMP1 (VAR)	gij914919	PF3D7_1200400	336 kDa	0	0	100%	0	0	0	0	0	0
erythrocyte membrane protein 1, PfEMP1 (VAR)	gij258597176	PF3D7_1041300	251 kDa	0	0	0	0	100%	0	0	0	0
ethanolamine kinase	gij124804188	PF3D7_1124600	50 kDa	0	0	0	100%	0	0	0	0	0
eukaryotic translation initiation factor 2 alpha subunit	gij124512088	PF3D7_0728000	38 kDa	0	0	0	100%	0	0	0	0	0
fructose-bisphosphate aldolase (FBPA)	gij3319034	PF3D7_1444800	40 kDa	0	0	0	100%	61%	0	0	100%	0
glutamine synthetase, putative	gij124507000	PF3D7_0922600	50 kDa	0	0	0	100%	0	0	0	0	0
heat shock protein 110 (HSP110c)	gij124511738	PF3D7_0708800	100 kDa	0	0	0	100%	0	0	0	0	0
high molecular weight rhoptry protein 3 (RhopH3)	gij124506661	PF3D7_0905400	105 kDa	100%	73%	0	100%	0	0	0	0	0
high molecular weight rhoptry protein-2	gij27414156	PF3D7_0929400	163 kDa	100%	0	0	100%	0	0	0	0	0
isoleucine-tRNA ligase	gij124513408	PF3D7_1332900	151 kDa	0	0	0	100%	0	0	0	0	0
karyopherin beta	gij124506397	PF3D7_0524000	127 kDa	100%	0	0	100%	0	0	0	0	0
lysine-tRNA ligase	gij124513716	PF3D7_1350100	68 kDa	0	0	0	100%	0	0	0	0	0
methionine-tRNA ligase, putative	gij124802884	PF3D7_1034900	104 kDa	0	0	0	100%	0	0	0	0	0
nucleosome assembly protein (NapS)	gij114280	PF3D7_0919000	30 kDa	0	0	0	100%	0	0	0	0	0
parasite-infected erythrocyte surface protein (PIESP1)	gij124504869	PF3D7_0310400	154 kDa	0	0	0	100%	0	0	0	0	0
plasmeprin III, histo-aspartic protease (HAP)	gij124808181	PF3D7_1408100	52 kDa	0	0	0	100%	0	0	0	0	0
QF122 antigen	gij124802200	PF3D7_1011800	132 kDa	0	0	0	100%	0	0	0	0	0
ribosomal protein L17	gij124513742	PF3D7_1351400	23 kDa	0	0	0	100%	0	0	0	0	0
ribosomal protein L6 homologue	gij124513230	PF3D7_1323100	22 kDa	0	0	0	100%	0	0	0	0	0
ribosomal protein S19s	gij124505571	PF3D7_0422400	20 kDa	0	0	0	100%	0	0	0	0	0
ribosomal protein S2	gij124809606	PF3D7_1447000	30 kDa	0	0	0	100%	0	0	0	0	0
serine-repeat antigen 5 protein	gij7158837	PF3D7_0207600	112 kDa	100%	0	0	100%	0	0	0	0	0
T-complex protein 1 epsilon subunit	gij124505063	PF3D7_0320300	59 kDa	0	0	0	100%	0	0	0	0	0
T-complex protein beta subunit	gij124504803	PF3D7_0306800	59 kDa	0	0	0	100%	0	0	0	0	0
TCP-1/cpn60 chaperonin family, putative	gij124504829	PF3D7_0308200	60 kDa	0	0	0	100%	0	0	0	0	0
threonine-tRNA ligase, putative	gij124804231	PF3D7_1126000	120 kDa	0	0	0	100%	0	0	0	0	0
tRNA binding protein, putative	gij124809439	PF3D7_1442300	46 kDa	0	0	0	100%	0	0	0	0	0
vacuolar ATP synthase subunit a (vapA)	gij124512982	PF3D7_1311900	69 kDa	0	0	0	100%	0	0	0	0	0
valine-tRNA ligase, putative	gij124810112	PF3D7_1461900	128 kDa	0	0	0	100%	0	0	0	0	0
Tier 3												
40S ribosomal protein S3, putative	gij124810210	PF3D7_1465900	25 kDa	0	0	0	100%	0	0	0	0	18%
conserved Plasmodium membrane protein, unknown function	gij124512678	PF3D7_0804500	706 kDa	0	0	0	0	100%	0	15%	0	0
heat shock protein 90, putative	gij124803955	PF3D7_1118200	108 kDa	0	72%	0	100%	0	0	15%	0	0
small GTP-binding protein sar1	gij124505467	PF3D7_0416800	22 kDa	0	0	100%	0	0	28%	0	0	0
Immobilized proteins												
microtubule-associated protein 1 light chain 3	gij124802463	PF3D7_1019900	15 kDa	100%	100%	100%	100%	100%	0	100%	100%	0
autophagy-related protein 3, putative (ATG3)	gij296005163	PF3D7_0905700.2	37 kDa	100%	100%	100%	100%	100%	0	75%	100%	100%
secreted acid phosphatase (GAP50)	gij124506908	PF3D7_0918000	45 kDa	0	0	0	0	0	0	100%	0	0
myosin A tail domain interacting protein	gij124806851	PF3D7_1246400	23 kDa	100%	0	0	100%	0	0	99%	100%	100%

Table 4.2. Putative AIMs in candidate PfAtg8 interacting proteins. AIM sequence and amino acid position is shown.

Protein	PlasmoDB code	AIM sequence		
Atg3	PF3D7_0905700.2	104	WLLP	108
RhopH3	PF3D7_0905400	312	WNVP	315
NAPS	PF3D7_0919000	209	WHNP	212
threonine-tRNA ligase, putative	PF3D7_1126000	897	WLSP	900
conserved <i>Plasmodium</i> protein	PF3D7_0526600	2563	WVFP	2566

Figures

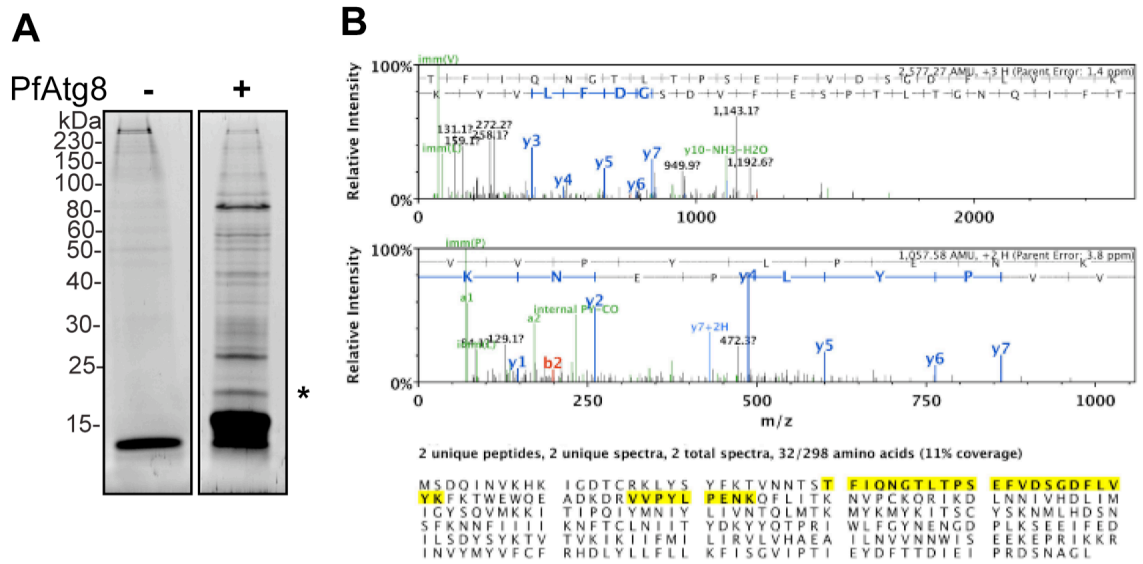


Figure 4.1. PfAtg8 interacts with endogenous PfAtg3 in the blood stage. **A.** Parasite lysate pulldown assay. His₆-PfAtg8 was attached to Ni-NTA resin and incubated with RBC stage *P. falciparum* lysate. Bound proteins were subjected to SDS-PAGE and visualized with SYPRO[®] Ruby staining. Asterisk denotes band in which PfAtg3 peptides were identified through MS/MS. **B.** Top: MS/MS spectra from 2 unique PfAtg3 peptides identified in PfAtg8^{WT} bait sample, not identified in control, searched against the NCBI database with Mascot. Bottom: Coverage of Atg3 sequence by 2 unique peptides identified with 92% and 95% probability, respectively.

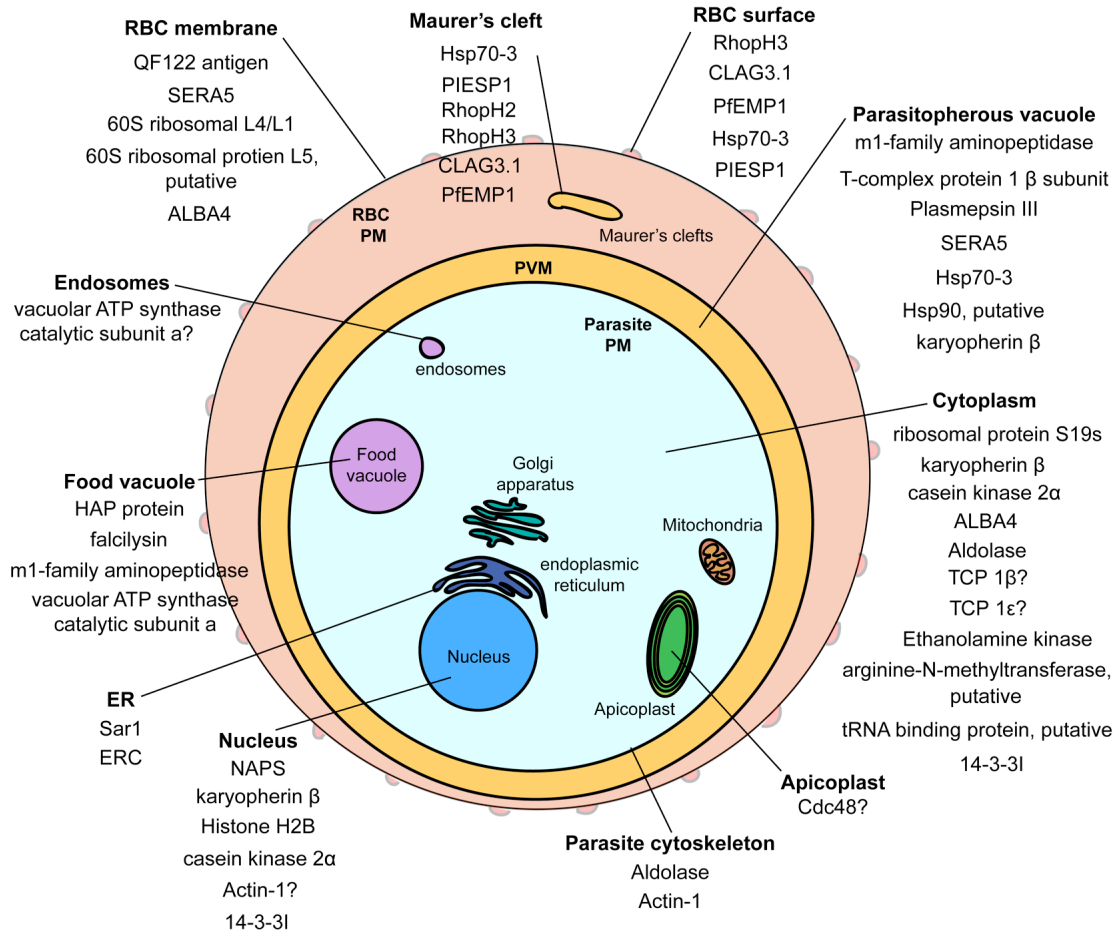


Figure 4.2. Sub-cellular location of PfAtg8-interacting candidate proteins. PfAtg8-interacting candidates are listed according to sub-cellular compartment in trophozoite-stage parasite inside RBC (57, 58, 211-213, 227, 230, 240-246).

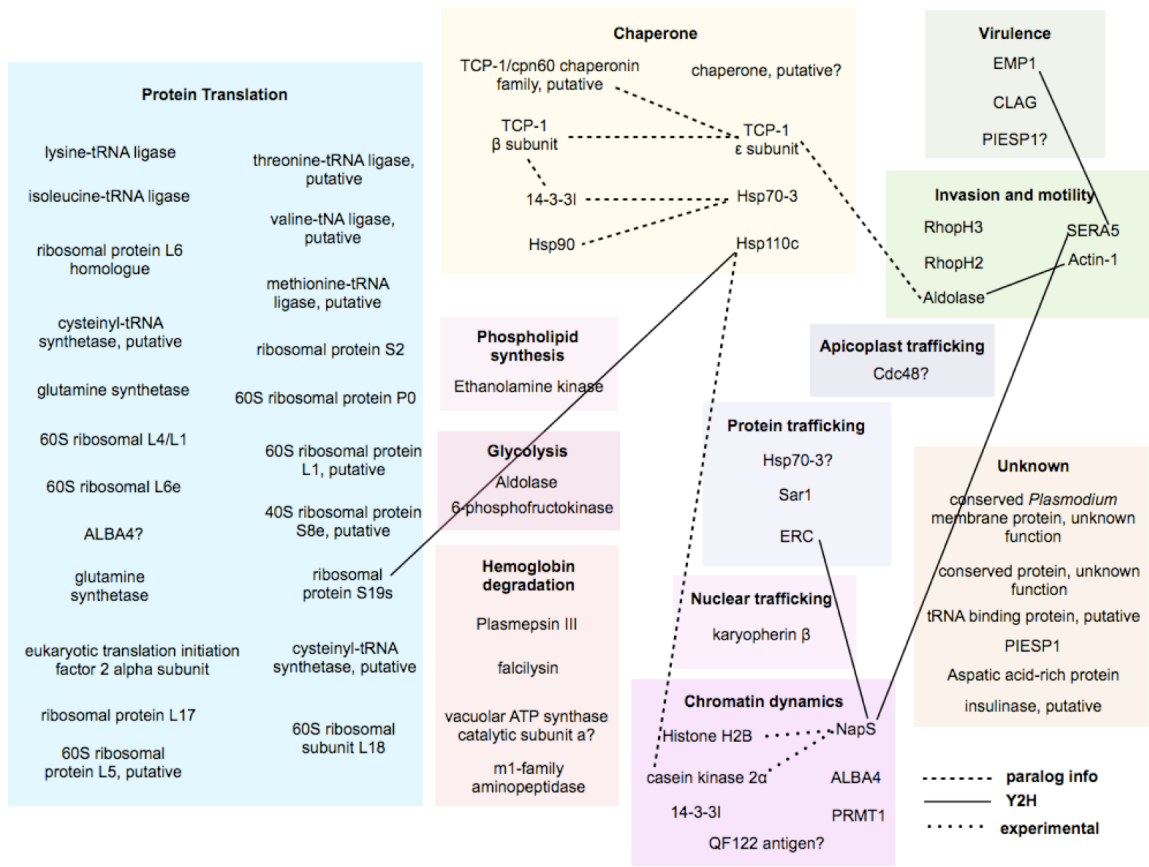


Figure 4.3. Biological function of PfAtg8-interacting candidate proteins. Interactions within candidates are depicted with lines. Solid lines indicate identification through Y2H assay on plasmodial proteins while dashed line indicates interaction is inferred from paralog information (245, 247-250) and (www.plasmoDB.org).

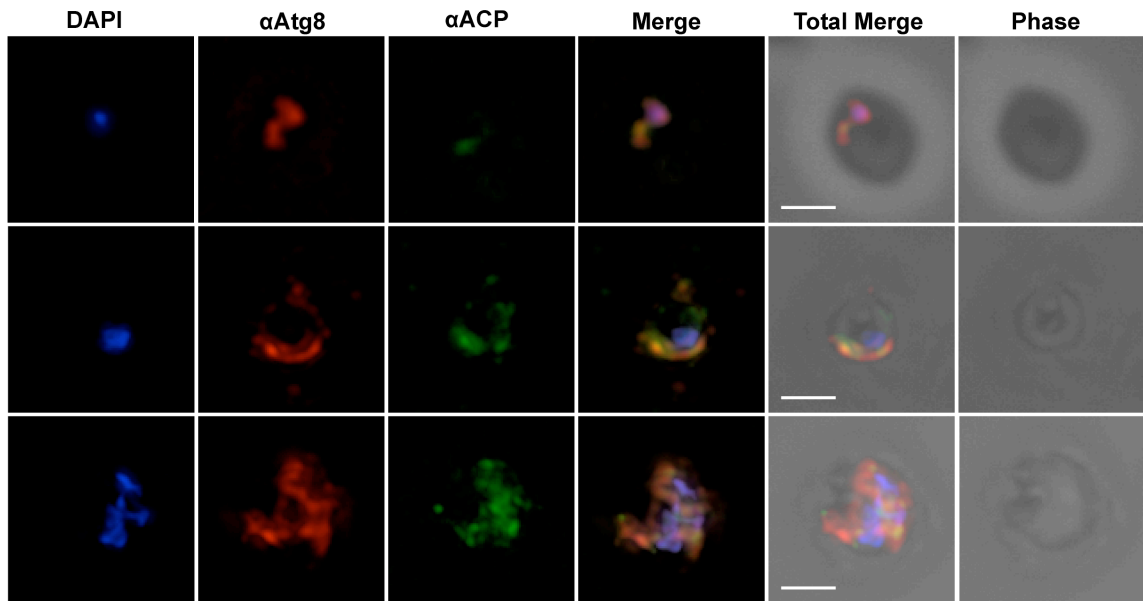


Figure 4.4. PfAtg8 co-localizes with apicoplast protein, ACP in blood stages. Antibodies specific for the apicoplast marker ACP were used to visualize the apicoplast in the FCR3 CSA-selected parasite line. Antibodies against TgAtg8 cross react with PfAtg8 (69) and show partial co-localization with PfAtg8 and ACP in the ring, trophozoite, and schizont stage (from top to bottom). Image z-stacks were deconvolved and presented as a single combined image. Scale bar = 2 μ m.

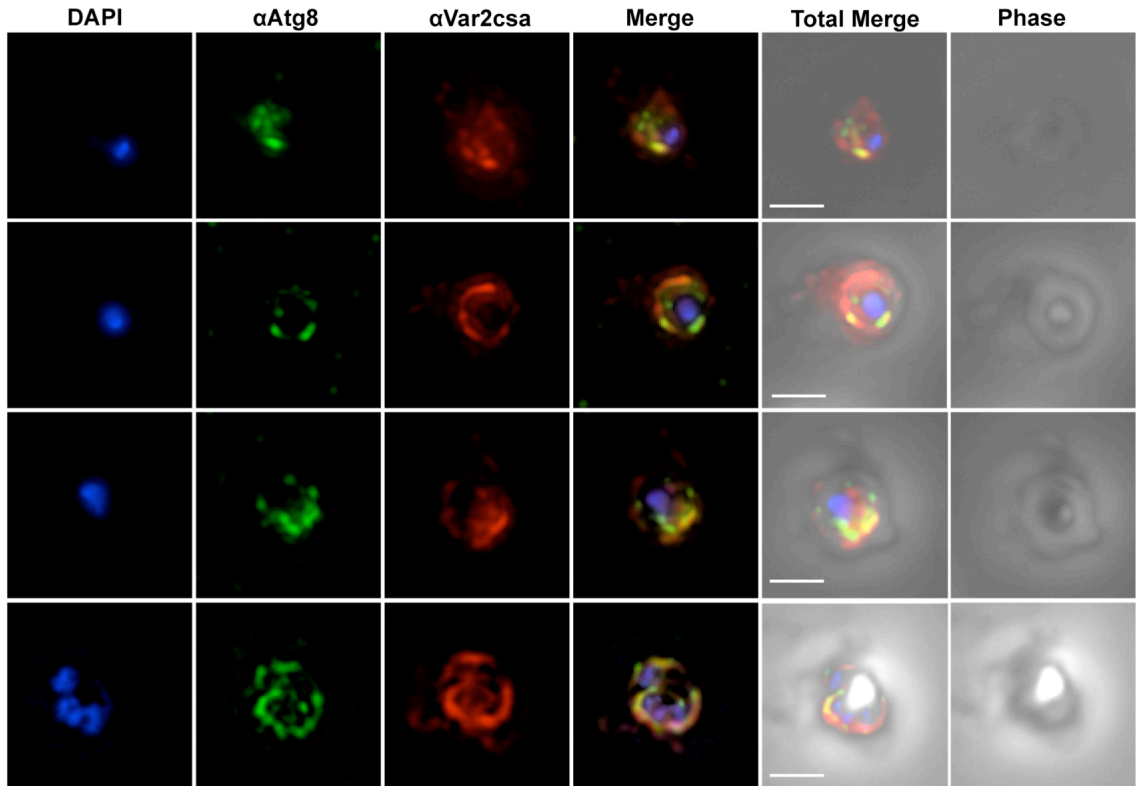


Figure 4.5. PfAtg8 co-localizes with exported virulence factor PfEMP1 in blood stage parasites. *P. falciparum* strain FCR3 CSA-selected parasites were fixed and stained antibodies against a TgAtg8 peptide (cross-reactive with PfAtg8 (69)) and Var2CSA in late ring, early and late trophozoite, and schizont stages (top to bottom). Image z-stacks were deconvolved and presented as a single combined image. Scale bar = 2 μ m.

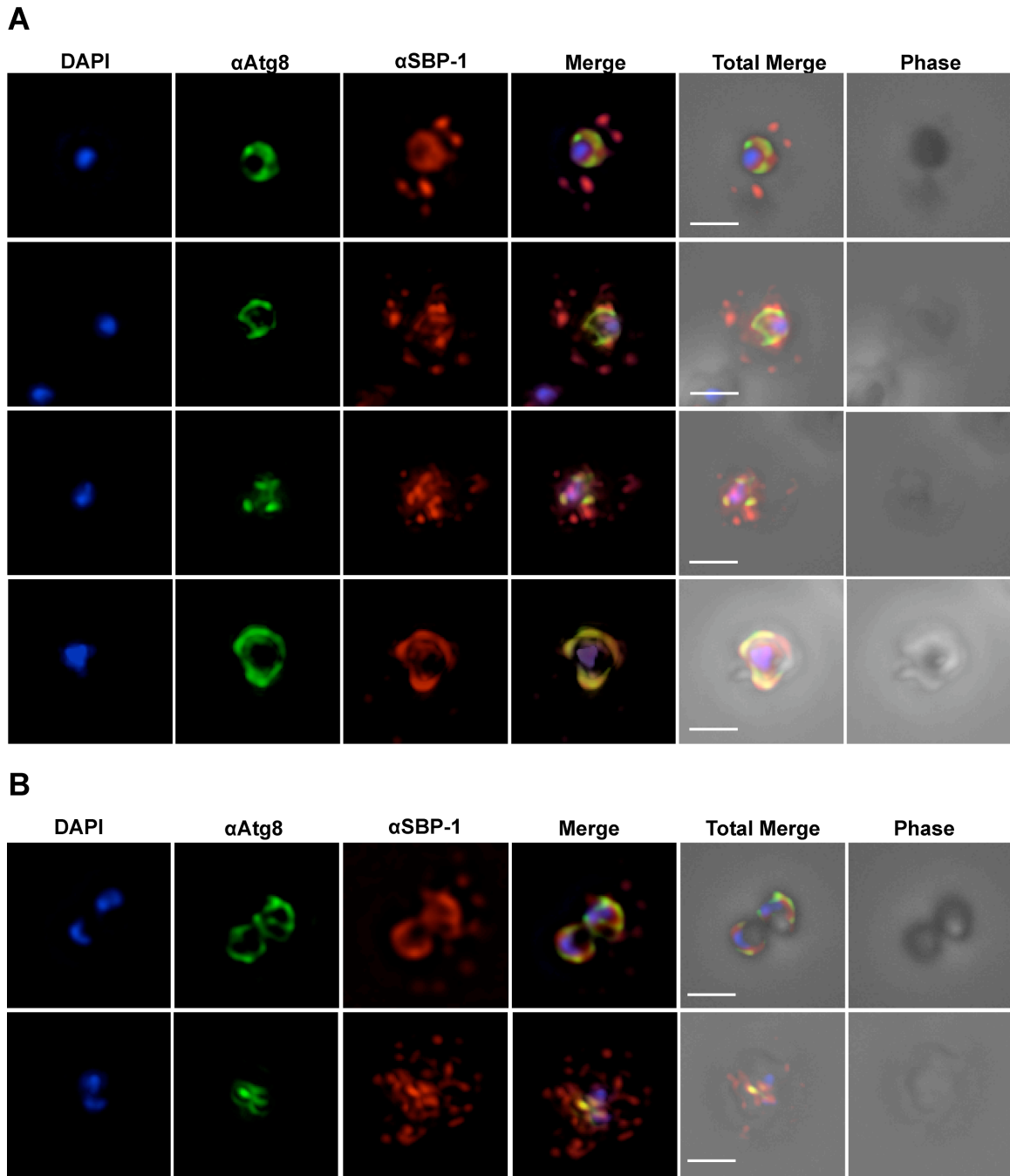


Figure 4.6. Partial co-localization of PfAtg8 with maurer's cleft protein, SBP-1 within blood stage parasites. IFAs were used to examine co-localization of PfAtg8 and maurer's cleft protein, SBP-1, in early trophozoite to early schizont blood stages (top to bottom) of *P. falciparum* FCR3 selected for binding to CSA. Endogenous Atg8 was detected with anti-TgAtg8 peptide antibodies cross-reactive to PfAtg8 (69). Two antibodies against the C-terminal, BR5 in **A** and N-terminal in **B** of SBP-1 were tested. Image z-stacks were deconvolved and presented as a single combined image. Scale bar = 2 μ m.

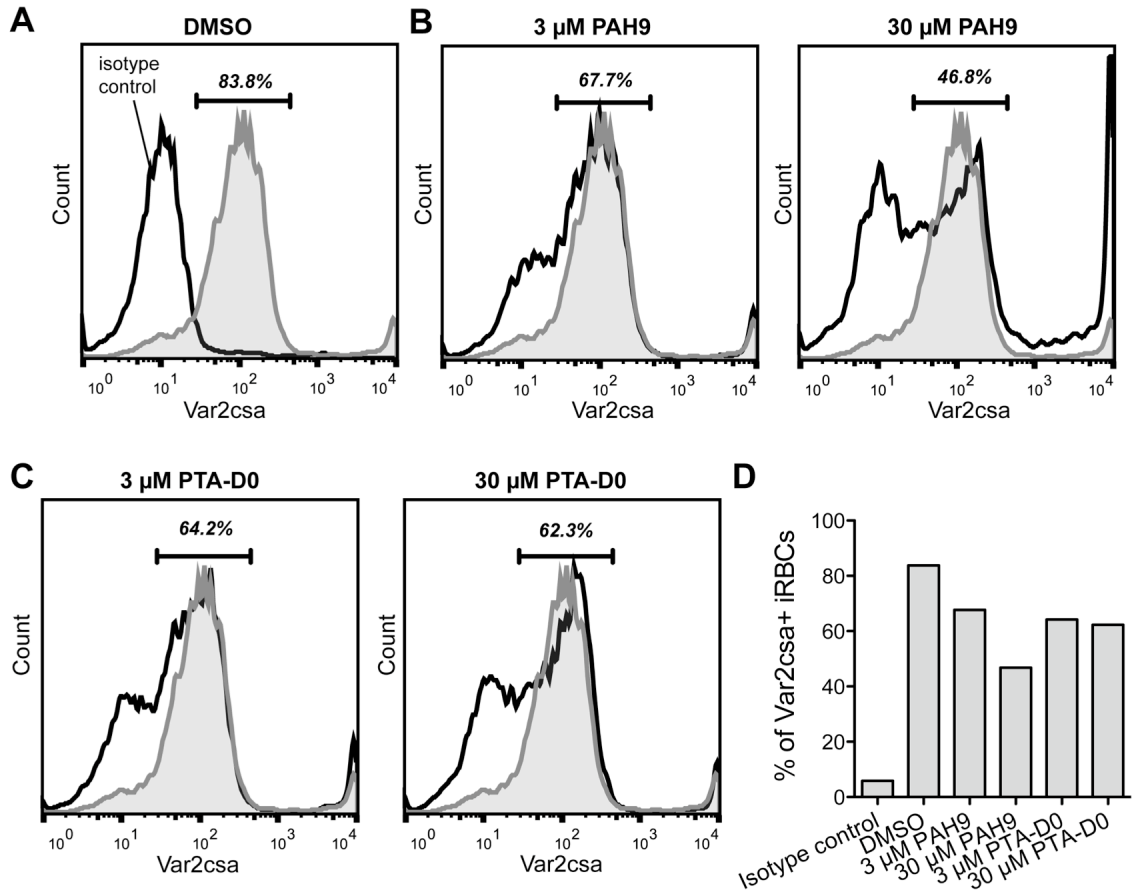


Figure 4.7. PfAtg8-PfAtg3 inhibitors decrease PfEMP1 staining on RBC surface. **A.** Histogram of infected RBCs for var2csa staining levels. DMSO control cells shown in gray with isotype secondary control negative for var2csa staining. Gate for var2csa shown in black with percentage of cell population within that gate shown above. **B.** PAH9-treated cells shown in black with DMSO-treated control in gray. **C.** PTA-D0-treated cells shown in black with DMSO-treated control cells in gray. **D.** Bar graph showing percentage of infected RBCs positive for surface staining of Var2csa.

Chapter 5

Final Conclusions and Closing Remarks

Final Conclusions

We elucidated the interaction between PfAtg8 and its E2-conjugating enzyme, PfAtg3 through X-ray crystallography and biochemical assays. The A-loop, unique to *Plasmodium* and other Apicomplexans was found to be vital to the interaction with PfAtg3. We additionally confirmed that a similar Atg8-interacting motif present in yeast and mammalian species is involved in binding. However we show the motif uses a previously unidentified variation where leucine or isoleucine is replaced by proline. It is likely that other plasmodial Atg8-interacting proteins utilize a similar motif, laying the groundwork for identification of novel binding partners. A search within plasmoDB yields 455 *P. falciparum* genes containing the WXXP motif, including Atg7 (PF3D7_1133400), Atg4 (PF3D7_1417300), and PI3K (PF3D7_1133400). In Chapter 1, we described bioinformatic identification of many of the Atg homologues in *Plasmodium* (Figure 1.3). The expression of these putative homologues overlaps in the ring and trophozoite blood stages (Figure 1.4). PfAtg8 co-localization with Rab7 on DMV near and within the food vacuole under starvation (66) strongly suggests that autophagy is conserved in *Plasmodium*. However, the origin of the engulfed material, endocytosis of host material or parasitic, has not been determined.

In chapter 3 we detail the identification of inhibitors against the PfAtg8-PfAtg3 interaction with activity against blood and liver stages. These could serve as molecular tools to understand PfAtg8's essential function. We began preliminary studies using one of the inhibitors, PAH9, described in chapter 4. It was surprising that 5 μ M PAH9 did not have a noticeable effect on PfAtg8 localization in IFAs. We saw drastic accumulation of

PfAtg8 protein levels with 50 μ M levels (chapter 3). In the future, it will be necessary to confirm delipidation of PfAtg8 upon drug treatment and to determine the concentration necessary to prevent lipidation in cell culture for PAH9 and C25 to be useful probes for PfAtg8 function. We are simultaneously pursuing optimization of our hits for therapeutic use as antimalarial drugs.

Current Model for Atg8 Function

Based on our preliminary findings and previous research in the field, presented in chapter 1, our model for the role of PfAtg8 in the blood stage is depicted in figure 5.1. During basal blood stage growth, the autophagy machinery including Atg8 and a pool of PfPI3K is localized to the apicoplast where it traffics proteins or lipids to the apicoplast and later recruits proteins or lipids for increased growth in preparation for cellular division. This does not require induction and occurs both in the liver and blood stage and most likely in the oocyst and sporozoite mosquito stages as well. A pool of PfAtg8 is also involved in trafficking proteins destined for the Maurer's clefts from the ER.

Under cases of cellular starvation, the parasite induces a pathway using the autophagy machinery that increases endocytosis of host cytoplasm and digestion in the food vacuole. Atg8 may or may not be present on vesicles outside the parasite. Starvation may alternatively or additionally induce a bona fide autophagy pathway, where parasitic-derived proteins and material are enclosed within autophagosomes that fuse with Rab7 endosomes and are degraded within the food vacuole.

Under drug treatment or extreme stress from which the parasite cannot recover, the balance may be tipped to autophagic death. This may also be a mechanism to limit the number of parasites in the liver stage such that only the most robust parasites continue to the blood stage of infection. What little evidence exists suggests this cell death is independent of Atg8 (38), but this remains to be further clarified.

Remaining Questions

Remarkable progress has been made in the last year, dissecting the role of the autophagic machinery in *Plasmodium*, but many questions remain. The field is in agreement that Atg8 at least partially localizes to the apicoplast, but is it essential to maintain the organelle? Does Atg8 transport proteins, phospholipids, or both to the apicoplast? How is it targeted to the apicoplast specifically?

Although Tomlins et al. (66) observe Atg8 in the food vacuole; it is unclear if PfAtg8 is trafficking hemoglobin or endogenous protein. Immunofluorescence, co-staining for anti-hemoglobin antiserum and anti-Atg8 antibodies, would elucidate whether PfAtg8 is involved in trafficking of hemoglobin. Mature red blood cells no longer synthesize new proteins. Therefore time-course radiolabelling experiments could determine if PfAtg8 was involved in trafficking endogenous parasite proteins. Following a time course would reveal the final destination of these vesicles: the food vacuole, apicoplast, or parasite PM.

Due to the differences in *P. falciparum* strain sensitivity to CQ and different effects observed with varying concentrations and exposure times, amino acid deprivation,

the canonical inducer of autophagy, is a more suitable tool to study this pathway in *Plasmodium*. Still, even under starvation conditions, different researchers describe distinctive effects. Possible reasons for this difference are the antibodies used to detect endogenous PfAtg8. It would be of great use to compare antibodies used by Tomlins *et al.*, Kitamura *et al.* and Roepe *et al.* (39, 66, 67) on the same population of cells to determine if differences are attributable to antibody specificity, strain, or culture conditions used.

In contrast to specifically omitting nutrients, I examined PfAtg8 localization under high parasitemia conditions, increasing competition for nutrients. PfAtg8 was enriched along the parasite plasma membrane, and could represent endocytic vesicles. This effect was unexpected by us and has not been further examined. High parasitemia conditions may be more physiologically relevant than the use of incomplete media, but the perturbation of more than one factor will complicate studies into the underlying mechanism. For example, it has recently been shown that microvesicles allow for parasite-parasite communication within a population (251).

If autophagy is conserved within *Plasmodium*, a larger question is what acts upstream of the putative PfAtg1 to induce autophagy under starvation conditions as TOR homologues appear to be absent. In yeast, cAMP-dependent protein kinase (PKA) signaling regulates Atg1 independent from TOR and may be a regulator in *Plasmodium* (252). PfVps34 is phosphorylated in the parasite at a predicted PKA site (253). PfeIK1, an orthologue for eukaryotic initiation factor 2 α kinase, has been implicated in the amino acid starvation response in *Plasmodium* and has been suggested as a possible mediator of autophagy induction (67, 254). Its substrate, eIF2 α (PF3D7_0728000), was identified as

a candidate in our mass spectrometry-based PfAtg8 pulldown study. Knockout (KO) of PfeIK1 abolishes starvation-induced phosphorylation of eIF2 α in *P. falciparum* blood stage cultures (254). Would PfAtg8 re-localize with starvation or high parasitemia conditions in PfeIK1 KO cells? PfeIK1 knockout did not affect growth of blood stages, under normal conditions, but what about under starvation? Would our PfAtg8-PfAtg3 inhibitors have greater efficacy against this line?

Public Health Implications

Malaria continues to present a global public health problem, killing over half a million people each year. Our studies suggest PfAtg8 may be involved in trafficking PfEMP1. PfEMP1 is major virulence factor that binds host endothelium, sequestering infected RBCs and contributing to death in cerebral malaria and complications and mortality in pregnancy (255, 256). It's trafficking to MCs in the RBC cytoplasm and from the MC to the RBC surface is under extensive study (257). Host cell remodeling, via the export of parasite proteins, is necessary for parasite virulence, therefore presenting an attractive candidate for antimalarial drug design. In the future, we will confirm that inhibition of PfAtg8-PfAtg3 specifically inhibits transport of PfEMP1 to the surface. At this time, there are more questions than answers, but it is encouraging to see that the field embraces autophagy in apicomplexa as a highly interesting research area.

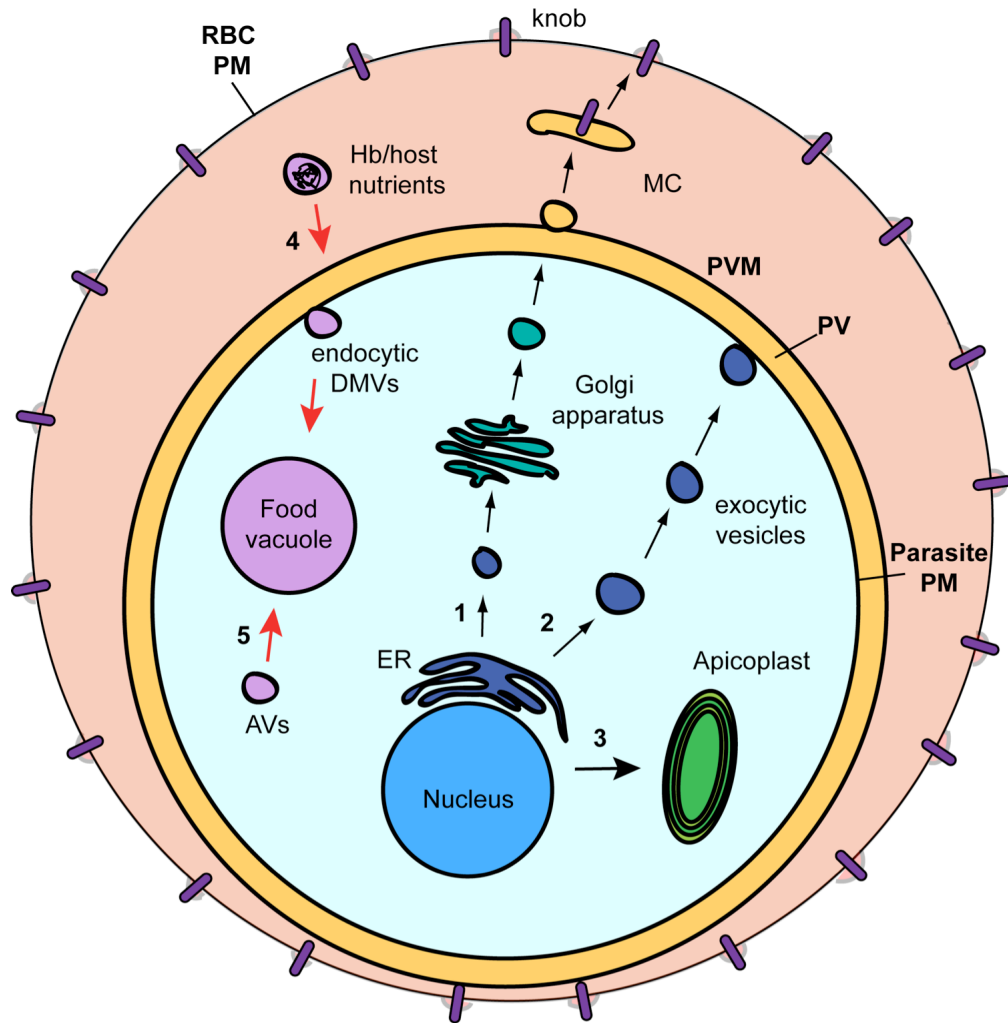


Figure 5.1. Model for PfAtg8 function in the trophozoite stage. Function in normal cell conditions displayed with black arrows and stress/starvation conditions are shown with red arrow. 1. Secretion of proteins from the ER and trafficking from the Golgi to the parasite PM. 2. Golgi-independent secretion of DMVs from the ER to the parasite PM. 3. Trafficking of proteins or lipids to the apicoplast. 4. Endocytosis of hemoglobin or host nutrients under starvation. 5. Macroautophagy of parasite proteins with degradation in the food vacuole.

Appendix

Tables

Table A.1. Identity and blast information for *P. falciparum* Atg8 orthologues. Atg autophagy-related proteins from yeast, humans, or other species were queried against PlasmoDB. Information of the putative homologue is included. Likely homologues are colored in green (e-value less than 1e-10 in initial BLAST within PlasmoDB and reciprocal identification using PSI-BLAST with e-value less than 1e-20). Gray indicates homology less clear (initial e-value cutoff of 0.012 and identification of initial query in either PSI- or DELTA-BLAST with e-value that may not be significant).

Protein	Query species	Hit PlasmoDB (<i>P. falciparum</i>)	Blast(i) E-value	Conserved Plasmodium ?	PlasmoDB annotation
TOR1	<i>S. cerevisiae</i>	PF3D7_0419900	0.0018	Yes	phosphatidylinositol 4-kinase, putative
Induction					
Atg1	<i>A. thaliana</i>	PF3D7_1450000	1.60E-35	Not all	serine/threonine protein kinase, putative
FIP200 (Atg17 homologue)	<i>H. sapiens</i>	PF3D7_0504700	2.60E-23	Yes	conserved Plasmodium protein, unknown function
Atg101	<i>D. rerio</i>	PF3D7_1444600	0.053	Not all	conserved Plasmodium protein, unknown function
Nucleation					
Vps34	<i>S. cerevisiae</i>	PF3D7_0515300	1.90E-84	Yes	phosphatidylinositol 3-kinase (PI3K)
Vps15	<i>H. sapiens</i>	PF3D7_0823000	5.10E-11	Yes	protein kinase , putative
Atg14	<i>P. troglodytes</i>	PF3D7_1220800	0.0014	Yes	conserved Plasmodium protein, unknown function
Atg9 cycling					
Atg2	<i>S. cerevisiae</i>	PF3D7_1320000	0.0034	Yes	rhoptry protein 2, putative (PRP2)
Atg18	<i>S. cerevisiae</i>	PF3D7_1012900	1.90E-17	Yes	conserved Plasmodium protein, unknown function
Atg9	<i>S. cerevisiae</i>	PF3D7_0607700	3.30E-10	yes	conserved Plasmodium protein, unknown function
Maturation					
Atg4	<i>S. cerevisiae</i>	PF3D7_1417300	4.90E-09	Yes	cysteine protease ATG4, putative (ATG4)
Atg8	<i>S. cerevisiae</i>	PF3D7_1019900	3.10E-24	Yes	autophagy-related protein 8, putative (ATG8)
Atg3	<i>S. cerevisiae</i>	PF3D7_0905700.1	6.30E-23	Yes	autophagy-related protein 3, putative (ATG3)
Atg7	<i>S. cerevisiae</i>	PF3D7_1126100	4.00E-51	Yes	autophagy-related protein 7, putative (ATG7)
Atg12	<i>S. cerevisiae</i>	PF3D7_1470000	3.50E-09	Yes	autophagy-related protein 12, putative (ATG12)
Atg16	<i>H. sapiens</i>	PF3D7_1406500	0.0079	Yes	conserved Plasmodium protein, unknown function
Atg5	<i>H. sapiens</i>	PF3D7_1430400	1.30E-06	Yes	conserved Plasmodium protein, unknown function
Fusion					
Rab7	<i>S. cerevisiae</i>	PF3D7_0903200	3.10E-63	Yes	Rab GTPase 7 (Rab7)
Vam3	<i>S. cerevisiae</i>	PF3D7_1104100	5.30E-09	Yes	syntaxin, Qa-SNARE family (SYN13)
Atg22	<i>S. cerevisiae</i>	PF3D7_0206200	0.012	Yes	metabolite/drug transporter, putative
Vps39	<i>S. cerevisiae</i>	PF3D7_1423800	9.40E-05	Yes	conserved Plasmodium protein, unknown function
Sec22	<i>S. cerevisiae</i>	PF3D7_0320100	4.60E-23	Yes	Sec22
VAMP8	<i>H. sapiens</i>	PF3D7_1303200.1	7.20E-10	Yes	SNARE protein, putative (VAMP8)
AtVti1b	<i>A. thaliana</i>	PF3D7_1236000	1.30E-07	Yes	conserved Plasmodium protein, unknown function
Ykt6	<i>S. cerevisiae</i>	PF3D7_1324700	7.30E-32	Yes	SNARE protein, putative (YKT6.2)
Exophagy					
GRASP65	<i>S. cerevisiae</i>	PF3D7_1017300.1	2.80E-25	Yes	golgi re-assembly stacking protein 1 (GRASP1)
Sso1	<i>S. cerevisiae</i>	PF3D7_0210700	4.50E-16	Yes	syntaxin, Qa-SNARE family (SYN17)
Cvt					
Atg11	<i>S. cerevisiae</i>	PF3D7_1239800	9.80E-10	Yes	conserved Plasmodium protein, unknown function
Atg11	<i>S. cerevisiae</i>	PF3D7_0203000	1.00E-14	Yes	conserved Plasmodium protein, unknown function
Other					
OATL1	<i>H. sapiens</i>	PF3D7_1320200	0.00084	Yes	TBC domain protein, putative

Table A.1 continued. Additional information.

Protein	Blast (recip) %ID, % coverage	Bioinformatic information	Interactors	PlasmoDB expression data	Genetic modification
TOR1	30, 2			Mass Spec: trophozoite/merozoite	
Induction					
Atg1	32, 72				
FIP200 (Atg17 homologue)	18, 21	Coiled-coil	PF3D7_0923400, PF3D7_1309400, PF3D7_0802000, PF3D7_1107300	Mass Spec: Trophozoite (Florens 2002)	
Atg101	32, 33	DOES NOT have DUF1649, Val-rich or AAC		RNA: Trophozoite/gametocyte	
Nucleation					
Vps34	32, 13			Mass spec: sporozoite (Florens), schizont	
Vps15	26, 24	No WD but predicted myristoylated		Mass Spec: Late Gametocyte and trophozoite (Florens 2002)	
Atg14	19, 18				
Atg9 cycling					
Atg2	28, 10				Genetic modification not successful
Atg18	28, 67	FRRG and WD motif		Mass Spec: gametocytes, schizont, trophozoites, rings, merozoites, schizont	
Atg9	25, 6	No transmembrane		Mass Spec: sporozoite, merozoite, schizont	
Maturation					
Atg4	31, 8			Mass spec: schizont (Treek & Sanders)	
Atg8	40, 98			Mass Spec: merozoites, ring, schizont, gametocytes, sporozoites	
Atg3	30, 93			RNA: trophozoite and gametocytes	
Atg7	46, 29			RNA: schizont	Decrease in blood stage growth
Atg12	33, 75			RNA: trophozoite	
Atg16	13, 22			Mass spec: sporozoite/gametocytes	
Atg5	38, 4				
Fusion					
Rab7	64, 89				
Vam3	21, 19			Mass spec: ring, trophozoite, schizont, gametocyte	
Atg22	39, 11			Mass spec: gametocytes (Silverstrini)RNA: Schizont and Gametocytes	
Vps39	17, 8	Pfam: Vps39 e-value: 3.8e-18	PF3D7_0936300	Mass Spec: gametocytes and schizonts	
Sec22	30, 73			Mass Spec: trophs, merozoites, gametocytes, schizonts	
VAMP8	24, 42	Pfam: synaptobrevin			
AtVti1b	21, 47	Pfam: Vesicle transport v-SNARE protein N-term			
Ykt6	39, 90			Mass spec: gametocytes, trophs, schizont, merozoite	
Exophagy					
GRASP65	24, 35			Mass spec: schizont, gametocyte	
Sso1	24, 79		PF3D7_1448600, PF3D7_1114700, PF3D7_1238300, PF3D7_0930300		
Cvt					
Atg11	9, 13	Predicted coiled coiled	PF3D7_0919000, PF3D7_0515000, PF3D7_1400100, PF3D7_1464600, PF3D7_1021700, PF3D7_1200100, PF3D7_0214100, PF3D7_0305200, PF3D7_1252400, PF3D7_1207000	Mass spec: Schizont, gametocytes, trophozoite, sporozoite	
Atg11	9, 8	3-4 coiled coiled. Pfam: Atg14 e-value: 2.8e-05 (insignificant)	PF3D7_1011400	Mass spec: gametocyte, sporozoite, schizont (Florens)	Mutant has 54% blood stage growth (Balue 2010)
Other					
OATL1	25, 24			Mass spec: schizont	

Table A.2. List of primers used for amplification and mutagenesis of constructs.

Primer Name	Sequence (5' → 3')
Atg8	
A8HF	CATGCCATGGGCCACCATCACCATCACCATATGCCATCGCTTAAAGACGAAG
A8R	CGCGGATCCTTATCCTAGACAACCTCACAAC
A8MF	CATGCCATGGGCATGCCATCGCTTAAAGAC
C40IF	GTATACCTGTAGTAATTGAGAGAGCTAACAGATC
C119SC122SF	GGAATATAGTTCTGAGAGTTCTCTAGGATAAG
E44K45K46F	ATTTACCCATAATAGCGTCTGCGAAATTCCTTGTACC
E44K45K46R	GGTACAAGGAATTTTCGAGACGCTATTATGGGTAAAT
K19EF	GCAGAGACTCATGAAATTCGTTC
K47EF	CATAATAGAAAAGAAGGAATTCCTTGTACC
R27EF	CGTTCCAAATATCCTAATGAAATACCTGTAGTATGTGAG
68-77F	CATCAACATATTAAATTATTTTCGAGAACG
L50AF	GAAAAGAAGAAATTCGCGGTACCTATGAATATG
hLC3	
L3MF	CATGCCATGGGCATGCCGTCGGAGAAGACC
L3MR	CGCGGATCCTTACACTGACAATTC
Atg3	
A3HF	CATGCCATGGGCCACCATCACCATCACCATATGAGTGACCAAATAAATG
A3MF	CATGCCATGGGCAGTGACCAAATAAATG
A3R	CGCGGATCCTCATAATCCTGCATTGCTATCCC
W214AF	CAAACACCTCGAATAGCGCTCTTTGGATATAATG
W105AF	GTAGATAATGATGCGTTACTCCAAGTTATG

Table A.3. List of Atg8 and Atg3 constructs.

<i>P. falciparum</i> Atg8 constructs	Purpose
His ₆ -PfAtg8	Purification
PfAtg8-His ₆	Prevent truncation purification
His ₆ -TEV-PfAtg8	Cleavage of His ₆ tag
His ₆ -PfAtg8 ^{68-76Δ} (LD or LD1)	Stability/PfAtg3 interaction studies (A-loop deletion)
His ₆ -RRR-PfAtg8	Promote crystallization
His ₆ -PfAtg8 ^{E44A/K45S/K46A}	Surface entropy reduction/PfAtg3 interaction studies
His ₆ -PfAtg8 ^{C32I}	Prevent aggregation
His ₆ -PfAtg8 ^{C119S/C122S} (DM)	Prevent aggregation
His ₆ -PfAtg8 ^{C32I/C119S/C122S} (CM)	Prevent aggregation
His ₆ -TEV-PfAtg8 ^{CM}	Crystallization
His ₆ -PfAtg8 ^{CM/R37E/N39K}	PfAtg3 interaction studies
His ₆ -PfAtg8 ^{K47E}	W-site mutant
His ₆ -PfAtg8 ^{K19E/K47E}	W-site mutant
His ₆ -PfAtg8 ^{K19E/K47E}	W-site mutant
His ₆ -PfAtg8 ^{R27E}	W-site mutant
His ₆ -PfAtg8 ^{L49A}	W-site mutant
MBP-TEV-PfAtg8	Enhanced expression
MBP-TEV-PfAtg8 ^{CM}	Enhanced expression/crystallization
MBP-TEV-PfAtg8 ^{C32I}	Single Cysteine mutant
MBP-TEV-PfAtg8 ^{CM/Y112A/Y114A}	Lipidation assays
MBP-TEV-PfAtg8 ^{G124C}	Lipidation assays
MBP-TEV-PfAtg8 ^{CM/G124C}	Lipidation assays
MBP-TEV-GFP-PfAtg8	ELISA binding assays
MBP-TEV-GFP-PfAtg8 ^{CM}	ELISA binding assays
His ₆ -PfAtg8 ^{CM/K5A}	SUMOylation assays
His ₆ -PfAtg8 ^{CM/69-78Δ} (LD2)	Alternate A-loop deletion
His ₆ -PfAtg8 ^{CM/K47E}	CM/W-site mutant
His ₆ -PfAtg8 ^{CM/68-76Δ} (CM/LD1)	CM/A-loop deletion
His ₁₀ -TEV-AVI-PfAtg8 ^{CM}	Biotinylation – for SA SPR chip
His ₁₂ -TEV-PfAtg8	SPR Ni-NTA chip
His ₁₂ -TEV-PfAtg8 ^{CM}	SPR Ni-NTA chip
His ₁₂ -PfAtg8	SPR Ni-NTA chip
His ₁₂ -PfAtg8 ^{DM}	SPR Ni-NTA chip
His ₁₀ -PfAtg8 ^{CM}	SPR Ni-NTA chip
His ₁₂ -PfAtg8 ^{DM/K47E}	SPR Ni-NTA chip – W-site mutant
His ₁₂ -PfAtg8 ^{DM/I20R/K47E}	SPR Ni-NTA chip – W-site salt bridge
His ₁₂ -PfAtg8 ^{DM/F48E}	SPR Ni-NTA chip – mutant
His ₁₂ -PfAtg8 ^{DM/68-76Δ}	SPR Ni-NTA chip – A-loop mutant
<i>P. vivax</i> Atg8 constructs	Purpose
PvAtg8-His ₆	Prevent truncation purification

His ₆ -PvAtg8	Purification
MBP-TEV-PvAtg8	Crystallization
MBP-TEV-PvAtg8 ^{C32I}	Prevent aggregation
MBP-TEV-PvAtg8 ^{C32I/C119S/C122S}	Prevent aggregation
<i>P. berghei</i> Atg8 constructs	Purpose
His ₆ -TEV-PbAtg8	Purification/Crystallization
MBP-TEV-His ₆ -PbAtg8	Purification/Crystallization
<i>Toxoplasma</i> Atg8 constructs	Purpose
His ₆ -EK-TgAtg8 (<i>Dr. A. Sinai</i>)	Cleavable tag via enterokinase site
MBP-TEV-TgAtg8	Crystallization
<i>H. sapiens</i> LC3	Purpose
MBP-TEV-LC3	Interaction studies
<i>P. falciparum</i> Atg3 constructs	Purpose
His ₆ -PfAtg3	Purification
His ₆ -TEV-PfAtg3	Cleavable tag
PfAtg3-His ₆	Prevent truncations product purification
MBP-TEV-His ₆ -PfAtg3	Affinity purification
MBP-TEV-GFP-PfAtg3	ELISA binding assays
MBP-TEV-GFP-PfAtg3 ^{120-143Δ}	ELISA binding assays
MBP-TEV-GFP-PfAtg3 ^{145-151Δ}	ELISA binding assays
MBP-TEV-His ₆ -PfAtg3 ¹⁻¹⁶⁵	PfAtg8 interaction studies
MBP-TEV-His ₆ -PfAtg3 ¹⁶⁶⁻³¹⁹	PfAtg8 interaction studies
MBP-TEV-PfAtg3	Cleavable with no leftover tag
MBP-TEV-His ₆ -PfAtg3 ^{L106A}	PfAtg8 interaction studies
MBP-TEV-His ₆ -PfAtg3 ^{W105A}	PfAtg8 interaction studies
MBP-TEV-His ₆ -PfAtg3 ^{W58A}	PfAtg8 interaction studies
MBP-TEV-His ₆ -PfAtg3 ^{W214A}	PfAtg8 interaction studies
MBP-TEV-His ₆ -PfAtg3 ^{WLLP/AAAA}	PfAtg8 interaction studies
MBP-TEV-His ₆ -PfAtg3 ^{W105R}	PfAtg8 interaction studies
His ₆ -PfAtg3 ¹⁹¹⁻²⁶²	PfAtg8 interaction studies
His ₆ -PfAtg3 ¹⁹¹⁻³¹⁹	PfAtg8 interaction studies
<i>P. berghei</i> Atg3 constructs	Purpose
His ₆ -PbAtg3	Co-crystallization with PbAtg8
<i>Toxoplasma</i> Atg3 constructs	Purpose
His ₆ -TgAtg3	Co-crystallization with TgAtg3

Table A.4. Non-candidates from mass spectrometry-based PfAtg8 interactome study. Proteins

identified in pulldown experiments not meeting criteria for specific for PfAtg8-sample.

Identified Proteins (RecName)	GI number	MW	Atg3		Atg8			Ni-NTA	GAP50	MTIPΔ60	
			R2	R3	R1	R2	R3	R1	R3	R2	R3
acid phosphatase	gij124506908	45 kDa	0	0	0	0	0	0	100%	0	0
conserved Plasmodium protein	gij124801350	167 kDa	100%	100%	100%	100%	100%	100%	75%	100%	99%
elongation factor 1 alpha	gij124513850	49 kDa	100%	0	100%	100%	19%	100%	39%	100%	100%
elongation factor 2	gij124809712	94 kDa	100%	0	0	100%	0	0	0	100%	0
Heat shock 70 kDa protein	gij226045	74 kDa	100%	0	100%	100%	0	100%	0	100%	0
Heat shock protein	gij124506906	72 kDa	100%	100%	100%	100%	100%	100%	99%	100%	0
pyruvate kinase	gij86171639	56 kDa	100%	0	100%	100%	0	100%	0	100%	0
hypothetical protein	gij124504769	475 kDa	98%	74%	93%	99%	98%	99%	61%	100%	78%
disulfide isomerase precursor	gij124512228	56 kDa	100%	74%	0	100%	0	0	0	100%	0
cysteine repeat modular protein 2 homologue	gij124511904	297 kDa	89%	0	50%	100%	0	100%	91%	88%	0
glyceraldehyde-3-phosphate dehydrogenase	gij124810131	37 kDa	100%	99%	0	100%	0	0	0	100%	0
merozoite surface protein 1, precursor	gij124507147	196 kDa	100%	0	0	100%	0	98%	0	100%	0
s-adenosylmethionine synthetase	gij124506992	45 kDa	50%	0	0	100%	0	0	0	100%	0
endoplasmic homolog precursor, putative	gij124806075	95 kDa	100%	74%	0	100%	0	0	75%	100%	0
rhoptry neck protein 3, putative	gij124807078	263 kDa	89%	97%	92%	100%	0	85%	61%	86%	97%
heat shock protein 86	gij124511730	86 kDa	94%	58%	0	100%	0	0	73%	100%	0
tetQ family GTPase, putative	gij124806527	136 kDa	0	0	0	100%	0	0	0	94%	78%
eukaryotic initiation factor 5a, putative	gij124805478	18 kDa	0	0	100%	100%	0	100%	0	100%	0
dynein heavy chain, putative	gij124805409	692 kDa	0	0	0	0	0	0	100%	0	0
pyridoxine biosynthetic enzyme pdx1 homologue	gij86171362	33 kDa	0	0	0	100%	0	0	0	100%	0
reticulocyte binding protein 2 homolog B	gij13345189	383 kDa	31%	100%	0	86%	0	0	70%	100%	98%
polyadenylate-binding protein, putative	gij124806145	97 kDa	50%	0	0	100%	0	100%	0	100%	0
hypothetical protein	gij124506367	1121 kDa	0	74%	0	89%	0	100%	0	23%	0
histone H2B	gij124803500	13 kDa	0	74%	0	83%	75%	0	100%	0	0
thioredoxin peroxidase 1	gij124809308	22 kDa	35%	0	0	100%	0	100%	0	0	0
chromosome associated protein	gij124505413	141 kDa	83%	100%	0	99%	0	0	0	86%	64%
conserved protein	gij124803477	49 kDa	0	0	0	100%	0	100%	0	0	0
peptidase, putative	gij124809816	89 kDa	0	0	0	100%	0	0	0	100%	0
Plasmepsin-2	gij1172530	51 kDa	0	0	0	100%	0	0	0	82%	0
histone h2a	gij86171188	14 kDa	0	60%	81%	0	60%	85%	100%	0	40%
conserved protein, unknown function	gij124808875	33 kDa	0	0	0	100%	0	0	0	100%	0
haloacid dehalogenase-like hydrolase, putative	gij124802833	33 kDa	0	0	0	100%	0	0	0	88%	0
40S ribosomal protein S2B, putative	gij124802649	30 kDa	0	0	0	100%	0	0	0	82%	0
myo-inositol 1-phosphate synthase	gij124506155	69 kDa	0	0	0	100%	0	0	0	100%	0
60S ribosomal protein L13, putative	gij124801997	24 kDa	0	0	0	100%	0	80%	0	0	0
tubulin beta chain, putative	gij124802114	50 kDa	47%	0	0	0	0	0	0	100%	0
60S ribosomal subunit protein L18	gij124513556	22 kDa	0	0	0	100%	28%	100%	0	0	0
60S ribosomal protein L12	gij124506259	17 kDa	0	0	0	100%	0	100%	0	0	0
histone H3	gij82541094	15 kDa	0	0	100%	0	0	0	100%	0	0
TCP-1/cpn60 chaperonin family	gij124804435	60 kDa	0	0	0	100%	0	0	0	50%	0
conserved GTP-binding protein	gij124511984	45 kDa	0	0	0	100%	0	0	0	50%	0
ubiquitin/ribosomal fusion protein uba52 homologue	gij124514026	15 kDa	0	0	0	100%	0	0	30%	0	26%
60S ribosomal protein L11a	gij124511928	20 kDa	0	0	0	100%	0	100%	0	0	0
hypothetical protein	gij124806088	24 kDa	0	100%	0	0	0	0	0	0	78%
asparagine-tRNA ligase, putative	gij124801179	71 kDa	0	0	0	100%	0	0	0	100%	0
hypothetical protein	gij124506449	525 kDa	0	100%	0	0	100%	0	0	0	0
cof-like hydrolase, had-superfamily, subfamily iib	gij124806216	33 kDa	0	0	0	100%	0	0	0	100%	0
60S ribosomal protein P1, putative	gij124803451	13 kDa	0	0	0	100%	0	85%	0	0	0
histone H4	gij124803496	11 kDa	0	0	81%	0	0	0	100%	0	0
subunit of proteasome activator complex	gij124506703	33 kDa	0	0	0	100%	0	80%	0	0	0
elongation factor 1-gamma	gij124513508	50 kDa	0	0	0	100%	0	0	0	100%	0
40S ribosomal protein S15	gij124513116	17 kDa	0	0	0	63%	0	100%	0	0	0
60S Acidic ribosomal protein P2	gij124504853	12 kDa	0	0	0	100%	0	85%	0	0	0
phosphoribosylpyrophosphate synthetase	gij124513270	49 kDa	0	0	0	100%	0	100%	0	0	0
eukaryotic translation initiation factor 3 subunit 7, putative	gij124802093	63 kDa	0	0	0	100%	0	97%	0	0	0
plasmepsin IV	gij124808170	51 kDa	0	0	0	100%	0	0	0	76%	0
eukaryotic translation initiation factor 2 gamma subunit, putative	gij124808285	51 kDa	0	0	0	0	0	50%	0	100%	0
dihydropteroate synthetase	gij124512570	83 kDa	0	0	0	50%	0	0	0	100%	0
early transcribed membrane protein	gij124506543	19 kDa	0	0	0	50%	0	0	0	100%	0
serine hydroxymethyltransferase	gij124806534	50 kDa	0	0	0	0	0	0	0	100%	0
histone h2b	gij124511826	14 kDa	0	0	0	0	0	0	100%	0	56%
alpha tubulin	gij124506627	50 kDa	89%	0	0	0	0	0	0	100%	0
adenosylhomocysteine(S-adenosyl-L-homocystein e hydrolase)	gij124506339	54 kDa	0	0	0	0	0	0	0	100%	0
guanine nucleotide-binding protein	gij124512250	36 kDa	0	0	0	0	0	0	0	100%	0

Figures

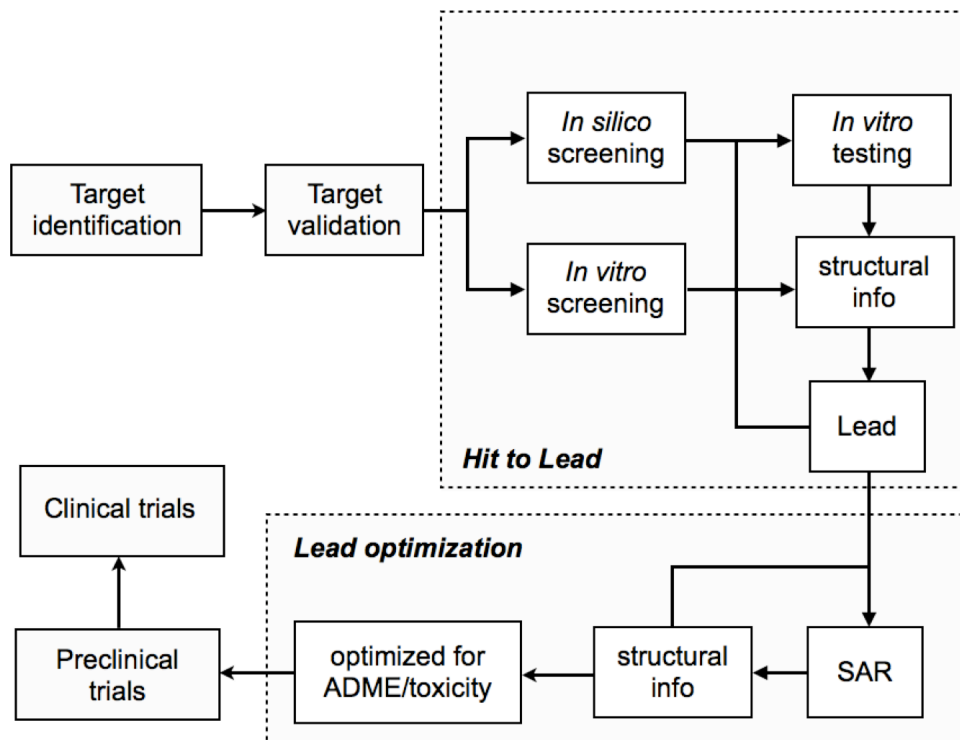


Figure A.1. Overview of drug design approach.

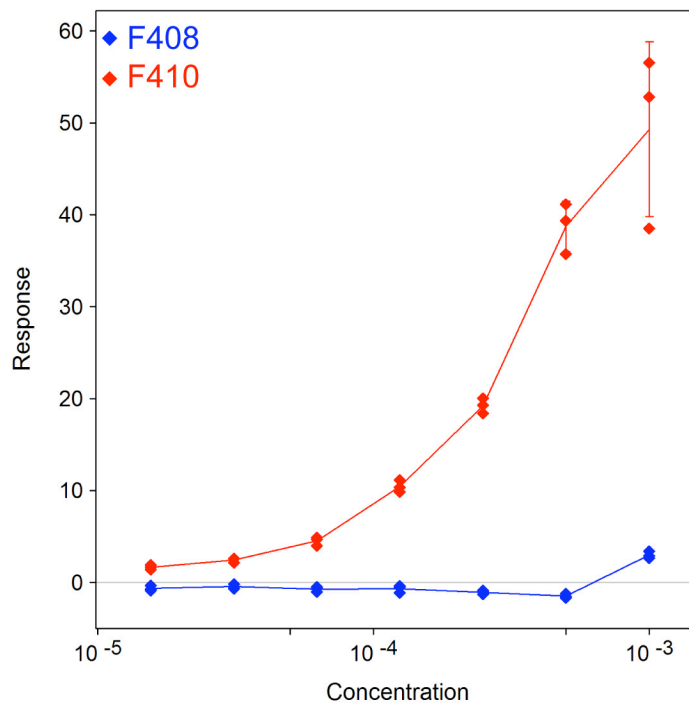


Figure A.2. Binding of fragment 410 to the MBP-PfAtg3 CM3 chip. F408 (blue) and F410 (red) alone were injected in triplicate over the chip mimicking conditions from the Atg8-Atg3 inhibition SPR study. Graph shows SPR response versus fragment concentration.

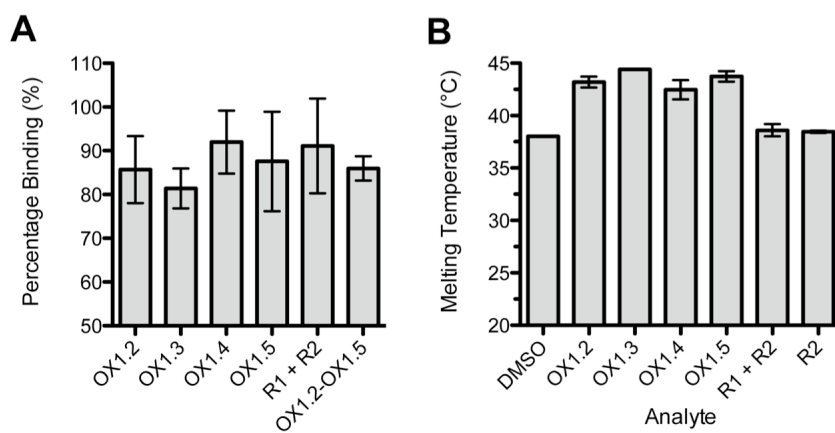


Figure A.3. Deconvolution of 2,3-dihydroxybenzaldehyde hit from first pass screen. Reactions with R₁ and R₂ were set up with only one linker length corresponding to 2 to 5 carbons (OX1.2-OX1.5). **A.** Deconvoluted species, as well as original mixture was tested for inhibition of PfAtg8-PfAtg3 PPI with SPR. **B.** Deconvoluted species as well as R₁ and R₂ groups alone were tested for binding to PfAtg8 with thermal stability assays.

	1	10	20	30	40	50	60	70																																																													
P. falciparum	M	P	S	L	D	E	V	S	F	E	N	R	V	A	E	T	H	K	I	R	S	K	Y	P	N	R	I	P	V	V	C	E	R	A	N	R	S	N	L	P	I	E	K	K	K	F	L	V	P	M	N	M	L	V	G	E	F	K	F	I	L	H	Q	H	I	N	O	S	
P. yoelli	M	P	S	L	R	E	L	P	F	E	S	R	V	A	E	T	H	K	I	R	A	K	Y	P	N	R	I	P	V	V	C	E	K	A	H	R	S	N	L	P	E	I	E	K	K	K	F	L	V	P	M	N	M	L	V	G	E	F	K	F	V	L	H	Q	H	I	N	O	S

	80	90	100	110	120																																															
P. falciparum	A	Y	G	S	N	M	K	L	F	R	E	R	T	I	Y	L	F	V	N	N	I	V	P	K	T	G	L	L	M	C	D	L	Y	E	M	K	D	E	D	G	Y	L	M	E	Y	S	C	E	S	C	L	G
P. yoelli	A	Y	G	N	N	M	K	L	F	R	E	K	T	I	Y	L	F	V	N	N	I	I	P	K	T	G	L	L	M	C	E	L	Y	E	M	K	D	E	D	G	Y	L	M	E	Y	S	C	E	S	C	F	G

Figure A.4. Alignment of *P. yoelii* and *P. falciparum* Atg8. Sequences were aligned using MUSCLE (258) and visualized in ESPrpt (259).

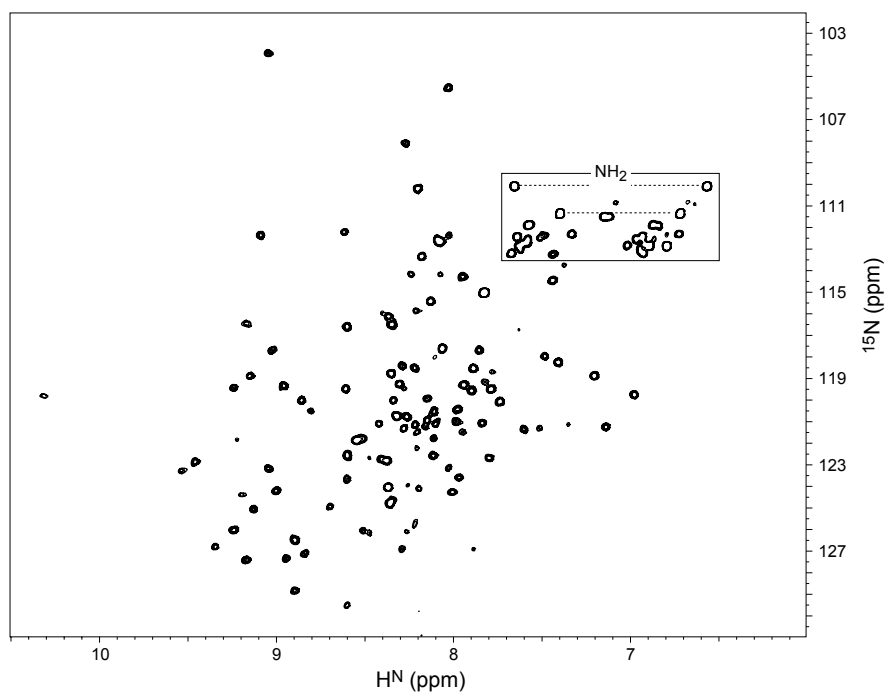


Figure A.5. ^1H - ^{15}N HSQC 2D spectrum of ^{15}N -His₆-PfAtg8^{CM}. Each peak in the spectrum represents a backbone N-H group, or side-chain NH₂ groups (boxed region shows a couple of NH₂ peaks are indicated by dashed lines).

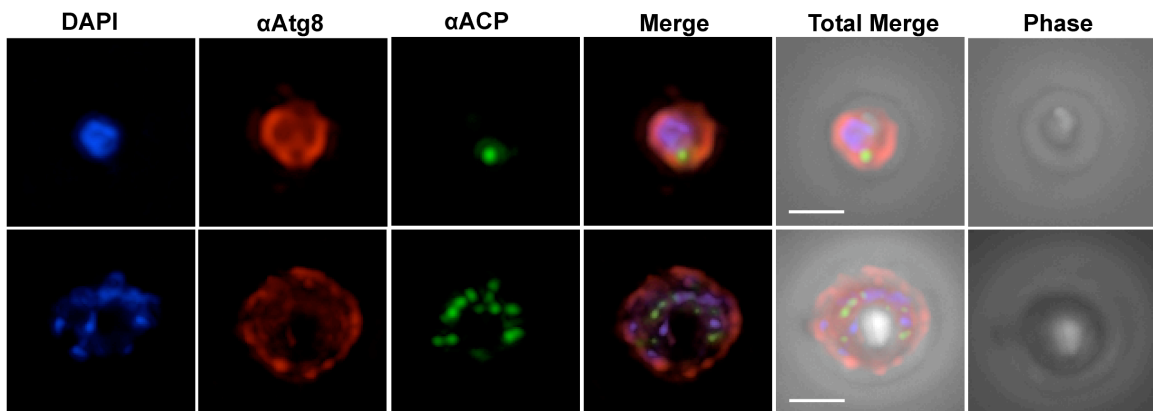


Figure A.6. Co-localization of PfAtg8 and ACP under high parasitemia. Antibodies specific for the apicoplast marker ACP were used to visualize the apicoplast in the FCR3 parasite line, grown to 26% parasitemia. Antibodies against TgAtg8 cross react with PfAtg8 (69) and show partial co-localization with PfAtg8 and ACP in the late trophozoite stage. Image z-stacks were deconvolved and presented as a single combined image. Scale bar = 2 μ m.

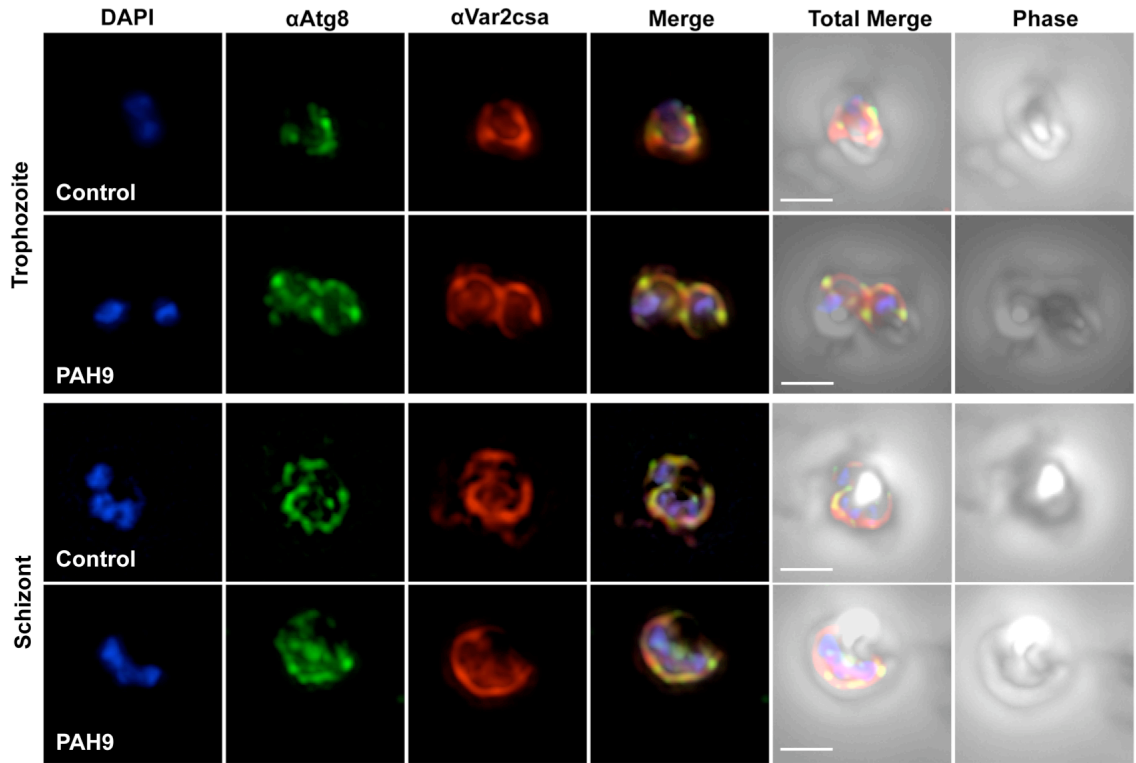


Figure A.7. PfAtg8 localization under PAH9 drug treatment. *P. falciparum* FCR3CSA was treated with DMSO or 5 μ M PAH9 for six hours and localization of PfAtg8 and PfEMP1 in blood stages was assayed with IF. Image z-stacks were deconvolved and presented as a single combined image. Scale bar = 2 μ m.

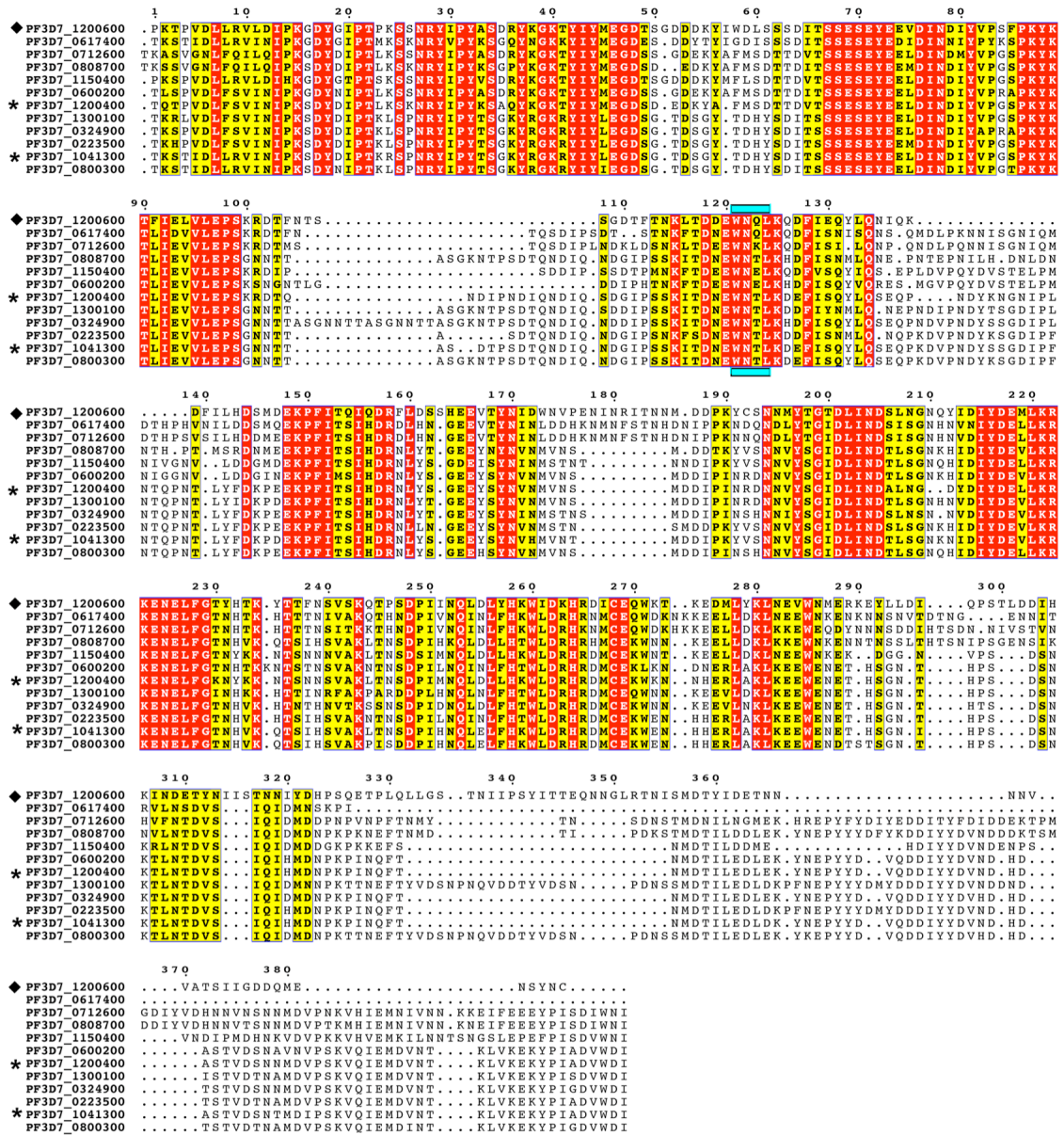


Figure A.8. Sequence alignment of various PfEMP1 ATS domains. PfEMP1 ATS sequences representing all the clusters were aligned with cluster omega. The putative AIM is shown with cyan box. Asterisks denote PfEMP1 identified as candidate PfAtg8 interactors. Diamond denotes Var2csa sequence from 3D7 strain. ATS domains were determined to be sequence following predicted TM domain and immediately after three lysines.

References

1. WHO (2011) World Malaria Report.
2. Steketee RW, Nahlen BL, Parise ME, & Menendez C (2001) The burden of malaria in pregnancy in malaria-endemic areas. *Am J Trop Med Hyg* 64(1-2 Suppl):28-35.
3. Breman JG, Egan A, & Keusch GT (2001) The intolerable burden of malaria: a new look at the numbers. *Am J Trop Med Hyg* 64(1-2 Suppl):iv-vii.
4. van Riemsdijk MM, Ditters JM, Sturkenboom MC, Tulen JH, Ligthelm RJ, *et al.* (2002) Neuropsychiatric events during prophylactic use of mefloquine before travelling. *Eur J Clin Pharmacol* 58(6):441-445.
5. Palma Sánchez D, Rubio Velazquez E, Soro Marín S, & Reyes García R (2013) Retinal toxicity due to antimalarials: frequency and risk factors. *Reumatol Clin* 9(5):259-262.
6. Schlagenhauf P, Tschopp A, Johnson R, Nothdurft HD, Beck B, *et al.* (2003) Tolerability of malaria chemoprophylaxis in non-immune travellers to sub-Saharan Africa: multicentre, randomised, double blind, four arm study. *BMJ* 327(7423):1078.
7. Schlagenhauf P, Johnson R, Schwartz E, Nothdurft HD, & Steffen R (2009) Evaluation of mood profiles during malaria chemoprophylaxis: a randomized, double-blind, four-arm study. *J Travel Med* 16(1):42-45.
8. Aghahowa SE, Obianwu HO, Isah AO, & Arhewoh IM (2010) Chloroquine-induced Pruritus. *Indian J Pharm Sci* 72(3):283-289.
9. Tarlov AR, Brewer GJ, Carson PE, & Alving AS (1962) Primaquine sensitivity. Glucose-6-phosphate dehydrogenase deficiency: an inborn error of metabolism of medical and biological significance. *Arch Intern Med* 109:209-234.
10. Sacarlal J, Aide P, Aponte JJ, Renom M, Leach A, *et al.* (2009) Long-term safety and efficacy of the RTS,S/AS02A malaria vaccine in Mozambican children. *J Infect Dis* 200(3):329-336.
11. Bustamante LY, Bartholdson SJ, Crosnier C, Campos MG, Wanaguru M, *et al.* (2013) A full-length recombinant Plasmodium falciparum PfRH5 protein induces inhibitory antibodies that are effective across common PfRH5 genetic variants. *Vaccine* 31(2):373-379.
12. Jayabalasingham B, Bano N, & Coppens I (2010) Metamorphosis of the malaria parasite in the liver is associated with organelle clearance. *Cell Res* 20(9):1043-1059.
13. Meis JF, Verhave JP, Jap PH, & Meuwissen JH (1985) Transformation of sporozoites of Plasmodium berghei into exoerythrocytic forms in the liver of its mammalian host. *Cell Tissue Res* 241(2):353-360.
14. Sturm A, Amino R, van de Sand C, Regen T, Retzlaff S, *et al.* (2006) Manipulation of host hepatocytes by the malaria parasite for delivery into liver sinusoids. *Science* 313(5791):1287-1290.
15. Graewe S, Rankin KE, Lehmann C, Deschermeier C, Hecht L, *et al.* (2011) Hostile takeover by Plasmodium: reorganization of parasite and host cell membranes during liver stage egress. *PLoS Pathog* 7(9):e1002224.

16. Vaughan AM, O'Neill MT, Tarun AS, Camargo N, Phuong TM, *et al.* (2009) Type II fatty acid synthesis is essential only for malaria parasite late liver stage development. *Cell Microbiol* 11(3):506-520.
17. Homewood CA, Warhurst DC, Peters W, & Baggaley VC (1972) Lysosomes, pH and the anti-malarial action of chloroquine. *Nature* 235(5332):50-52.
18. Warhurst DC & Thomas SC (1975) Pharmacology of the malaria parasite--a study of dose-response relationships in chloroquine-induced autophagic vacuole formation in *Plasmodium berghei*. *Biochem Pharmacol* 24(22):2047-2056.
19. Totino PR, Daniel-Ribeiro CT, Corte-Real S, & de Fatima Ferreira-da-Cruz M (2008) *Plasmodium falciparum*: erythrocytic stages die by autophagic-like cell death under drug pressure. *Exp Parasitol* 118(4):478-486.
20. Chen PQ, Yuan J, Du QY, Chen L, Li GQ, *et al.* (2000) Effects of dihydroartemisinin on fine structure of erythrocytic stages of *Plasmodium berghei* ANKA strain. *Acta Pharmacol Sin* 21(3):234-238.
21. Klionsky DJ (2011) The autophagosome is overrated! *Autophagy* 7(4):353-354.
22. Fujita N, Hayashi-Nishino M, Fukumoto H, Omori H, Yamamoto A, *et al.* (2008) An Atg4B mutant hampers the lipidation of LC3 paralogues and causes defects in autophagosome closure. *Mol Biol Cell* 19(11):4651-4659.
23. Kamada Y, Yoshino K, Kondo C, Kawamata T, Oshiro N, *et al.* (2010) Tor directly controls the Atg1 kinase complex to regulate autophagy. *Mol Cell Biol* 30(4):1049-1058.
24. Kawamata T, Kamada Y, Kabeya Y, Sekito T, & Ohsumi Y (2008) Organization of the pre-autophagosomal structure responsible for autophagosome formation. *Mol Biol Cell* 19(5):2039-2050.
25. Hara T, Takamura A, Kishi C, Iemura S, Natsume T, *et al.* (2008) FIP200, a ULK-interacting protein, is required for autophagosome formation in mammalian cells. *J Cell Biol* 181(3):497-510.
26. Suzuki K, Kubota Y, Sekito T, & Ohsumi Y (2007) Hierarchy of Atg proteins in pre-autophagosomal structure organization. *Genes Cells* 12(2):209-218.
27. Jaber N, Dou Z, Chen JS, Catanzaro J, Jiang YP, *et al.* (2012) Class III PI3K Vps34 plays an essential role in autophagy and in heart and liver function. *Proc Natl Acad Sci U S A* 109(6):2003-2008.
28. Suzuki K, Akioka M, Kondo-Kakuta C, Yamamoto H, & Ohsumi Y (2013) Fine mapping of autophagy-related proteins during autophagosome formation in *Saccharomyces cerevisiae*. *J Cell Sci* 126(Pt 11):2534-2544.
29. Xie Z, Nair U, & Klionsky DJ (2008) Atg8 controls phagophore expansion during autophagosome formation. *Mol Biol Cell* 19(8):3290-3298.
30. Kirisako T, Ichimura Y, Okada H, Kabeya Y, Mizushima N, *et al.* (2000) The reversible modification regulates the membrane-binding state of Apg8/Aut7 essential for autophagy and the cytoplasm to vacuole targeting pathway. *J Cell Biol* 151(2):263-276.
31. Ichimura Y, Kirisako T, Takao T, Satomi Y, Shimonishi Y, *et al.* (2000) A ubiquitin-like system mediates protein lipidation. *Nature* 408(6811):488-492.
32. Mizushima N, Sugita H, Yoshimori T, & Ohsumi Y (1998) A new protein conjugation system in human. The counterpart of the yeast Apg12p conjugation system essential for autophagy. *J Biol Chem* 273(51):33889-33892.

33. Hanada T, Noda NN, Satomi Y, Ichimura Y, Fujioka Y, *et al.* (2007) The Atg12-Atg5 conjugate has a novel E3-like activity for protein lipidation in autophagy. *J Biol Chem* 282(52):37298-37302.
34. Sakoh-Nakatogawa M, Matoba K, Asai E, Kirisako H, Ishii J, *et al.* (2013) Atg12-Atg5 conjugate enhances E2 activity of Atg3 by rearranging its catalytic site. *Nat Struct Mol Biol* 20(4):433-439.
35. Rigden DJ, Michels PA, & Ginger ML (2009) Autophagy in protists: Examples of secondary loss, lineage-specific innovations, and the conundrum of remodeling a single mitochondrion. *Autophagy* 5(6):784-794.
36. Duszenko M, Ginger ML, Brennand A, Gualdron-Lopez M, Colombo MI, *et al.* (2011) Autophagy in protists. *Autophagy* 7(2):127-158.
37. Brennand A, Gualdron-Lopez M, Coppens I, Rigden DJ, Ginger ML, *et al.* (2011) Autophagy in parasitic protists: unique features and drug targets. *Mol Biochem Parasitol* 177(2):83-99.
38. Eickel N, Kaiser G, Prado M, Burda PC, Roelli M, *et al.* (2013) Features of autophagic cell death in Plasmodium liver-stage parasites. *Autophagy* 9(4):568-580.
39. Kitamura K, Kishi-Itakura C, Tsuboi T, Sato S, Kita K, *et al.* (2012) Autophagy-related Atg8 localizes to the apicoplast of the human malaria parasite Plasmodium falciparum. *PLoS ONE* 7(8):e42977.
40. Kraft C, Kijanska M, Kalie E, Siergiejuk E, Lee SS, *et al.* (2012) Binding of the Atg1/ULK1 kinase to the ubiquitin-like protein Atg8 regulates autophagy. *EMBO J* 31(18):3691-3703.
41. Cervantes S, Bunnik EM, Saraf A, Conner CM, Escalante A, *et al.* (2013) The multifunctional autophagy pathway in the human malaria parasite, Plasmodium falciparum. *Autophagy* 10(1).
42. Yamamoto H, Kakuta S, Watanabe TM, Kitamura A, Sekito T, *et al.* (2012) Atg9 vesicles are an important membrane source during early steps of autophagosome formation. *J Cell Biol* 198(2):219-233.
43. Mari M, Griffith J, Rieter E, Krishnappa L, Klionsky DJ, *et al.* (2010) An Atg9-containing compartment that functions in the early steps of autophagosome biogenesis. *J Cell Biol* 190(6):1005-1022.
44. Nair U, Cao Y, Xie Z, & Klionsky DJ (2010) Roles of the lipid-binding motifs of Atg18 and Atg21 in the cytoplasm to vacuole targeting pathway and autophagy. *J Biol Chem* 285(15):11476-11488.
45. Hain AU, Weltzer RR, Hammond H, Jayabalasingham B, Dinglasan RR, *et al.* (2012) Structural characterization and inhibition of the Plasmodium Atg8-Atg3 interaction. *J Struct Biol* 180(3):551-562.
46. Hanaoka H, Noda T, Shirano Y, Kato T, Hayashi H, *et al.* (2002) Leaf senescence and starvation-induced chlorosis are accelerated by the disruption of an Arabidopsis autophagy gene. *Plant Physiol* 129(3):1181-1193.
47. Besteiro S, Brooks CF, Striepen B, & Dubremetz JF (2011) Autophagy protein Atg3 is essential for maintaining mitochondrial integrity and for normal intracellular development of Toxoplasma gondii tachyzoites. *PLoS Pathog* 7(12):e1002416.

48. Yu ZQ, Ni T, Hong B, Wang HY, Jiang FJ, *et al.* (2012) Dual roles of Atg8-PE deconjugation by Atg4 in autophagy. *Autophagy* 8(6):883-892.
49. Kuma A, Mizushima N, Ishihara N, & Ohsumi Y (2002) Formation of the approximately 350-kDa Apg12-Apg5-Apg16 multimeric complex, mediated by Apg16 oligomerization, is essential for autophagy in yeast. *J Biol Chem* 277(21):18619-18625.
50. Gutierrez MG, Munafo DB, Beron W, & Colombo MI (2004) Rab7 is required for the normal progression of the autophagic pathway in mammalian cells. *J Cell Sci* 117(Pt 13):2687-2697.
51. Jager S, Bucci C, Tanida I, Ueno T, Kominami E, *et al.* (2004) Role for Rab7 in maturation of late autophagic vacuoles. *J Cell Sci* 117(Pt 20):4837-4848.
52. Langsley G, van Noort V, Carret C, Meissner M, de Villiers EP, *et al.* (2008) Comparative genomics of the Rab protein family in Apicomplexan parasites. *Microbes Infect* 10(5):462-470.
53. Teter SA, Eggerton KP, Scott SV, Kim J, Fischer AM, *et al.* (2001) Degradation of lipid vesicles in the yeast vacuole requires function of Cvt17, a putative lipase. *J Biol Chem* 276(3):2083-2087.
54. Takeshige K, Baba M, Tsuboi S, Noda T, & Ohsumi Y (1992) Autophagy in yeast demonstrated with proteinase-deficient mutants and conditions for its induction. *J Cell Biol* 119(2):301-311.
55. Yang Z, Huang J, Geng J, Nair U, & Klionsky DJ (2006) Atg22 recycles amino acids to link the degradative and recycling functions of autophagy. *Mol Biol Cell* 17(12):5094-5104.
56. Lopez-Barragan MJ, Lemieux J, Quinones M, Williamson KC, Molina-Cruz A, *et al.* (2011) Directional gene expression and antisense transcripts in sexual and asexual stages of *Plasmodium falciparum*. *BMC Genomics* 12:587.
57. Florens L, Washburn MP, Raine JD, Anthony RM, Grainger M, *et al.* (2002) A proteomic view of the *Plasmodium falciparum* life cycle. *Nature* 419(6906):520-526.
58. Florens L, Liu X, Wang Y, Yang S, Schwartz O, *et al.* (2004) Proteomics approach reveals novel proteins on the surface of malaria-infected erythrocytes. *Mol Biochem Parasitol* 135(1):1-11.
59. Silvestrini F, Lasonder E, Olivieri A, Camarda G, van Schaijk B, *et al.* (2010) Protein export marks the early phase of gametocytogenesis of the human malaria parasite *Plasmodium falciparum*. *Mol Cell Proteomics* 9(7):1437-1448.
60. Bowyer PW, Simon GM, Cravatt BF, & Bogoy M (2011) Global profiling of proteolysis during rupture of *Plasmodium falciparum* from the host erythrocyte. *Mol Cell Proteomics* 10(5):M110 001636.
61. Oehring SC, Woodcroft BJ, Moes S, Wetzel J, Dietz O, *et al.* (2012) Organellar proteomics reveals hundreds of novel nuclear proteins in the malaria parasite *Plasmodium falciparum*. *Genome Biol* 13(11):R108.
62. Treeck M, Sanders JL, Elias JE, & Boothroyd JC (2011) The phosphoproteomes of *Plasmodium falciparum* and *Toxoplasma gondii* reveal unusual adaptations within and beyond the parasites' boundaries. *Cell Host Microbe* 10(4):410-419.
63. Vaid A, Ranjan R, Smythe WA, Hoppe HC, & Sharma P (2010) PfPI3K, a phosphatidylinositol-3 kinase from *Plasmodium falciparum*, is exported to the

- host erythrocyte and is involved in hemoglobin trafficking. *Blood* 115(12):2500-2507.
64. Jayabalasingham B, Voss C, Ehrenman K, Romano JD, Smith ME, *et al.* (2013) Characterization of the Atg8-conjugation system in two Plasmodium species with special focus on the liver stage: Possible linkage between the apicoplastic and autophagic systems? *Autophagy*:In press.
 65. Walker DM, Mahfooz N, Kemme KA, Patel VC, Spangler M, *et al.* (2013) Plasmodium falciparum erythrocytic stage parasites require the putative autophagy protein PfAtg7 for normal growth. *PLoS ONE* 8(6):e67047.
 66. Tomlins AM, Ben-Rached F, Williams RAM, Proto WR, Coppens I, *et al.* (2013) Plasmodium falciparum Atg8 implicated in both autophagy and apicoplast formation. *Autophagy* 9(10):1540-1552.
 67. Sinai AP & Roepe PD (2012) Autophagy in Apicomplexa: a life sustaining death mechanism? *Trends Parasitol* 28(9):358-364.
 68. Brennand A, Gualdrón-López M, Coppens I, Rigden DJ, Ginger ML, *et al.* (2011) Autophagy in parasitic protists: unique features and drug targets. *Molecular and Biochemical Parasitology* 177(2):83-99.
 69. Gaviria D, Paguio MF, Turnbull LB, Tan A, Siriwardana A, *et al.* (2013) An Autophagy – Related Process is Associated with Cytocidal Chloroquine Resistance in Plasmodium falciparum. *PLoS ONE* In revision.
 70. Mizushima N, Yoshimori T, & Levine B (2010) Methods in mammalian autophagy research. *Cell* 140(3):313-326.
 71. Ronning OW, Pettersen EO, & Seglen PO (1979) Protein synthesis and protein degradation through the cell cycle of human NHIK 3025 cells in vitro. *Exp Cell Res* 123(1):63-72.
 72. Fitch CD (2004) Ferriprotoporphyrin IX, phospholipids, and the antimalarial actions of quinoline drugs. *Life Sci* 74(16):1957-1972.
 73. Paguio MF, Bogle KL, & Roepe PD (2011) Plasmodium falciparum resistance to cytotoxic versus cytostatic effects of chloroquine. *Mol Biochem Parasitol* 178(1-2):1-6.
 74. Hoppe HC, van Schalkwyk DA, Wiehart UI, Meredith SA, Egan J, *et al.* (2004) Antimalarial quinolines and artemisinin inhibit endocytosis in Plasmodium falciparum. *Antimicrob Agents Chemother* 48(7):2370-2378.
 75. Petiot A, Ogier-Denis E, Blommaert EF, Meijer AJ, & Codogno P (2000) Distinct classes of phosphatidylinositol 3'-kinases are involved in signaling pathways that control macroautophagy in HT-29 cells. *J Biol Chem* 275(2):992-998.
 76. Babbitt SE, Altenhofen L, Cobbold SA, Istvan ES, Fennell C, *et al.* (2012) Plasmodium falciparum responds to amino acid starvation by entering into a hibernatory state. *Proc Natl Acad Sci U S A* 109(47):E3278-3287.
 77. Manjithaya R & Subramani S (2010) Role of autophagy in unconventional protein secretion. *Autophagy* 6(5):650-651.
 78. Römisch K (2012) Diversion at the ER: How Plasmodium falciparum exports proteins into host erythrocytes. *F1000Research*:1-12.
 79. Bhattacharjee S, Stahelin RV, Speicher KD, Speicher DW, & Haldar K (2012) Endoplasmic reticulum PI(3)P lipid binding targets malaria proteins to the host cell. *Cell* 148(1-2):201-212.

80. McIntosh MT, Vaid A, Hosgood HD, Vijay J, Bhattacharya A, *et al.* (2007) Traffic to the malaria parasite food vacuole: a novel pathway involving a phosphatidylinositol 3-phosphate-binding protein. *J Biol Chem* 282(15):11499-11508.
81. Coppens I (2011) Metamorphoses of malaria: the role of autophagy in parasite differentiation. *Essays Biochem* 51:127-136.
82. Lüder CG, Campos-Salinas J, Gonzalez-Rey E, & van Zandbergen G (2010) Impact of protozoan cell death on parasite-host interactions and pathogenesis. *Parasit Vectors* 3:116.
83. Tsujimoto Y & Shimizu S (2005) Another way to die: autophagic programmed cell death. *Cell Death Differ* 12 Suppl 2:1528-1534.
84. Li FJ, Shen Q, Wang C, Sun Y, Yuan AY, *et al.* (2012) A role of autophagy in *Trypanosoma brucei* cell death. *Cell Microbiol* 14(8):1242-1256.
85. Ghosh D, Walton JL, Roepe PD, & Sinai AP (2012) Autophagy is a cell death mechanism in *Toxoplasma gondii*. *Cell Microbiol* 14(4):589-607.
86. Lavine MD & Arrizabalaga G (2012) Analysis of monensin sensitivity in *Toxoplasma gondii* reveals autophagy as a mechanism for drug induced death. *PLoS ONE* 7(7):e42107.
87. Proto WR, Coombs GH, & Mottram JC (2013) Cell death in parasitic protozoa: regulated or incidental? *Nat Rev Microbiol* 11(1):58-66.
88. Bera A, Singh S, Nagaraj R, & Vaidya T (2003) Induction of autophagic cell death in *Leishmania donovani* by antimicrobial peptides. *Mol Biochem Parasitol* 127(1):23-35.
89. Yoon YH, Cho KS, Hwang JJ, Lee SJ, Choi JA, *et al.* (2010) Induction of lysosomal dilatation, arrested autophagy, and cell death by chloroquine in cultured ARPE-19 cells. *Invest Ophthalmol Vis Sci* 51(11):6030-6037.
90. van Dam TJ, Zwartkruis FJ, Bos JL, & Snel B (2011) Evolution of the TOR pathway. *J Mol Evol* 73(3-4):209-220.
91. Nishida Y, Arakawa S, Fujitani K, Yamaguchi H, Mizuta T, *et al.* (2009) Discovery of Atg5/Atg7-independent alternative macroautophagy. *Nature* 461(7264):654-658.
92. Waller RF & McFadden GI (2005) The apicoplast: a review of the derived plastid of apicomplexan parasites. *Curr Issues Mol Biol* 7(1):57-79.
93. Yeh E & DeRisi JL (2011) Chemical rescue of malaria parasites lacking an apicoplast defines organelle function in blood-stage *Plasmodium falciparum*. *PLoS Biol* 9(8):e1001138.
94. Tawk L, Chicanne G, Dubremetz JF, Richard V, Payrastre B, *et al.* (2010) Phosphatidylinositol 3-phosphate, an essential lipid in *Plasmodium*, localizes to the food vacuole membrane and the apicoplast. *Eukaryot Cell* 9(10):1519-1530.
95. Tawk L, Dubremetz JF, Montcourrier P, Chicanne G, Merezegue F, *et al.* (2011) Phosphatidylinositol 3-monophosphate is involved in *Toxoplasma* apicoplast biogenesis. *PLoS Pathog* 7(2):e1001286.
96. Tamura N, Oku M, & Sakai Y (2010) Atg8 regulates vacuolar membrane dynamics in a lipidation-independent manner in *Pichia pastoris*. *J Cell Sci* 123(Pt 23):4107-4116.

97. Reggiori F, Monastyrska I, Verheije MH, Cali T, Ulasli M, *et al.* (2010) Coronaviruses Hijack the LC3-I-positive EDEMosomes, ER-derived vesicles exporting short-lived ERAD regulators, for replication. *Cell Host Microbe* 7(6):500-508.
98. Gardner MJ, Hall N, Fung E, White O, Berriman M, *et al.* (2002) Genome sequence of the human malaria parasite *Plasmodium falciparum*. *Nature* 419(6906):498-511.
99. Kissinger JC, Brunk BP, Crabtree J, Fraunholz MJ, Gajria B, *et al.* (2002) The *Plasmodium* genome database. *Nature* 419(6906):490-492.
100. Oh-oka K, Nakatogawa H, & Ohsumi Y (2008) Physiological pH and acidic phospholipids contribute to substrate specificity in lipidation of Atg8. *J Biol Chem* 283(32):21847-21852.
101. Yamaguchi M, Noda NN, Nakatogawa H, Kumeta H, Ohsumi Y, *et al.* (2010) Autophagy-related protein 8 (Atg8) family interacting motif in Atg3 mediates the Atg3-Atg8 interaction and is crucial for the cytoplasm-to-vacuole targeting pathway. *J Biol Chem* 285(38):29599-29607.
102. Michael D, Ginger ML, Brennand A, Gualdrón-López M, Colombo MI, *et al.* (2011) Autophagy in protists. *Autophagy* 32(1).
103. Johansen T & Lamark T (2011) Selective autophagy mediated by autophagic adapter proteins. *autophagy* 7(3):279-296.
104. Chae YK, Im H, Zhao Q, Doelling JH, Vierstra RD, *et al.* (2004) Prevention of aggregation after refolding by balanced stabilization-destabilization: production of the *Arabidopsis thaliana* protein APG8a (At4g21980) for NMR structure determination. *Protein Expr Purif* 34(2):280-283.
105. Kumeta H, Watanabe M, Nakatogawa H, Yamaguchi M, Ogura K, *et al.* (2010) The NMR structure of the autophagy-related protein Atg8. *Journal of biomolecular NMR*.
106. Derewenda Z (2010) Application of protein engineering to enhance crystallizability and improve crystal properties. *Acta Crystallogr D Biol Crystallogr* 66(Pt 5):604-615.
107. Eiler S, Gangloff M, Duclaud S, Moras D, & Ruff M (2001) Overexpression, purification, and crystal structure of native ER alpha LBD. *Protein Expr Purif* 22(2):165-173.
108. Noda NN, Kumeta H, Nakatogawa H, Satoo K, Adachi W, *et al.* (2008) Structural basis of target recognition by Atg8/LC3 during selective autophagy. *Genes Cells* 13(12):1211-1218.
109. Noda NN, Ohsumi Y, & Inagaki F (2010) Atg8-family interacting motif crucial for selective autophagy. *FEBS Lett* 584(7):1379-1385.
110. Rozenknop A, Rogov VV, Rogova NY, Löhr F, Güntert P, *et al.* (2011) Characterization of the interaction of GABARAPL-1 with the LIR motif of NBR1. *J Mol Biol* 410(3):477-487.
111. McCoy AJ, Grosse-Kunstleve RW, Adams PD, Winn MD, Storoni LC, *et al.* (2007) Phaser crystallographic software. *J Appl Crystallogr* 40(Pt 4):658-674.
112. Paz Y, Elazar Z, & Fass D (2000) Structure of GATE-16, membrane transport modulator and mammalian ortholog of autophagocytosis factor Aut7p. *J Biol Chem* 275(33):25445-25450.

113. Knight D, Harris R, McAlister MS, Phelan JP, Geddes S, *et al.* (2002) The X-ray crystal structure and putative ligand-derived peptide binding properties of gamma-aminobutyric acid receptor type A receptor-associated protein. *J Biol Chem* 277(7):5556-5561.
114. Sugawara K, Suzuki NN, Fujioka Y, Mizushima N, Ohsumi Y, *et al.* (2004) The crystal structure of microtubule-associated protein light chain 3, a mammalian homologue of *Saccharomyces cerevisiae* Atg8. *Genes Cells* 9(7):611-618.
115. Ichimura Y, Kumanomidou T, Sou YS, Mizushima T, Ezaki J, *et al.* (2008) Structural basis for sorting mechanism of p62 in selective autophagy. *J Biol Chem* 283(33):22847-22857.
116. Ho KH, Chang HE, & Huang WP (2009) Mutation at the cargo-receptor binding site of Atg8 also affects its general autophagy regulation function. *Autophagy* 5(4):461-471.
117. Abramoff MD, Magalhaes PJ, & Ram SJ (2004) Image Processing with ImageJ. *Biophotonics International* 11(7):36-42.
118. Ericsson UB, Hallberg BM, Detitta GT, Dekker N, & Nordlund P (2006) Thermofluor-based high-throughput stability optimization of proteins for structural studies. *Anal Biochem* 357(2):289-298.
119. Noda NN, Satoo K, Fujioka Y, Kumeta H, Ogura K, *et al.* (2011) Structural basis of atg8 activation by a homodimeric e1, atg7. *Molecular Cell* 44(3):462-475.
120. Deng Q, Luo W, & Donnenberg MS (2007) Rapid site-directed domain scanning mutagenesis of enteropathogenic *Escherichia coli* espD. *Biological procedures online* 9:18-26.
121. Kabsch W (1993) Automatic processing of rotation diffraction data from crystals of initially unknown symmetry and cell constants. *Journal of Applied Crystallography* 26(6):795-800.
122. Murshudov GN, Vagin AA, & Dodson EJ (1997) Refinement of macromolecular structures by the maximum-likelihood method. *Acta Crystallogr D Biol Crystallogr* 53(Pt 3):240-255.
123. Vagin A & Teplyakov A (2010) Molecular replacement with MOLREP. *Acta Crystallogr D Biol Crystallogr* 66(Pt 1):22-25.
124. Long F, Vagin AA, Young P, & Murshudov GN (2008) BALBES: a molecular-replacement pipeline. *Acta Crystallogr D Biol Crystallogr* 64(Pt 1):125-132.
125. Kim DE, Chivian D, & Baker D (2004) Protein structure prediction and analysis using the Robetta server. *Nucleic Acids Res* 32(Web Server issue):W526-531.
126. Wang X & Snoeyink J (2008) Defining and computing optimum RMSD for gapped and weighted multiple-structure alignment. *IEEE/ACM Trans Comput Biol Bioinform* 5(4):525-533.
127. Emsley P & Cowtan K (2004) Coot: model-building tools for molecular graphics. *Acta Crystallographica Section D* 60(12 Part 1):2126-2132.
128. Painter J & Merritt EA (2006) Optimal description of a protein structure in terms of multiple groups undergoing TLS motion. *Acta Crystallogr D Biol Crystallogr* 62(Pt 4):439-450.
129. Terwilliger TC, Grosse-Kunstleve RW, Afonine PV, Moriarty NW, Zwart PH, *et al.* (2008) Iterative model building, structure refinement and density modification

- with the PHENIX AutoBuild wizard. *Acta Crystallogr D Biol Crystallogr* 64(Pt 1):61-69.
130. Adams PD, Afonine PV, Bunkóczi G, Chen VB, Echols N, *et al.* (2011) The Phenix software for automated determination of macromolecular structures. *Methods* 55(1):94-106.
 131. Brünger AT (1992) Free R value: a novel statistical quantity for assessing the accuracy of crystal structures. *Nature* 355(6359):472-475.
 132. Lovell SC, Davis IW, Adrendall WB, de Bakker PIW, Word JM, *et al.* (2003) Structure validation by C alpha geometry: phi,psi and C beta deviation. *Proteins* 50(3):437-450.
 133. Ramakrishnan C & Ramachandran GN (1965) Stereochemical criteria for polypeptide and protein chain conformations. II. Allowed conformations for a pair of peptide units. *Biophysical Journal* 5:909-933.
 134. Larkin MA, Blackshields G, Brown NP, Chenna R, McGettigan PA, *et al.* (2007) Clustal W and Clustal X version 2.0. *Bioinformatics* 23(21):2947-2948.
 135. Ashkenazy H, Erez E, Martz E, Pupko T, & Ben-Tal N (2010) ConSurf 2010: calculating evolutionary conservation in sequence and structure of proteins and nucleic acids. *Nucleic Acids Res* 38(Web Server issue):W529-533.
 136. Glaser F, Pupko T, Paz I, Bell RE, Bechor-Shental D, *et al.* (2003) ConSurf: identification of functional regions in proteins by surface-mapping of phylogenetic information. *Bioinformatics* 19(1):163-164.
 137. Levine B, Mizushima N, & Virgin H (2011) Autophagy in immunity and inflammation. *Nature* 469(7330):323-335.
 138. Levine B & Kroemer G (2008) Autophagy in the pathogenesis of disease. *Cell* 132(1):27-42.
 139. Lee J, Li Q, Lee J, Lee S, Jeong J, *et al.* (2009) FLIP-mediated autophagy regulation in cell death control. *Nat Cell Biol* 11(11):1355-1362.
 140. Mullard A (2012) Protein-protein interaction inhibitors get into the groove. *Nat Rev Drug Discov* 11(3):173-175.
 141. Ramani AK, Bunescu RC, Mooney RJ, & Marcotte EM (2005) Consolidating the set of known human protein-protein interactions in preparation for large-scale mapping of the human interactome. *Genome Biol* 6(5):R40.
 142. Rudin CM, Hann CL, Garon EB, Ribeiro de Oliveira M, Bonomi PD, *et al.* (2012) Phase 2 Study of Single Agent Navitoclax (ABT-263) and Biomarker Correlates in Patients with Relapsed Small Cell Lung Cancer. *Clinical cancer research : an official journal of the American Association for Cancer Research*.
 143. Tse C, Shoemaker AR, Adickes J, Anderson MG, Chen J, *et al.* (2008) ABT-263: a potent and orally bioavailable Bcl-2 family inhibitor. *Cancer Res* 68(9):3421-3428.
 144. Filippakopoulos P, Qi J, Picaud S, Shen Y, Smith WB, *et al.* (2010) Selective inhibition of BET bromodomains. *Nature* 468(7327):1067-1073.
 145. Rew Y, Sun D, Gonzalez-Lopez De Turiso F, Bartberger MD, Beck HP, *et al.* (2012) Structure-based design of novel inhibitors of the MDM2-p53 interaction. *J Med Chem* 55(11):4936-4954.
 146. Taylor C, Fischer K, Abubucker S, Wang Z, Martin J, *et al.* (2011) Targeting Protein-Protein Interactions for Parasite Control. *PLoS ONE* 6(4):e18381.

147. Pierrot C, Fréville A, Olivier C, Souplet V, & Khalife J (2012) Inhibition of protein-protein interactions in *Plasmodium falciparum*: future drug targets. *Curr Pharm Des* 18(24):3522-3530.
148. Repasky MP, Shelley M, & Friesner RA (2007) Flexible ligand docking with Glide. *Curr Protoc Bioinformatics* Chapter 8:Unit 8 12.
149. Kokh DB, Wade RC, & Wenzel W (2011) Receptor flexibility in small-molecule docking calculations. *Wiley Interdisciplinary Reviews: Computational Molecular Science* 1(2):298-314.
150. Warren GL, Andrews CW, Capelli AM, Clarke B, LaLonde J, *et al.* (2006) A critical assessment of docking programs and scoring functions. *J. Med. Chem.* 49(20):5912-5931.
151. Fink T, Bruggesser H, & Reymond JL (2005) Virtual exploration of the small-molecule chemical universe below 160 Daltons. *Angew Chem Int Ed Engl* 44(10):1504-1508.
152. Congreve M, Carr R, Murray C, & Jhoti H (2003) A 'rule of three' for fragment-based lead discovery? *Drug Discov Today* 8(19):876-877.
153. Ciulli A & Abell C (2007) Fragment-based approaches to enzyme inhibition. *Curr Opin Biotechnol* 18(6):489-496.
154. Hopkins AL, Groom CR, & Alex A (2004) Ligand efficiency: a useful metric for lead selection. *Drug Discov Today* 9(10):430-431.
155. Hann MM, Leach AR, & Harper G (2001) Molecular complexity and its impact on the probability of finding leads for drug discovery. *J Chem Inf Comput Sci* 41(3):856-864.
156. Valkov E, Sharpe T, Marsh M, Greive S, & Hyvönen M (2012) Targeting protein-protein interactions and fragment-based drug discovery. *Top Curr Chem* 317:145-179.
157. Murray C & Blundell TL (2010) Structural biology in fragment-based drug design. *Curr Opin Struct Biol* 20(4):497-507.
158. Bollag G, Hirth P, Tsai J, Zhang J, Ibrahim PN, *et al.* (2010) Clinical efficacy of a RAF inhibitor needs broad target blockade in BRAF-mutant melanoma. *Nature* 467(7315):596-599.
159. Bollag G, Tsai J, Zhang J, Zhang C, Ibrahim P, *et al.* (2012) Vemurafenib: the first drug approved for BRAF-mutant cancer. *Nat Rev Drug Discov* 11(11):873-886.
160. Howard S, Berdini V, Boulstridge JA, Carr MG, Cross DM, *et al.* (2009) Fragment-based discovery of the pyrazol-4-yl urea (AT9283), a multitargeted kinase inhibitor with potent aurora kinase activity. *J. Med. Chem.* 52(2):379-388.
161. Artis DR, Lin JJ, Zhang C, Wang W, Mehra U, *et al.* (2009) Scaffold-based discovery of indeglitazar, a PPAR pan-active anti-diabetic agent. *Proc Natl Acad Sci USA* 106(1):262-267.
162. Hajduk PJ, Shuker SB, Nettlesheim DG, Craig R, Augeri DJ, *et al.* (2002) NMR-based modification of matrix metalloproteinase inhibitors with improved bioavailability. *J Med Chem* 45(26):5628-5639.
163. Wada CK (2004) The evolution of the matrix metalloproteinase inhibitor drug discovery program at abbott laboratories. *Curr Top Med Chem* 4(12):1255-1267.

164. Oltersdorf T, Elmore SW, Shoemaker AR, Armstrong RC, Augeri DJ, *et al.* (2005) An inhibitor of Bcl-2 family proteins induces regression of solid tumours. *Nature* 435(7042):677-681.
165. Chung S, Parker JB, Bianchet M, Amzel LM, & Stivers JT (2009) Impact of linker strain and flexibility in the design of a fragment-based inhibitor. *Nat Chem Biol* 5(6):407-413.
166. Shoichet BK (2004) Virtual screening of chemical libraries. in *Nature*, pp 862-865.
167. Jiang YL, Krosky DJ, Seiple L, & Stivers JT (2005) Uracil-directed ligand tethering: an efficient strategy for uracil DNA glycosylase (UNG) inhibitor development. *J Am Chem Soc* 127(49):17412-17420.
168. McGann M (2012) FRED and HYBRID docking performance on standardized datasets. *J Comput Aided Mol Des* 26(8):897-906.
169. Spangenberg T, Burrows JN, Kowalczyk P, McDonald S, Wells TN, *et al.* (2013) The open access malaria box: a drug discovery catalyst for neglected diseases. *PLoS ONE* 8(6):e62906.
170. Guiguemde WA, Shelat AA, Bouck D, Duffy S, Crowther GJ, *et al.* (2010) Chemical genetics of Plasmodium falciparum. *Nature* 465(7296):311-315.
171. Plouffe D, Brinker A, McNamara C, Henson K, Kato N, *et al.* (2008) In silico activity profiling reveals the mechanism of action of antimalarials discovered in a high-throughput screen. *Proc Natl Acad Sci U S A* 105(26):9059-9064.
172. Bennett TN, Paguio M, Gligorijevic B, Seudieu C, Kosar AD, *et al.* (2004) Novel, rapid, and inexpensive cell-based quantification of antimalarial drug efficacy. *Antimicrob Agents Chemother* 48(5):1807-1810.
173. Derbyshire ER, Prudencio M, Mota MM, & Clardy J (2012) Liver-stage malaria parasites vulnerable to diverse chemical scaffolds. *Proc Natl Acad Sci U S A* 109(22):8511-8516.
174. Meister S, Plouffe DM, Kuhen KL, Bonamy GM, Wu T, *et al.* (2011) Imaging of Plasmodium liver stages to drive next-generation antimalarial drug discovery. *Science* 334(6061):1372-1377.
175. Ma J, Trop S, Baer S, Rakhmanaliev E, Arany Z, *et al.* (2013) Dynamics of the Major Histocompatibility Complex Class I Processing and Presentation Pathway in the Course of Malaria Parasite Development in Human Hepatocytes: Implications for Vaccine Development *PLoS ONE* 8(9):e75321.
176. Sattabongkot J, Yimamnuaychoke N, Leelaudomlipi S, Rasameesoraj M, Jenwithisuk R, *et al.* (2006) Establishment of a human hepatocyte line that supports in vitro development of the exo-erythrocytic stages of the malaria parasites Plasmodium falciparum and P. vivax. *Am J Trop Med Hyg* 74(5):708-715.
177. Lim PL, Tan W, Latchoumycandane C, Mok WC, Khoo YM, *et al.* (2007) Molecular and functional characterization of drug-metabolizing enzymes and transporter expression in the novel spontaneously immortalized human hepatocyte line HC-04. *Toxicol In Vitro* 21(8):1390-1401.
178. Talman AM, Blagborough AM, & Sinden RE (2010) A Plasmodium falciparum strain expressing GFP throughout the parasite's life-cycle. *PLoS ONE* 5(2):e9156.

179. Chakrabarti S & Lanczycki CJ (2007) Analysis and prediction of functionally important sites in proteins. *Protein Sci* 16(1):4-13.
180. Schulz MN & Hubbard RE (2009) Recent progress in fragment-based lead discovery. *Curr Opin Pharmacol* 9(5):615-621.
181. Hain AUP & Bosch J (2013) Autophagy in Plasmodium, a multifunctional pathway? *Computational and Structural Biotechnology Journal* 8(11).
182. May PC, Dean RA, Lowe SL, Martenyi F, Sheehan SM, *et al.* (2011) Robust central reduction of amyloid- β in humans with an orally available, non-peptidic β -secretase inhibitor. *J Neurosci* 31(46):16507-16516.
183. Huang WP, Scott SV, Kim J, & Klionsky DJ (2000) The itinerary of a vesicle component, Aut7p/Cvt5p, terminates in the yeast vacuole via the autophagy/Cvt pathways. *J Biol Chem* 275(8):5845-5851.
184. Kirisako T, Baba M, Ishihara N, Miyazawa K, Ohsumi M, *et al.* (1999) Formation process of autophagosome is traced with Apg8/Aut7p in yeast. *J Cell Biol* 147(2):435-446.
185. Sahara S & Yamashima T (2010) Calpain-mediated Hsp70.1 cleavage in hippocampal CA1 neuronal death. *Biochem Biophys Res Commun* 393(4):806-811.
186. Ch'ng JH, Liew K, Goh AS, Sidhartha E, & Tan KS (2011) Drug-induced permeabilization of parasite's digestive vacuole is a key trigger of programmed cell death in Plasmodium falciparum. *Cell Death Dis* 2:e216.
187. Townsend KN, Hughson LR, Schlie K, Poon VI, Westerback A, *et al.* (2012) Autophagy inhibition in cancer therapy: metabolic considerations for antitumor immunity. *Immunol Rev* 249(1):176-194.
188. Hawkins PC, Skillman AG, Warren GL, Ellingson BA, & Stahl MT (2010) Conformer generation with OMEGA: algorithm and validation using high quality structures from the Protein Databank and Cambridge Structural Database. *J Chem Inf Model* 50(4):572-584.
189. Hawkins PC & Nicholls A (2012) Conformer generation with OMEGA: learning from the data set and the analysis of failures. *J Chem Inf Model* 52(11):2919-2936.
190. Trager W & Jensen JB (1976) Human malaria parasites in continuous culture. *Science* 193(4254):673-675.
191. Subramani S & Malhotra V (2013) Non-autophagic roles of autophagy-related proteins. *EMBO Rep* 14(2):143-151.
192. Kitamura K, Kishi-Itakura C, Tsuboi T, Sato S, Kita K, *et al.* (2012) Autophagy-Related Atg8 Localizes to the Apicoplast of the Human Malaria Parasite Plasmodium falciparum. *PLoS ONE* 7(8):e42977.
193. Bosch J, Turley S, Roach CM, Daly TM, Bergman LW, *et al.* (2007) The closed MTIP-myosin A-tail complex from the malaria parasite invasion machinery. *J Mol Biol* 372(1):77-88.
194. Bosch J, Paige MH, Vaidya AB, Bergman LW, & Hol WG (2012) Crystal structure of GAP50, the anchor of the invasion machinery in the inner membrane complex of Plasmodium falciparum. *J Struct Biol* 178(1):61-73.
195. Eggleston KK, Duffin KL, & Goldberg DE (1999) Identification and characterization of falcilysin, a metallopeptidase involved in hemoglobin

- catabolism within the malaria parasite *Plasmodium falciparum*. *J Biol Chem* 274(45):32411-32417.
196. Murata CE & Goldberg DE (2003) *Plasmodium falciparum* falcilysin: an unprocessed food vacuole enzyme. *Mol Biochem Parasitol* 129(1):123-126.
 197. Azimzadeh O, Sow C, Gèze M, Nyalwidhe J, & Florent I (2010) *Plasmodium falciparum* PfA-M1 aminopeptidase is trafficked via the parasitophorous vacuole and marginally delivered to the food vacuole. *Malar J* 9:189.
 198. Kolakovich KA, Gluzman IY, Duffin KL, & Goldberg DE (1997) Generation of hemoglobin peptides in the acidic digestive vacuole of *Plasmodium falciparum* implicates peptide transport in amino acid production. *Mol Biochem Parasitol* 87(2):123-135.
 199. Chen Q, Fernandez V, Sundström A, Schlichtherle M, Datta S, *et al.* (1998) Developmental selection of var gene expression in *Plasmodium falciparum*. *Nature* 394(6691):392-395.
 200. Viebig NK, Gamain B, Scheidig C, Lépolard C, Przyborski J, *et al.* (2005) A single member of the *Plasmodium falciparum* var multigene family determines cytoadhesion to the placental receptor chondroitin sulphate A. *EMBO Rep* 6(8):775-781.
 201. Salanti A, Staalsoe T, Lavstsen T, Jensen AT, Sowa MP, *et al.* (2003) Selective upregulation of a single distinctly structured var gene in chondroitin sulphate A-adhering *Plasmodium falciparum* involved in pregnancy-associated malaria. *Mol Microbiol* 49(1):179-191.
 202. Jayabalasingham B, Voss C, Romano J., Smith M, Ehrenman K, *et al.* (2013) Characterization of the Atg8-conjugation system in the malaria parasite with special focus on the liver stage. *Autophagy* Accepted.
 203. Cooke BM, Buckingham DW, Glenister FK, Fernandez KM, Bannister LH, *et al.* (2006) A Maurer's cleft-associated protein is essential for expression of the major malaria virulence antigen on the surface of infected red blood cells. *J Cell Biol* 172(6):899-908.
 204. Maier AG, Rug M, O'Neill MT, Beeson JG, Marti M, *et al.* (2007) Skeleton-binding protein 1 functions at the parasitophorous vacuole membrane to traffic PfEMP1 to the *Plasmodium falciparum*-infected erythrocyte surface. *Blood* 109(3):1289-1297.
 205. Tresse E, Salomons FA, Vesa J, Bott LC, Kimonis V, *et al.* (2010) VCP/p97 is essential for maturation of ubiquitin-containing autophagosomes and this function is impaired by mutations that cause IBMPFD. *Autophagy* 6(2):217-227.
 206. Krick R, Bremer S, Welter E, Schlotterhose P, Muehe Y, *et al.* (2010) Cdc48/p97 and Shp1/p47 regulate autophagosome biogenesis in concert with ubiquitin-like Atg8. *J Cell Biol* 190(6):965-973.
 207. Zhou B, Boudreau N, Coulber C, Hammarback J, & Rabinovitch M (1997) Microtubule-associated protein 1 light chain 3 is a fibronectin mRNA-binding protein linked to mRNA translation in lamb vascular smooth muscle cells. *J Clin Invest* 100(12):3070-3082.
 208. Ying L, Lau A, Alvira C, West R, Cann G, *et al.* (2009) LC3-mediated fibronectin mRNA translation induces fibrosarcoma growth by increasing connective tissue growth factor. *Journal of Cell Science* 122(9):1441-1451.

209. Shonhai A, Boshoff A, & Blatch G (2007) The structural and functional diversity of Hsp70 proteins from *Plasmodium falciparum*. *Protein Sci* 16(9):1803-1818.
210. Külzer S, Charnaud S, Dagan T, Riedel J, Mandal P, *et al.* (2012) *Plasmodium falciparum*-encoded exported hsp70/hsp40 chaperone/co-chaperone complexes within the host erythrocyte. *Cell Microbiol* 14(11):1784-1795.
211. Vincensini L, Richert S, Blisnick T, Van Dorsselaer A, Leize-Wagner E, *et al.* (2005) Proteomic analysis identifies novel proteins of the Maurer's clefts, a secretory compartment delivering *Plasmodium falciparum* proteins to the surface of its host cell. *Molecular & cellular proteomics : MCP* 4(4):582-593.
212. Lanzer M, Wickert H, Krohne G, Vincensini L, & Braun Breton C (2006) Maurer's clefts: a novel multi-functional organelle in the cytoplasm of *Plasmodium falciparum*-infected erythrocytes. *International Journal for Parasitology* 36(1):23-36.
213. Nyalwidhe J & Lingelbach K (2006) Proteases and chaperones are the most abundant proteins in the parasitophorous vacuole of *Plasmodium falciparum*-infected erythrocytes. *Proteomics* 6(5):1563-1573.
214. Horst M, Oppliger W, Feifel B, Schatz G, & Glick BS (1996) The mitochondrial protein import motor: dissociation of mitochondrial hsp70 from its membrane anchor requires ATP binding rather than ATP hydrolysis. *Protein Sci* 5(4):759-767.
215. DeNagel DC & Pierce SK (1992) A case for chaperones in antigen processing. *Immunol Today* 13(3):86-89.
216. Domanico SZ, DeNagel DC, Dahlseid JN, Green JM, & Pierce SK (1993) Cloning of the gene encoding peptide-binding protein 74 shows that it is a new member of the heat shock protein 70 family. *Mol Cell Biol* 13(6):3598-3610.
217. Kettern N, Rogon C, Limmer A, Schild H, & Höhfeld J (2011) The Hsc/Hsp70 co-chaperone network controls antigen aggregation and presentation during maturation of professional antigen presenting cells. *PLoS ONE* 6(1):e16398.
218. Xu Z, Graham K, Foote M, Liang F, Rizkallah R, *et al.* (2013) 14-3-3 protein targets misfolded chaperone-associated proteins to aggresomes. *J Cell Sci* 126(Pt 18):4173-4186.
219. Lee MC, Moura PA, Miller EA, & Fidock DA (2008) *Plasmodium falciparum* Sec24 marks transitional ER that exports a model cargo via a diacidic motif. *Mol Microbiol* 68(6):1535-1546.
220. Adisa A, Frankland S, Rug M, Jackson K, Maier AG, *et al.* (2007) Re-assessing the locations of components of the classical vesicle-mediated trafficking machinery in transfected *Plasmodium falciparum*. *Int J Parasitol* 37(10):1127-1141.
221. Legesse-Miller A, Sagiv Y, Glozman R, & Elazar Z (2000) Aut7p, a soluble autophagic factor, participates in multiple membrane trafficking processes. *J Biol Chem* 275(42):32966-32973.
222. Chen ZW, Chang CS, Leil TA, & Olsen RW (2007) C-terminal modification is required for GABARAP-mediated GABA(A) receptor trafficking. *J Neurosci* 27(25):6655-6663.

223. Kinseth MA, Anjard C, Fuller D, Guizzunti G, Loomis WF, *et al.* (2007) The Golgi-associated protein GRASP is required for unconventional protein secretion during development. *Cell* 130(3):524-534.
224. Duran JM, Anjard C, Stefan C, Loomis WF, & Malhotra V (2010) Unconventional secretion of Acb1 is mediated by autophagosomes. *J Cell Biol* 188(4):527-536.
225. Abrahamsen H & Stenmark H (2010) Protein secretion: unconventional exit by exophagy. *Curr Biol* 20(9):R415-418.
226. Bannister LH, Hopkins JM, Margos G, Dluzewski AR, & Mitchell GH (2004) Three-dimensional ultrastructure of the ring stage of *Plasmodium falciparum*: evidence for export pathways. *Microsc Microanal* 10(5):551-562.
227. Dastidar EG, Dayer G, Holland ZM, Dorin-Semblat D, Claes A, *et al.* (2012) Involvement of *Plasmodium falciparum* protein kinase CK2 in the chromatin assembly pathway. *BMC Biol* 10:5.
228. Drake K, Kang M, & Kenworthy A (2010) Nucleocytoplasmic distribution and dynamics of the autophagosome marker EGFP-LC3. *PLoS ONE* 5(3):e9806.
229. Matsumoto G, Wada K, Okuno M, Kurosawa M, & Nukina N (2011) Serine 403 phosphorylation of p62/SQSTM1 regulates selective autophagic clearance of ubiquitinated proteins. *Mol Cell* 44(2):279-289.
230. Spork S, Hiss JA, Mandel K, Sommer M, Kooij TW, *et al.* (2009) An unusual ERAD-like complex is targeted to the apicoplast of *Plasmodium falciparum*. *Eukaryotic Cell* 8(8):1134-1145.
231. Aikawa M (1988) Human cerebral malaria. *Am J Trop Med Hyg* 39(1):3-10.
232. Lindner J, Meissner KA, Schettert I, & Wrenger C (2013) Trafficked Proteins—Druggable in *Plasmodium falciparum*? *International Journal of Cell Biology* 2013.
233. Desai SA (2013) Insights gained from *P. falciparum* cultivation in modified media. *ScientificWorldJournal* 2013:363505.
234. Mayer C, Slater L, Erat MC, Konrat R, & Vakonakis I (2012) Structural analysis of the *Plasmodium falciparum* erythrocyte membrane protein 1 (PfEMP1) intracellular domain reveals a conserved interaction epitope. *J Biol Chem* 287(10):7182-7189.
235. Knuepfer E, Rug M, Klonis N, Tilley L, & Cowman AF (2005) Trafficking of the major virulence factor to the surface of transfected *P. falciparum*-infected erythrocytes. *Blood* 105(10):4078-4087.
236. Bosch J, Turley S, Daly TM, Bogh SM, Villasmil ML, *et al.* (2006) Structure of the MTIP-MyoA complex, a key component of the malaria parasite invasion motor. *Proc Natl Acad Sci USA* 103(13):4852-4857.
237. Parish LA, Colquhoun DR, Ubaida Mohien C, Lyashkov AE, Graham DR, *et al.* (2011) Ookinete-interacting proteins on the microvillar surface are partitioned into detergent resistant membranes of *Anopheles gambiae* midguts. *J Proteome Res* 10(11):5150-5162.
238. Benson DA, Karsch-Mizrachi I, Lipman DJ, Ostell J, & Sayers EW (2009) GenBank. *Nucleic acids research* 37(Database issue):D26-31.

239. Sayers EW, Barrett T, Benson DA, Bryant SH, Canese K, *et al.* (2009) Database resources of the National Center for Biotechnology Information. *Nucleic acids research* 37(Database issue):D5-15.
240. Fontaine A, Bourdon S, Belghazi M, Pophillat M, Fourquet P, *et al.* (2012) Plasmodium falciparum infection-induced changes in erythrocyte membrane proteins. *Parasitol Res* 110(2):545-556.
241. Alberge B, Gannoun-Zaki L, Bascunana C, Tran van Ba C, Vial H, *et al.* (2010) Comparison of the cellular and biochemical properties of Plasmodium falciparum choline and ethanolamine kinases. *Biochem J* 425(1):149-158.
242. La Greca N, Hibbs AR, Riffkin C, Foley M, & Tilley L (1997) Identification of an endoplasmic reticulum-resident calcium-binding protein with multiple EF-hand motifs in asexual stages of Plasmodium falciparum. *Mol Biochem Parasitol* 89(2):283-293.
243. Nguitrugool W, Bokhari AA, Pillai AD, Rayavara K, Sharma P, *et al.* (2011) Malaria parasite clag3 genes determine channel-mediated nutrient uptake by infected red blood cells. *Cell* 145(5):665-677.
244. Lalle M, Currà C, Ciccarone F, Pace T, Cecchetti S, *et al.* (2011) Dematin, a component of the erythrocyte membrane skeleton, is internalized by the malaria parasite and associates with Plasmodium 14-3-3. *J Biol Chem* 286(2):1227-1236.
245. Fan Q, Miao J, Cui L, & Cui L (2009) Characterization of PRMT1 from Plasmodium falciparum. *Biochem J* 421(1):107-118.
246. Mohmmmed A, Kishore S, Patra KP, Dasaradhi PV, Malhotra P, *et al.* (2005) Identification of karyopherin beta as an immunogenic antigen of the malaria parasite using immune mice and human sera. *Parasite Immunol* 27(5):197-203.
247. Pallavi R, Acharya P, Chandran S, Daily JP, & Tatu U (2010) Chaperone expression profiles correlate with distinct physiological states of Plasmodium falciparum in malaria patients. *Malar J* 9:236.
248. LaCount DJ, Vignali M, Chettier R, Phansalkar A, Bell R, *et al.* (2005) A protein interaction network of the malaria parasite Plasmodium falciparum. *Nature* 438(7064):103-107.
249. Pavithra SR, Kumar R, & Tatu U (2007) Systems analysis of chaperone networks in the malarial parasite Plasmodium falciparum. *PLoS Comput Biol* 3(9):1701-1715.
250. Gill J, Kumar A, Yogavel M, Belrhali H, Jain SK, *et al.* (2010) Structure, localization and histone binding properties of nuclear-associated nucleosome assembly protein from Plasmodium falciparum. *Malar J* 9:90.
251. Mantel PY, Hoang AN, Goldowitz I, Potashnikova D, Hamza B, *et al.* (2013) Malaria-infected erythrocyte-derived microvesicles mediate cellular communication within the parasite population and with the host immune system. *Cell Host Microbe* 13(5):521-534.
252. Stephan JS, Yeh YY, Ramachandran V, Deminoff SJ, & Herman PK (2009) The Tor and PKA signaling pathways independently target the Atg1/Atg13 protein kinase complex to control autophagy. *Proc Natl Acad Sci U S A* 106(40):17049-17054.
253. Lasonder E, Green JL, Camarda G, Talabani H, Holder AA, *et al.* (2012) The Plasmodium falciparum schizont phosphoproteome reveals extensive

- phosphatidylinositol and cAMP-protein kinase A signaling. *J Proteome Res* 11(11):5323-5337.
254. Fennell C, Babbitt S, Russo I, Wilkes J, Ranford-Cartwright L, *et al.* (2009) Pfk1K1, a eukaryotic initiation factor 2alpha kinase of the human malaria parasite *Plasmodium falciparum*, regulates stress-response to amino-acid starvation. *Malar J* 8:99.
 255. Fried M & Duffy PE (1996) Adherence of *Plasmodium falciparum* to chondroitin sulfate A in the human placenta. *Science* 272(5267):1502-1504.
 256. Smith JD, Craig AG, Kriek N, Hudson-Taylor D, Kyes S, *et al.* (2000) Identification of a *Plasmodium falciparum* intercellular adhesion molecule-1 binding domain: a parasite adhesion trait implicated in cerebral malaria. *Proc Natl Acad Sci USA* 97(4):1766-1771.
 257. Crabb BS, de Koning-Ward TF, & Gilson PR (2010) Protein export in *Plasmodium* parasites: from the endoplasmic reticulum to the vacuolar export machine. *Int J Parasitol* 40(5):509-513.
 258. Edgar RC (2004) MUSCLE: multiple sequence alignment with high accuracy and high throughput. *Nucleic Acids Res* 32(5):1792-1797.
 259. Gouet P, Robert X, & Courcelle E (2003) ESPript/ENDscript: Extracting and rendering sequence and 3D information from atomic structures of proteins. *Nucleic Acids Res* 31(13):3320-3323.

Adelaide Ulricke Hain

DOB July 5th, 1985, Big Rapids, MI
Email: hain.ulli@gmail.com

EDUCATION

- 2008-2013 **Johns Hopkins Bloomberg School of Public Health** Baltimore, MD
PhD, Biochemistry & Molecular Biology
Advisor: Dr. Jürgen Bosch
Thesis: *Characterization, structural analysis, and identification of inhibitors of Atg8 and the Atg8-Atg3 interaction in the malaria parasite, Plasmodium.*
- 2004-2008 **Michigan State University** East Lansing, MI
BS, Human Biology, *summa cum laude*
Lyman Briggs College of Natural Science
Honors College

RESEARCH EXPERIENCE

- 2009-2013 Doctoral student
Biochemical and structural characterization of the plasmodial Atg8-Atg3 interaction, important for autophagy. Determined the X-ray structure of *Plasmodium* Atg8 with Atg3 peptide, which was used to guide development of inhibitors against the interaction. These inhibitors served as molecular probes to study the function of Atg8 in *Plasmodium*.
- 2007-2008 Research Assistant
Microbiology & Molecular Genetics
Advisor: Dr. Cori Fata-Hartley
Contribute to knowledge of viral replication by determination of the mode of action of dipyrimadole in inhibiting synthesis of plus-stranded RNA viruses. A forward genetics approach was used to select for resistant forms of the picornavirus member Mengovirus and the genome was sequenced to identify candidate genes conferring resistance.

PUBLICATIONS

Hain AU, Bartee D, Sanders N, Sullivan D, Levitskaya J, Freel Myers C, Bosch J. Identification of an Atg8-Atg3 protein-protein interaction inhibitor from the MMV Malaria Box active in blood and liver stage *P. falciparum* parasites. *J Med Chem.* 2013 *Submitted.*

Hain AU, Bosch J. Autophagy in *Plasmodium*, a multifunctional pathway? *Comp Struct Biotech J.* 2013 Aug; 8(11). e201308002, doi: 10.5936/csbj.201308002.

Hain AU, Weltzer RR, Hammond H, Jayabalasingham B, Dinglasan RR, Graham DR, Colquhoun DR, Coppens I, Bosch J. Structural characterization and inhibition of the

Plasmodium Atg8-Atg3 interaction. *J Struct Biol.* 2012 Dec;180(3):551-62.
doi:10.1016/j.jsb.2012.09.001.

LAB TECHNIQUES

Molecular cloning, protein purification, X-ray crystallography, Surface plasmon resonance, cell culture, immunofluorescence microscopy

AWARDS & FELLOWSHIPS

2012 JHU Women's Club Rosa Gryder Memorial Award
2011-2013 JH Malaria Research Institute Predoctoral Fellowship
2010 The Elsa Orent Keiles Fellowship in Biochemistry
2006-2008 MSU Lumsden Valrance full-tuition Scholarship
2005 The Sean Healey Memorial Award for Honors Writing

PRESENTATIONS

Apr. 2013 JHSPH World Malaria Day (Poster)
Identification of potential inhibitors against the autophagy protein Atg8 in Plasmodium

Feb. 2013 Keystone Symposia on Autophagy, Inflammation, and Immunity (Poster)
Elucidating and targeting the autophagy system in the malaria parasite

May 2012 Seattle Parasitology Meeting (Oral)
Structural characterization and targeting of Plasmodium Atg8

Apr. 2011 JHSPH World Malaria Day (Poster)
Plasmodium Atg8 and its E2, Encounters of a Targetable Kind

Sept. 2010 Molecular Parasitology Meeting (Poster)
The Plasmodium autophagy system as a potential platform for structure based drug design.

TEACHING EXPERIENCE

Fall 2012 Teaching Assistant - Intro to Molecular Biology (Master's level)
Spring 2011 Teaching Assistant - Genomics (Master's level)

PROFESSIONAL ASSOCIATIONS

American Association for the Advancement of Science